



DIPARTIMENTO DI MATEMATICA E FISICA

CORSO DI LAUREA MAGISTRALE IN FISICA

MASTER DEGREE THESIS

*Characterization of superconducting
resonant RF cavities for axion search
with the QUAX experiment*

October 23, 2018

Author:

Alessio Rettaroli

Supervisor:

Prof. Giuseppe Salamanna

Supervisor:

Dott. Claudio Gatti

Academic year 2017–2018

Abstract

An outstanding result of modern cosmology is that a significant fraction of the Universe is made of Dark Matter. However, the nature of such component is still unknown, apart its gravitational interaction with ordinary baryonic matter. A favored candidate for Dark Matter is the *axion*: a new pseudoscalar particle introduced by Peccei and Quinn to solve the so-called *CP* problem of the strong interactions. The theory, together with experimental bounds, predicts that axions have small couplings to Standard Model particles. In particular the couplings with photons and fermions can be exploited to search for axions.

The QUAX experiment explores the possibility to study the interaction of the dark matter axions comprising the galactic halo with the spin of electrons. In fact, due to the motion of the Solar System through the galactic halo, the Earth is effectively moving through the cold dark matter cloud surrounding the Galaxy and an observer on Earth would see such axions as a wind. In particular, the effect of the axion wind on a magnetized material can be described as an effective oscillating rf field with frequency determined by axion mass. Thus, a possible detector for the axion wind can be a magnetized sample placed inside a microwave cavity, both cooled down at ultra-cryogenic temperatures.

Type-II superconductors are employed as the materials the microwave cavities are made of, with the goal of maintaining high quality factors¹ ($\sim 10^6$) even in the presence of applied magnetic fields, necessary to the axion detection. Niobium, Niobium-Titanium and Magnesium Diboride cavities have been studied.

After briefly reviewing axion physics and their detection techniques, this thesis work is dedicated to the characterization of the aforementioned cavities. This is done by studying how their quality factor changes when an increasing value of a static magnetic field is applied at fixed temperature ($T = 4.2$ K), and the quality factor dependence on temperature with fixed values of magnetic field. Niobium was mostly used to improve the experimental set-up, since its properties are already well known due to its many applications. An unprecedented result was obtained with the Niobium-Titanium cavity, concerning the possibility to improve the sensitivity in the axion search through the axion-photon coupling. This could have resonance in other experiments searching for axions involving microwave cavities. For the Magnesium Diboride cavity a very first test was performed. This is the first bulk cavity made of this material to be studied for these purposes.

The quality factor values of the cavities were obtained performing a fit procedure to the data of the S_{11} (reflection coefficient) and S_{21} (transmission coefficient) cavity parameters, quantities often used in radio-frequency measurements.

¹A quality factor is defined as the electromagnetic energy stored in the cavity divided by the energy dissipated by its conducting walls in one period.

Acknowledgments

To begin I want to thank Giuseppe Salamanna for accepting to be my internal supervisor, and for giving me useful advices on my present and future.

I'm obviously thankful to the COLD lab team: Claudio Gatti (my thesis supervisor at LNF), Daniele Di Gioacchino, Carlo Ligi and Simone Tocci. The beauty of being a small group is that you immediately get in tune with each other, and this is what they did with me. They welcomed me since the first day, they're always available and share their enthusiasm for what they do and for the physics cause.

Thank you also to Danilo Babusci for having read this work and suggested some corrections.

Last but not least, I also would like to thank my friends and classmates Alessio M. Leonardi and Simone Romiti, with which I had interesting discussions on physics and *much more*. I'm grateful to them, as they supported and endured me during this weird period of my life!

Contents

Introduction	1
1 The physics case	4
1.1 Strong CP problem and axions	4
1.1.1 QCD symmetries	4
1.1.2 $U(1)_A$ problem	7
1.1.3 Strong CP problem	12
1.1.4 Axions as a solution to the CP problem	14
1.2 Searching for axions	20
1.2.1 Axion parameter space	22
1.2.2 Astrophysical bounds	24
1.2.3 Axion cosmology	26
1.2.4 Properties of galactic DM axions	28
1.2.5 Detection techniques	30
2 QUAX R&D at LNF	36
2.1 The QUAX experiment	36
2.1.1 Coupling to electrons and detection technique	37
2.1.2 Signal power	39
2.2 Tools to study resonant cavities	43
2.2.1 Radiofrequency concepts	43
2.2.2 Elements of superconductivity	54
2.3 Resonant cavities	61
2.4 Goals of QUAX R&D and this thesis work	64

2.5	Experimental set-up	66
3	Characterization of the resonant cavities	74
3.1	Q determination	74
3.1.1	Q_L measurements through the 3-dB method	75
3.1.2	Q_0 determination through a fit procedure	75
3.2	Measurements	81
3.2.1	Niobium resonant cavity	82
3.2.2	Niobium-Titanium resonant cavities	90
3.2.3	Magnesium Diboride cavity	103
	Conclusion	105
A	Resonant modes of a cylindrical cavity	107
B	3-dB method	114
	Bibliography	116

Introduction

From astrophysical and cosmological observations made from the last century, there is now evidence that only 5% of the Universe constituents is explained by ordinary matter. Another 20% is originated by the Dark Matter (DM) and the rest is accounted by Dark Energy (DE), responsible for the acceleration of the expansion of the Universe itself. Dark Matter is thought to be non-baryonic unrevealed matter, whose existence is proved because it can interact gravitationally with ordinary matter (the effects can be seen at galactic scales and in clusters of galaxies), but DM has not been detected so far with searches of electromagnetic signals, because it does not undergo electromagnetic interactions. Two scenarios can occur, the Hot Dark Matter and the Cold Dark Matter scenarios, Hot and Cold meaning that the DM particles are relativistic or not, respectively. Large scale structure observations suggest that the Cold Dark Matter (CDM) model is more reliable.

The CDM model finds contact points with the Standard Model (SM) of particle physics if one tries to answer the question *what is dark matter made of?* In the context of theories of new physics beyond the Standard Model many new particles arise, and some of these are good candidates to solve the DM problem. Supersymmetry (SUSY) predicts particles that can be included in the category of WIMPs (Weakly Interacting Massive Particles) [1], while in the low energy frontier new light bosons appear when global symmetries are spontaneously broken, like the approximate symmetries of QCD discussed in this work. In the latter case, the particles arising from symmetry breakings are called WISPs, Weakly Interacting Subelectronvolt Particles. Among these there are **axions** and Axion-Like Particles (ALPs). QCD axions are at the moment the best-motivated candidates of DM [1], and since an evidence of supersymmetries is missing in the high energy landscape, increasingly resources are being invested in the search for WISPs, in particular ALPs.

QCD axions are introduced to solve the strong CP problem. The QCD lagrangian

admits an additional term that violates the CP symmetry, but this violation is not seen in strong interactions. The value of the parameter responsible for this violation, $\bar{\theta}$, is constrained to be $\lesssim 10^{-10}$ from experiments [2] while it is expected to be of order 1 from the theory, because it is a sum of two independent parameters coming from two independent physics sectors: QCD and electroweak theory. Peccei and Quinn proposed [3, 4] in 1977 the existence of an additional scalar field, defined in such a way that its potential, with a null minimum, incorporates the $\bar{\theta}$ parameter. In the subsequent months Weinberg and Wilczek interpreted this field as a new spin 0 particle, the axion, that couples very weakly to SM particles and is abundantly produced in the Universe: characteristics that make the axion a good candidate of dark matter. These particles are named after a laundry detergent, since axions have the capability to "clean up" the strong CP problem [5].

Axions can undergo interactions with photons and fermions. Both coupling constants and mass are inversely proportional to a free parameter of the theory, f_a , that represents the energy scale at which the Peccei-Quinn $U(1)$ symmetry is broken, so neither the couplings nor the mass can be *a priori* specified. They have to be determined experimentally. Since in principle they can take any value, the design of an experiment to detect axions is difficult, as it can only test small ranges of axion masses (see "Haloscopes" in the exclusion plot 1.8). Anyway there are some astrophysical and laboratory bounds that restrict the possible values of f_a and m_a (hence of the couplings too), making the detection more feasible.

In 1983 Sikivie [6] proposed two detection techniques, both relying on axion-photons coupling²; the two detectors are called elioscope and haloscope. In both cases an external static magnetic field is applied in a certain volume to stimulate the conversion of the axion into a photon. The elioscope exploits as a source the axion flux coming from the Sun, and photons produced are collected in a sort of telescope structure in which the magnetic field is applied. The haloscope is designed to detect axions from the galactic halo, with the hypothesis that all or part of the DM is made up of axions, and photons are collected in resonant microwave cavities.

In this thesis the **QUAX** experiment is described, whose acronym stands for 'QUest for AXions'. The experiment is funded by INFN, is situated at LNF (Laboratori Nazionali di Frascati) and LNL (Laboratori Nazionali di Legnaro) and is in its R&D phase. QUAX uses resonant cavities as haloscopes and with the application of a static magnetic field can test the axion-photon coupling. QUAX, though, introduces also some novelty in the landscape of haloscopes, as it can also investigate the axion-electron coupling if a magnetized medium is put inside the cavity, in which case the Electron Spin Resonance (ESR) is exploited. Since the power emitted in photons after an interaction is very small, QUAX is studying

²The interaction of axions with photons is not the usual one. An electron can change its energy by absorbing or emitting a photon, while an axion that "hits" a photon disappears, and a new photon is produced.

cavities built with type-II superconducting materials to reach high quality factors in the presence of an applied magnetic field, cooled down to cryogenic temperatures. This also allows to avoid noise due to thermal photons coming from the cavity walls.

During my thesis I contributed to the characterization of some of the resonant cavities available at LNF, joining the team working in the COLD laboratory (CryOgenic Laboratory for Detectors).

The thesis is structured as follows. In the first chapter I present the motivations that led to the introduction of axions, along with a summary of the present detection techniques and experiments dedicated to ALPs research. In the second chapter the QUAX experiment is described. Then the technical tools needed to study resonant cavities are listed, and the laboratory set-up is described. The third chapter is dedicated to the measurements made with different cavities and to their data analysis. In the conclusion there is a short overview of the work done in this thesis and the results obtained are outlined, with some remarks on the future of the QUAX experiment.

CHAPTER 1

The physics case

1.1 Strong CP problem and axions

The formulation of a new scalar field in the Standard Model, the axion field, starts from the observation that in the chiral limit the quarks present some approximate symmetries, among which there is an axial symmetry $U(1)_A$. This brings to predict a wrong mass for the η' meson. This problem is automatically resolved if one takes a glance to the nontrivial QCD vacuum structure, but in doing so a new problem arises: in the QCD Lagrangian a term, with a parameter $\bar{\theta}$ as a coefficient, that violates CP in strong interactions (thus the name *strong* in the title) is introduced. This would cause an Electric Dipole Moment (EDM) for the neutron, that is not observed [2]. As a solution a new axial symmetry in the SM is proposed, the PQ symmetry $U(1)_{PQ}$ (PQ from Peccei and Quinn), which promotes the parameter $\bar{\theta}$ to a dynamical field. A nice introduction and insight to the axion formulation is given in [7].

1.1.1 QCD symmetries

Let us first define what is intended for axial and vector symmetries. For simplicity I will only consider phase transformations.

Taken a quark field $q(x)$ (but this is true for any fermion field $\Psi(x)$) it can be written in the chiral representation¹ as a sum of left- and right-handed fields, $q = (q_L, q_R)^T$ or

¹This refers to the representation of the γ Dirac matrices.

$q = (q_L + q_R)$, obtained from the application of the chiral projection operators P_L ad P_R :

$$q_L = P_L q = \frac{1 - \gamma_5}{2} q \quad q_R = P_R q = \frac{1 + \gamma_5}{2} q. \quad (1.1)$$

I also write the QCD gauge-invariant Lagrangian density that will be useful for further discussions. For one quark flavor it is [8]:

$$\mathcal{L}_{QCD} = \bar{q}_L i\gamma^\mu D_\mu q_L + \bar{q}_R i\gamma^\mu D_\mu q_R - \bar{q}_L m q_R - \bar{q}_R m q_L - \frac{1}{4} G_{\mu\nu}^a G_a^{\mu\nu}, \quad (1.2)$$

with D_μ the covariant derivative, m the mass of the quark and $G_a^{\mu\nu}$ the gluon field strength tensor:

$$G_a^{\mu\nu} = \partial^\mu A_a^\nu - \partial^\nu A_a^\mu + g_s f_{abc} A_b^\mu A_c^\nu, \quad (1.3)$$

where A_a^μ is the gluon vector field, $a, b, c = 1, \dots, 8$ are indexes for the gauge fields, f_{abc} the structure constants of $SU(3)_c$ (the sum over b and c is implicit), and g_s the coupling constant of strong interactions.

A global vector $U(1)_V$ transformation is a phase transformation that rotates the left- and right-handed fields in the same sense:

$$q_L \longrightarrow e^{-i\alpha} q_L \quad q_R \longrightarrow e^{-i\alpha} q_R, \quad (1.4)$$

while a global axial $U(1)_A$ transformation causes the fields to rotate in the opposite sense:

$$q_L \longrightarrow e^{-i\alpha} q_L \quad q_R \longrightarrow e^{i\alpha} q_R. \quad (1.5)$$

For the conjugate fields \bar{q}_L and \bar{q}_R the sign of the exponents has to be changed. Note that these transformations repeat identically for any quark flavor. The field rotations of eq. (1.5) are equivalent to the following rotation of the Dirac field:

$$q \longrightarrow e^{i\alpha\gamma_5} q, \quad (1.6)$$

because in the chiral representation $\gamma_5 = \text{diag}(-1, -1, 1, 1)$, and then $\gamma_5 \Psi_{L,R} = \mp \Psi_{L,R}$.

In the context of the SM, all elementary particle fields are invariant under $SU(3)_c \times SU(2)_W \times U(1)_Y$ transformations, where the c , W and Y subscripts respectively stand for color, weak isospin and hypercharge. The quark fields exhibit additional symmetries concerning also their flavors, if the chiral limit is supposed. Let's consider only u and d quarks; in the chiral limit their masses can be thought to be zero, $m_u, m_d \approx 0$. This is a reasonable assumption, since the actual masses are much smaller than $\Lambda_{QCD} \approx 200$ MeV, being $m_u \simeq 2.2$ MeV and $m_d \simeq 4.7$ MeV [9]. In the chiral limit the symmetries that arise are only approximate, and they would be exact if u and d masses were actually zero. The new global symmetries are $SU(2)_V$, $U(1)_V$, $SU(2)_A$ and $U(1)_A$, or equivalently QCD

acquires a global $SU(2)_V \times SU(2)_A \times U(1)_V \times U(1)_A$ symmetry. To show why they are symmetries it suffices only to look at the mass term in the Lagrangian (1.2):

$$-m\bar{q}q = -m(\bar{q}_L q_R + \bar{q}_R q_L). \quad (1.7)$$

This term is invariant under vector transformations (1.4), so $U(1)_V$ is an exact symmetry in any case (and it implies baryon number conservation [10]), but is clearly not invariant under axial transformations (1.5). But if the quark mass $m \rightarrow 0$, there is no term mixing left- and right-handed fields in \mathcal{L} , and also the axial transformation becomes a symmetry.

An $SU(2)$ transformation is just a little more complicated and involves a doublet of fields, therefore considering as an example a doublet of u and d quarks it writes [11]:

$$\begin{pmatrix} u \\ d \end{pmatrix} \longrightarrow e^{-i\epsilon_k \sigma_k/2} \begin{pmatrix} u \\ d \end{pmatrix}, \quad (1.8)$$

where $k = 1, 2, 3$, ϵ_k are parameters and σ_k the three generators of $SU(2)$ group transformations (Pauli matrices). Note that unlike $U(1)$ phase rotations, the $SU(2)$ transformations mix the quark flavors. In this case it is clear that $SU(2)_V$ transformations maintain mass terms of the form (1.7) invariant, but it is indeed necessary to keep the quark masses to zero to make $SU(2)_V$ a symmetry, because u and d are part of a doublet and therefore they must have the same quantum numbers, including mass. This symmetry is known as the nuclear isospin symmetry, and as a consequence it predicts the existence in the hadron spectrum of couples of baryons with approximately the same mass and the same strong interactions. The simplest example of such a doublet is made up of the well known proton and neutron. It is important to remark that the symmetry is only approximate, due to the different masses of the u and d quarks.

The presence of an $SU(2)_A$ symmetry would predict a doublet of hadrons with same quantum numbers and with quite the same mass as the proton-neutron doublet, but with opposite parity [8], which is not seen to exist. Therefore $SU(2)_A$ has to be somehow broken, and the simplest and elegant way to do it is spontaneous symmetry breaking (SSB). In this case we're not relying on the Higgs mechanism, that introduces an additional scalar field to the Lagrangian, but rather it is assumed that dynamically scalar *quark condensates* form. These are $\bar{q}q$ combinations of fundamental quarks with non-zero vacuum expectation values:

$$\langle 0 | \bar{q}q | 0 \rangle \neq 0. \quad (1.9)$$

Therefore both axial $SU(2)_A$ and $U(1)_A$ symmetries are spontaneously broken. Therefore as a consequence of the Goldstone theorem [11], four massless bosons are expected, three from the broken generators of $SU(2)_A$ and one from $U(1)_A$. In the hadron spectrum there exist a triplet of particles with odd parity: the pion triplet, π^0 and π^\pm . Their masses are

not much smaller with respect to Λ_{QCD} ($m_{\pi^0} \simeq 135$ MeV, $m_{\pi^\pm} \simeq 140$ MeV), but they are the lightest mesons and their masses go to zero as $m_u, m_d \rightarrow 0$. They can be thought of as the Goldstone bosons (in this case called *pseudo*-Goldstone bosons) of the broken $SU(2)_A$ symmetry.

In this simple 2-flavor model the pseudo-Goldstone boson associated with $U(1)_A$ breakdown would be the pseudoscalar η meson, if the s quark didn't exist. It would have a mass smaller than it actually is, if it were only made of $\bar{u}u$ and $\bar{d}d$ quark combinations. The η meson has, on the contrary, a mass of about $m_\eta \simeq 548$ MeV as the combination $\bar{s}s$ also contributes.

In the next section the 3-flavor model will be briefly discussed, at the origin of the $U(1)_A$ issue.

1.1.2 $U(1)_A$ problem

The 3-flavor case for the QCD approximate symmetries is obtained by considering also the s quark, with null mass $m_s \approx 0$. This is an even more rough approximation than before, since the measured s quark mass is $m_s \simeq 95$ MeV. Now QCD possesses a global $SU(3)_V \times SU(3)_A \times U(1)_V \times U(1)_A$ symmetry. The $U(1)_V$ symmetry implies, again, the baryon number conservation, while $SU(3)_V$ symmetry predicts, as an example, triplets with particles degenerate in mass, like the Σ triplet. Then, by breaking the axial symmetries, eight pseudo-Goldstone bosons from $SU(3)_A$ and one from $U(1)_A$ are expected. In the hadron spectrum, in fact, there exist some candidates: the pseudoscalar singlet η' meson and the pseudoscalar octet comprising the three pions, the kaons (K^+, K^-, K^0, \bar{K}^0) and the η meson. The pions are the aforementioned bosons of the $SU(2)_A$ broken symmetry (remember that $SU(2)$ is a subgroup of $SU(3)$ in group theory), and the other mesons have still masses small enough to play the role of pseudo-Goldstone bosons. Now, the η' meson, the would-be ninth pseudo-Goldstone boson, has mass $m_{\eta'} \simeq 958$ MeV, much *higher* compared to Λ_{QCD} . So a ninth boson associated to the $U(1)_A$ breaking seems not to exist. Nevertheless, Weinberg [12] pointed out that in this 3-flavor model the pseudo-Goldstone boson associated to the $U(1)_A$ broken symmetry should have a mass:

$$m_{\eta'} < \sqrt{3}m_\pi \approx 240 \text{ MeV}, \quad (1.10)$$

a value that is quite far from the observed one. The so called $U(1)_A$ problem resides in this discrepancy: why the observed η' meson is *so* heavy?

Solution to the $U(1)_A$ problem

From the discussions that follow, the solution at this problem can be summarized with a very simple statement: the expected pseudo-Goldstone boson doesn't exist because there

is no $U(1)_A$ symmetry at all! Though, this simplicity hides quite difficult and intriguing physics arguments, as *chiral anomalies* and the nontrivial *topology* of the QCD vacuum. Moreover, the solution to this issue causes the strong *CP* problem to arise. In what comes I will only refer to the highlights, following the guidelines of Refs. [8, 13, 7].

As a starting point one can recall the Noether's theorem, stating that each symmetry of a Lagrangian (density) has associated to it a conserved current (density) J^μ , in formulas:

$$\partial_\mu J^\mu = 0.$$

As a consequence there is a conserved quantity, i.e. a time-independent quantity, that is the spatial integral of the time component J^0 of the current:

$$Q = \int d^3x J^0 = \text{const.}$$

A conserved current is obtained as a combination of the fields involved in the transformation and their derivatives. The axial current associated with a $U(1)_A$ transformation (see (1.6), now with Ψ instead of q) is:

$$J_5^\mu = \bar{\Psi} \gamma^\mu \gamma_5 \Psi. \quad (1.11)$$

The name *axial* also means that a quantity is odd with respect to a parity operation, and this is clear from the above equation.

At this point the chiral anomaly plays an important role. A symmetry of a Lagrangian in the classical field theory is said to be anomalous when it is violated in its quantum formulation. It is worth noting that anomalies are not renormalizable, so if they appear in gauge theories (and indeed they do) it is important that they cancel with each other. I won't talk about renormalizability here, as I would run out of the scope of this thesis, but let me say that anomalies do have observable effects: a striking example is the dominant contribution of anomalies to the $\pi^0 \rightarrow \gamma\gamma$ decay through the triangle diagram (Fig. 1.1).

Returning to the axial current of eq. (1.11), it can be seen that for a theory with a fermion interacting with gauge bosons of the type:

$$\mathcal{L} = \bar{\Psi} (i \gamma^\mu \partial_\mu - m) \Psi + \text{interactions} + \text{gauge fields}, \quad (1.12)$$

a $U(1)_A$ transformation of the fermion fields has an associated axial current J_5^μ that satisfies:

$$\partial_\mu J_5^\mu = 2im \bar{\Psi} \gamma_5 \Psi. \quad (1.13)$$

Then $U(1)_A$ is an approximate symmetry only if we put $m = 0$, that is true in the chiral limit, as seen in Sec. 1.1.1 for the u and d quarks. To see the effects of the chiral anomaly

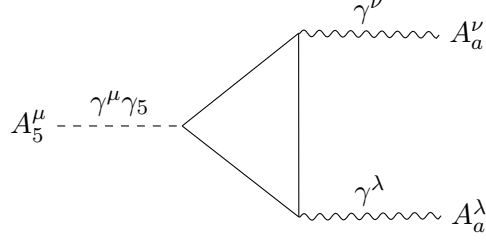


Figure 1.1: The anomalous one-loop diagram of an axial current that couples to two gauge bosons.

on J_5^μ , the presence of the axial symmetry can be simulated by adding to the Lagrangian a vector axial boson A_5^μ having interactions with the fermion, the interaction being $-g' J_5^\mu A_{5\mu}$ in analogy with the electromagnetic interaction. At the quantum level of the field theory, this Lagrangian leads to a transition from the axial boson to two gauge bosons through a one-loop diagram, Figure 1.1. Performing the regularization of the amplitude of the diagram, this causes the Ward identity to be no longer satisfied (see chapter 5 of [14]). The analogous of the Ward identity in the position space is the expression of the four-divergence of the current, $\partial_\mu J_5^\mu$, that acquires an additional term. Referring to strong interactions, i.e. considering quarks as fermions and gluons as gauge bosons, in the limit $m \rightarrow 0$ this term is [8, 10]:

$$\partial_\mu J_5^\mu = -N_f \frac{g_s^2}{32\pi^2} \varepsilon^{\mu\nu\rho\sigma} \text{Tr}(G_{\mu\nu} G_{\rho\sigma}) \equiv -N_f \frac{g_s^2}{16\pi^2} \text{Tr}(G_{\mu\nu} \tilde{G}^{\mu\nu}). \quad (1.14)$$

N_f is the number of quark flavors that one includes in the theory, $\varepsilon_{\mu\nu\rho\sigma}$ the Levi-Civita antisymmetric tensor² and $G_{\mu\nu}$ is defined as:

$$G^{\mu\nu} = \lambda_a G_a^{\mu\nu}, \quad (1.15)$$

where λ_a are the generators of $SU(3)_c$ group, $a = 1, \dots, 8$ is again an index for the gauge fields, and the gluon field strength tensor $G_a^{\mu\nu}$ has been defined in eq. (1.3). In eq. (1.14) the trace is defined as:

$$\text{Tr}(G^{\mu\nu} \tilde{G}^{\mu\nu}) = \text{Tr}(\lambda_a G_a^{\mu\nu} \lambda_b \tilde{G}_{\mu\nu}^b) = \frac{1}{2} G_a^{\mu\nu} \tilde{G}_{\mu\nu}^a, \quad (1.16)$$

and \tilde{G} is defined as the dual tensor of G :

$$\tilde{G}^{\mu\nu} = \frac{1}{2} \varepsilon^{\mu\nu\rho\sigma} G_{\rho\sigma}.$$

From eq. (1.14), since $\partial_\mu J_5^\mu \neq 0$, it is evident that the axial current is actually not conserved, because of the effect of the chiral anomaly. Therefore $U(1)_A$ symmetry is

²Here it is assumed the convention $\varepsilon^{0123} = +1$.

automatically broken (it is not even an approximate symmetry at all). This implies that a pseudo-Goldstone boson associated to $U(1)_A$ is no longer needed in the hadron spectrum and the arguments of Weinberg on the η' mass become irrelevant. It seems that the $U(1)_A$ problem is resolved by only invoking the chiral anomaly, but this is not the whole story. In fact, inserting eqs. (1.15) and (1.3) in eq. (1.14), the right hand side of the latter turns out to be a total derivative:

$$\begin{aligned}\partial_\mu J_5^\mu &= -N_f \frac{g_s^2}{32\pi^2} \partial_\mu K^\mu \\ K^\mu &= \epsilon^{\mu\nu\rho\sigma} A_\nu^a \left[G_{\rho\sigma}^a - \frac{g_s}{3} f^{abc} A_\rho^b A_\sigma^c \right].\end{aligned}\tag{1.17}$$

Thus a new \hat{J}_5^μ current can be defined:

$$\partial_\mu \hat{J}_5^\mu \equiv \partial_\mu \left(J_5^\mu + N_f \frac{g_s^2}{32\pi^2} K^\mu \right) = 0,\tag{1.18}$$

and \hat{J}_5^μ is a conserved quantity. As a consequence of the Noether's theorem there should be a global symmetry, so the $U(1)_A$ problem strikes back.

From eq. (1.14) it is also seen that an extra term adds to the Lagrangian [15]:

$$\delta\mathcal{L} = \alpha \partial_\mu J_5^\mu = -\alpha N_f \frac{g_s^2}{16\pi^2} \text{Tr} \left(G_{\mu\nu} \tilde{G}^{\mu\nu} \right),\tag{1.19}$$

where α is the parameter of the $U(1)_A$ transformation (eq. (1.6)). Now, in quantum field theory the Lagrangian action $S = \int \mathcal{L} d^4x$ is left unchanged, and hence there are no physical consequences, if the Lagrangian variation $\delta\mathcal{L}$ is either zero or equal to a four-divergence. This seems to be the case, being $\delta\mathcal{L} \sim \partial_\mu K^\mu$, so in a first instance one can think of discarding the α -term in the Lagrangian because it has no observable effects. However this can be done only if the surface integral of K^μ can be neglected, and this is true with the usual hypothesis that the fields are null at spatial infinity. And here comes the turning point: the gauge fields A_a^μ of QCD appearing in K^μ do not all tend to zero simultaneously at infinity, therefore the surface integral of K^μ does not cancel and this has physical relevance. To understand how the $U(1)_A$ problem is resolved and what physical consequence is involved, I treat just the tip of the iceberg of the QCD vacuum structure. More details can be found in Refs. [10, 8] and therein references.

Under the action of a gauge unitary transformation \mathcal{U} , the gauge fields A_a^μ transform as follows (in a gauge where the time-like components are zero, $A_a^0 = 0$):

$$A^i \longrightarrow \mathcal{U} A^i \mathcal{U}^{-1} + \frac{i}{g_s} \mathcal{U} \nabla^i \mathcal{U}^{-1},\tag{1.20}$$

where $A^i \equiv \frac{\lambda_a}{2} A_a^i$. A vacuum configuration is defined by $A^i = 0$, but there are other

infinite equivalent vacuum configurations corresponding to the gauge transformations of A^i , that are $(A^i)' = \frac{i}{g_s} \mathcal{U} \nabla^i \mathcal{U}^{-1}$. It turns out that it is not possible to smoothly transform each vacuum configuration into another (i.e. to reach each vacuum with infinitesimal transformations starting from the identity). This implies that the vacua are separated by energy barriers. Each vacuum is then classified by an integer number n , called *winding number*, associated to a specific operator \mathcal{U}_n . The vacua are then indicated by $|n\rangle$. For each n a different expression of the fields A^i exists. For instance, the solution with $n = 1$ is called **instanton**, while $n = 0$ corresponds to $A^i = 0$ and $\mathcal{U}_0 = 1$.

Restoring all the components of A^μ , the winding number has the expression [10]:

$$n = \frac{1}{24\pi^2} \int dS_\mu \varepsilon^{\mu\nu\rho\sigma} \text{Tr} [(\mathcal{U} \partial_\nu \mathcal{U}^{-1})(\mathcal{U} \partial_\rho \mathcal{U}^{-1})(\mathcal{U} \partial_\sigma \mathcal{U}^{-1})], \quad (1.21)$$

with dS_μ the surface element in 4-D euclidean space. 't Hooft realized that this is exactly the space-time integral of the first line of eq. (1.17):

$$n = \frac{g_s^2}{32\pi^2} \int d^4x \text{Tr} (G_{\mu\nu} \tilde{G}^{\mu\nu}). \quad (1.22)$$

What's interesting is the possibility of quantum tunnelling between different vacua with different winding numbers. The amplitude of the transition from $|n_1\rangle$ to $|n_2\rangle$ is not negligible, so it is preferable to define a true vacuum that possibly remains fixed. The operator \mathcal{U}_k also acts as a "tunnelling" operator:

$$\mathcal{U}_k |n\rangle = |n+k\rangle,$$

and we want the true vacuum to be invariant under this operation. A superposition of all the vacua satisfies this request and is the so called **θ -vacuum**, defined as:

$$|\theta\rangle = \sum_n e^{-in\theta} |n\rangle. \quad (1.23)$$

If now the transition probability from a θ vacuum to a θ' vacuum is evaluated, it is found to be [10]:

$$\mathcal{M}_{\theta \rightarrow \theta'} \sim \delta(\theta' - \theta) e^{-(S - in\theta)}. \quad (1.24)$$

The Dirac function confirms that there is no transition between different values of this vacuum, as requested from its definition, but in the exponent the action S is summed to a term including the winding number. Therefore the amplitude can also be calculated from an effective action:

$$S_{\text{eff}} = S - in\theta = S + \frac{g_s^2}{32\pi^2} \theta_{QCD} \int d^4x \text{Tr} (G_{\mu\nu} \tilde{G}^{\mu\nu}).$$

The last equality follows from eq. (1.22), the Wick rotation has been used to pass from a euclidean to a Minkowski space and θ has been renamed to θ_{QCD} . Finally we can say that the Lagrangian acquires, for the same reason, an additional term \mathcal{L}_θ given by:

$$\mathcal{L}_\theta = \frac{g_s^2}{32\pi^2} \theta_{QCD} \text{Tr} \left(G_{\mu\nu} \tilde{G}^{\mu\nu} \right). \quad (1.25)$$

This Lagrangian is still Lorentz- and gauge-invariant, but due to the presence of $\varepsilon_{\mu\nu\rho\sigma}$ it violates parity and time reversal. Hence, because of the CPT theorem, it also violates CP symmetry. We will see in the next section that CP is not indeed violated in the strong sector, and this leads to the strong CP problem.

To conclude this section I remark that the $U(1)_A$ problem is untied. In fact the axial current J_5^μ is not conserved, since the surface term $\int d\sigma_\mu K^\mu$ is non-vanishing (eq. (1.17)), because of the complicated structure of the QCD vacuum. The current \hat{J}_5^μ is conserved (see eq. (1.18)), but it cannot be associated to a symmetry in the theory because it is not gauge-invariant. In fact, the charge $\hat{Q}_5 = \int d^3x \hat{J}_5^0$, under a gauge transformation \mathcal{U}_1 , transforms as [13]:

$$\mathcal{U}_1 \hat{Q}_5 \mathcal{U}_1^{-1} = \hat{Q}_5 + N_f, \quad (1.26)$$

for $n \neq 0$. Then $U(1)_A$ is not a symmetry of QCD, neither exact nor approximate, since no gauge-invariant conserved current is associated with it.

1.1.3 Strong CP problem

So far quarks and gluons in the QCD sector only have been considered. But quarks also undergo, of course, electroweak interactions. Here we will see that another source of CP violation coming from the electroweak sector is present.

To understand how a θ -term can arise from electroweak interactions, it is worth noting what is the variation of θ_{QCD} under an axial transformation. For N_f flavors of massless quarks the $U(1)_A$ is anomalous, and the Lagrangian acquires a further term as in eq. (1.19), that adds to the θ -term of the Lagrangian (1.25), causing θ_{QCD} to shift:

$$\theta_{QCD} \longrightarrow \theta_{QCD} - 2N_f\alpha. \quad (1.27)$$

This means that if quark masses are zero and if only θ_{QCD} contributed to CP violation, by a suitable choice of the parameter α , we could make $\theta_{QCD} = 0$.

After the electroweak spontaneous symmetry breaking through the Higgs mechanism, the mass term for the quarks is:

$$\mathcal{L}_{mass} = -\bar{u}_{iL} M_{ij}^u u_{jR} - \bar{d}_{iL} M_{ij}^d d_{jR} + h.c.,$$

where u (d) denotes the vector of the up-quark (down-quark) generation in the basis in

which it is an eigenstate of the electroweak interactions, and M^u , M^d the mass matrices in this basis. The latter are not diagonal or hermitian, but can be diagonalized through unitary matrices U and W such that:

$$U_u^\dagger M^u W_u = m_u, \quad U_d^\dagger M^d W_d = m_d,$$

with $m_{u,d}$ diagonal and real matrices. This can be achieved transforming the quark vectors with an internal transformation:

$$(\bar{u}_L)_i \longrightarrow (\bar{u}_L)_j \left(U_u^\dagger \right)_{ji} \quad (u_R)_i \longrightarrow (W_u)_{ij} (u_R)_j,$$

and the same for the d -quark generation. In this regard, we can say that a particular transformation that diagonalize M^u and M^d exists and the matrices U and W can be absorbed by the quark fields. The transformations are a combination of vector $U(1)_V$ and axial $U(1)_A$ rotations, with parameter α that can be chosen as [13]:

$$\theta_{EW} \equiv \alpha = \frac{1}{2N_f} \arg \left[\det \left(M^u M^d \right) \right].$$

But $U(1)_A$ is anomalous and hence the Lagrangian must present another term as (1.25). As a result the parameter θ_{QCD} is changed by θ_{EW} when a $U(1)_A$ transformation is applied to diagonalize the quark mass matrices (see eq. (1.27)):

$$\bar{\theta} \equiv \theta_{QCD} - \theta_{EW} = \theta_{QCD} - \arg \left[\det \left(M^u M^d \right) \right]. \quad (1.28)$$

Finally, the Lagrangian that has physical observable effects is the one including the $\bar{\theta}$ -term:

$$\mathcal{L}_{CP\,viol.} = \mathcal{L}_{QCD} + \frac{g_s^2}{32\pi^2} \bar{\theta} \text{Tr} \left(G_{\mu\nu} \tilde{G}^{\mu\nu} \right). \quad (1.29)$$

This is, though, an additional contribution to the CP violation in the SM, since it is known that from the electroweak sector another violating source is present: the phase δ_{CKM} of the CKM matrix, responsible for the kaon and B oscillations. This is *not* equivalent to θ_{EW} , and we may not confuse between them. In fact the CKM matrix is necessary to rotate the fields from the mass basis to the basis in which the quarks undergo weak interactions with the right observed coupling constants.

Neutron EDM

The strong CP problem itself comes when one accounts for the predictions that a CP -violating term produces, one of which is the existence of an Electric Dipole Moment (EDM) for hadrons. Among all the hadrons, the most striking example is the neutron. Due to the

additional term in the Lagrangian the neutron should possess an EDM proportional to $\bar{\theta}$:³

$$d_n \simeq e \cdot \bar{\theta} \frac{m_u m_d}{f_\pi^2(m_u + m_d)} \left(\frac{0.9}{4\pi^2} \ln \frac{\Lambda}{m_\pi} \right) \simeq 2.4 \cdot 10^{-16} \bar{\theta} e \text{ cm}, \quad (1.30)$$

where e is the electric charge of the electron, $f_\pi = 93$ MeV the pion decay constant, m_u , m_d the up quark and down quark masses respectively, and Λ a constant of order the neutron mass m_n . Natural units $\hbar = c = 1$ are used, so $1 \text{ eV} \approx 1 \mu\text{m}^{-1}$. But the neutron EDM has been measured with high accuracy and up to now it seems to be zero. From the most recent experiment on neutron EDM [2] we can assert that the upper limit is:

$$d_n \lesssim 1.6 \cdot 10^{-26} e \text{ cm}, \quad (1.31)$$

then giving an estimation of the upper limit that can be put on $\bar{\theta}$:

$$|\bar{\theta}| \lesssim 0.67 \cdot 10^{-10}. \quad (1.32)$$

This is an embarrassingly small value, considering that the contributions to $\bar{\theta}$ come from two independent sectors (strong and electroweak), and then it is expected that at least one contribution is of $\mathcal{O}(1)$. The strong CP problem can then be stated as: *why $\bar{\theta}$ is so small?*. That is, apparently there are no reasons for θ_{QCD} and θ_{EW} to tune exactly to zero when they are summed.

1.1.4 Axions as a solution to the CP problem

The most referenced solutions to this problem are essentially three:

- the presence of a massless quark;
- a spontaneous CP violation;
- the Peccei-Quinn mechanism.

The first relies on the possibility that a quark, for example the u quark, is massless, in which case the $\bar{\theta}$ parameter would be irrelevant, because as in eq. (1.30) the electric dipole would vanish. More generally, in this case the θ_{EW} term wouldn't be present, and the axial symmetry would be broken only by the chiral anomaly, so θ_{QCD} could be gauged away by a phase rotation. Though this possibility is clearly ruled out by experiment, since there is no evidence of massless quarks. The second solution postulates the existence in the Standard Model of a more general CP symmetry, that would be spontaneously broken, allowing for CP violation. However this is not the favored solution, because experimental data is in excellent agreement with a CP violation due to the CKM matrix of the Standard

³I report the value given in [16], but one of the first calculations were made by Baluni [17].

Model [15]. This is an explicit symmetry breaking. In the third solution, discussed below, an additional $U(1)_A$ symmetry is assumed in the theory and this leads to the presence of an additional pseudo-Goldstone boson: the *axion*. From now on I will only refer to the Peccei-Quinn solution to the strong CP problem.

Peccei-Quinn mechanism

The solution was proposed by R. Peccei and H. Quinn in two papers in 1977 [3, 4]. They suggested to introduce a further exact axial global $U(1)$ symmetry, now called $U(1)_{PQ}$ symmetry, at the classical Lagrangian by adding a scalar field. The key argument is that if it is spontaneously broken and has a chiral anomaly, there is an additional $G_{\mu\nu}\tilde{G}^{\mu\nu}$ term in the Lagrangian that can absorb the $\bar{\theta}$ term. Then in 1978 Weinberg [18] and Wilczek [19] realized that adding a scalar field, that causes the spontaneous breaking of the $U(1)_{PQ}$ symmetry, generates a new Goldstone boson: the axion.

To show the mechanism it suffices to consider only one quark flavor⁴ and a new scalar complex field σ ; then the model can be extended to include other flavors. Since a mass term for the quark is not invariant under $U(1)$ rotations (see eq. (1.7)), we must begin from a Lagrangian with a massless quark and Yukawa couplings with the scalar field:

$$\mathcal{L}_{\text{Yuk}} = -y(\bar{q}_L \sigma q_R + \bar{q}_R \sigma^* q_L), \quad (1.33)$$

the σ field having a Lagrangian:

$$\mathcal{L}_\sigma = \frac{1}{2}\partial_\mu\sigma\partial^\mu\sigma^* - V(|\sigma|) = \frac{1}{2}\partial_\mu\sigma\partial^\mu\sigma^* - \mu^2|\sigma|^2 - \frac{\lambda}{4}|\sigma|^4, \quad (1.34)$$

and suppose that the potential has a minimum at $|\sigma| = f_a$. Applying an axial $U(1)$ transformation to the quarks they rotate as in (1.5), $q_L \rightarrow e^{-i\alpha}q_L$ and $q_R \rightarrow e^{i\alpha}q_R$. Then, for the Lagrangian to be invariant under this rotations, it is required that σ changes as $\sigma \rightarrow e^{-2i\alpha}\sigma$. If the scalar field satisfies that condition, $U(1)_{PQ}$ is an exact global symmetry of the Lagrangian. This symmetry has now to be spontaneously broken in order to generate the quark mass. Writing σ as an expansion around the minimum:

$$\sigma(x) = (\rho(x) + f_a) e^{ia(x)/f_a}, \quad (1.35)$$

with $\rho(x)$ and $a(x)$ two real fields, the Lagrangian acquires a quark mass term proportional to f_a , kinetic terms for the fields ρ and a , self-interactions and interactions between ρ , a and the quark. The ρ field plays the role of the Higgs boson in the EWSSB, while the axion $a(x)$ is supposed to be the massless Goldstone boson associated to the breakdown

⁴The quark is always charged under $SU(3)_c$, and so it has interactions with vector gauge fields representing the gluons.

of a global $U(1)$ symmetry, as noted by Weinberg and Wilczek. But after the symmetry breaking $U(1)_{PQ}$ presents, as usual, a chiral anomaly and this causes the Lagrangian to acquire another CP -violating term proportional to the parameter α of the transformation (similar to eq. (1.29)). We note now from equation (1.35) that when σ is rotated by an angle α , the field a undergoes the transformation:

$$a \longrightarrow a + \alpha f_a. \quad (1.36)$$

Then the parameter α in the violating term can be substituted with $\frac{a}{f_a}$, and the final Lagrangian takes the form [13]:

$$\mathcal{L}_{\text{eff}} = \mathcal{L}_q + \mathcal{L}_\rho + \frac{1}{2} \partial_\mu a \partial^\mu a + \mathcal{L}_{\text{int}} [\partial^\mu (a/f_a); q] + \frac{\alpha_s}{8\pi} \bar{\theta} G_{\mu\nu}^b \tilde{G}_b^{\mu\nu} + \frac{\alpha_s}{8\pi} \frac{a}{f_a} G_{\mu\nu}^b \tilde{G}_b^{\mu\nu}. \quad (1.37)$$

Here \mathcal{L}_{int} contains the derivative interactions of the axion with the matter field q (the quark), $\alpha_s \equiv \frac{g_s^2}{4\pi}$ and the expression $\frac{1}{2} G_{\mu\nu}^b \tilde{G}_b^{\mu\nu}$ has been used in place of $\text{Tr}(G_{\mu\nu} \tilde{G}^{\mu\nu})$. The last contribution to this Lagrangian must be seen as a potential V_{eff} for the axion, because it is neither a kinetic term nor a usual mass term. This has two consequences: it solves the strong CP problem and it gives a mass to the axion, that now has to be referred to as a *pseudo-Goldstone* boson.

It solves the strong CP problem, because it can absorb the $\bar{\theta}$ term in a redefinition of the potential or equivalently of the axion field. In fact, including the $\bar{\theta}$ term in the potential and imposing that it has a minimum when calculated in the vacuum, $\left\langle \frac{\partial V_{\text{eff}}}{\partial a} \right\rangle = 0$, it can be shown [4] that this condition implies:

$$\langle a \rangle = -\bar{\theta} f_a, \quad (1.38)$$

and it can be said that the axion field a is the dynamical version of the $\bar{\theta}$ angle. The Lagrangian (1.37) can be rewritten in terms of a physical axion field with null vacuum expectation value, defined as:

$$a_{\text{phys}} = a - \langle a \rangle. \quad (1.39)$$

The second effect of the potential is giving the axion a mass. In fact this term in the Lagrangian is an *explicit* breaking of $U(1)_{PQ}$ symmetry, and this can be imagined as a tilt of the wine-bottle-shaped potential $V(|\sigma|)$ along a certain direction. As a consequence, after the symmetry breaking the axion rolls towards the new tilted minimum and oscillates around that, acquiring a mass. This can be calculated from the potential as:

$$m_a^2 = \left\langle \frac{\partial^2 V_{\text{eff}}}{\partial a^2} \right\rangle_{\langle a \rangle = -\bar{\theta} f_a}. \quad (1.40)$$

The effective Lagrangian can now be rewritten after the above considerations; adding

the mass term, this is:

$$\begin{aligned}\mathcal{L}_{\text{eff}} = \mathcal{L}_q + \mathcal{L}_\rho + \frac{1}{2} \partial_\mu a_{\text{phys}} \partial^\mu a_{\text{phys}} - \frac{1}{2} m_a^2 a_{\text{phys}}^2 + \\ + \mathcal{L}_{\text{int}} [\partial^\mu (a_{\text{phys}}/f_a); q] + \frac{\alpha_s}{8\pi} \frac{a_{\text{phys}}}{f_a} G_{\mu\nu}^b \tilde{G}_b^{\mu\nu},\end{aligned}\quad (1.41)$$

where now the term $\mathcal{L}_{agg} \sim a_{\text{phys}} G_{\mu\nu}^b \tilde{G}_b^{\mu\nu}$ represents an interaction between the axion and the gluons. The strong CP problem can be considered solved, because when axion excitations are not present, a_{phys} is zero and the classical potential is minimized at zero. When excitations are present, $a_{\text{phys}} \neq 0$ and a CP violation is still present. However when observable quantities depending on a_{phys} , as the neutron EDM, are considered over a long time interval, they average to zero and the CP violation is not seen. The CASPER experiment, indeed, tries to detect just the time-varying nEDM resulting from the axion-neutron interaction [20].

Now that the simple model has been developed it must be extended to the whole SM; different models arise, depending on how the $U(1)_{PQ}$ symmetry is added to the SM Lagrangian. Below I will only cite the PQWW, the KSVZ and the DFSZ models. In the following I will refer to a_{phys} simply as a , redefining $a \equiv a_{\text{phys}}$.

PQWW model

In the framework of the minimal SM all the fermions acquire a mass thanks to the coupling with the Higgs doublet Φ . When all quark flavors are included in the PQ mechanism the σ field cannot simply be identified with the Higgs doublet. In fact, in the Higgs model the down-type quarks couple to Φ in the Yukawa Lagrangian, while up-type quarks couple to $\tilde{\Phi} = i\sigma_2 \Phi^*$, that does not transform in the same way as Φ does under $U(1)_{PQ}$ transformations, condition necessary to make the Lagrangian $U(1)_{PQ}$ invariant. Peccei and Quinn thus thought of a non-minimal model in which there are two Higgs doublets, Φ_1 and Φ_2 , having transformations that preserve $U(1)_{PQ}$ invariance. The Yukawa couplings can be written as:

$$\mathcal{L}_{\text{Yuk}} = \Gamma_{ij}^u \bar{Q}_{Li} \Phi_1 u_{Rj} + \Gamma_{ij}^d \bar{Q}_{Li} \Phi_2 d_{Rj} + \Gamma_{ij}^l \bar{L}_{Li} \Phi_2 l_{Rj} + h.c., \quad (1.42)$$

where here L_L and l_R represent a lepton doublet and a lepton singlet. Calling v_1 and v_2 the minima of the potentials for Φ_1 and Φ_2 respectively, and $f_a = \sqrt{v_1^2 + v_2^2}$, the vacuum values of the doublets are [13]:

$$\Phi_1 = \frac{v_1}{\sqrt{2}} \begin{pmatrix} 1 \\ 0 \end{pmatrix} e^{ixa/f_a}, \quad \Phi_2 = \frac{v_2}{\sqrt{2}} \begin{pmatrix} 0 \\ 1 \end{pmatrix} e^{ia/x f_a},$$

with $x = v_2/v_1$. The Lagrangian now possesses the requested $U(1)_{PQ}$ symmetry, if Φ_1 , Φ_2 and the right-handed fields undergo the transformations:

$$\begin{aligned}\Phi_1 &\longrightarrow e^{i\alpha x} \Phi_1 & u_R &\longrightarrow e^{-i\alpha x} u_R \\ \Phi_2 &\longrightarrow e^{i\alpha/x} \Phi_2 & d_R &\longrightarrow e^{-i\alpha/x} d_R.\end{aligned}$$

The left-handed fields are taken fixed, and for the leptons the same transformations hold.

The axion mass has been calculated with effective Lagrangian techniques [13]. In this calculations mixing terms with neutral pions and η mesons arise, and these are responsible for generating the mass term of the axion. These mixings also allow the axion to have interactions with two photons, that can be exploited to design an experimental approach to the axion detection, as discussed in Sec. 1.2. Note that f_a is a free parameter of the theory, and in the PQWW model it is assumed to be equal to v , the energy scale of electroweak interactions: $f_a = \sqrt{v_1^2 + v_2^2} \equiv v \simeq 246 \text{ GeV}$. With this value, the mass and the couplings are:

$$m_a = \frac{m_{\pi^0} f_\pi}{v} \frac{\sqrt{m_u m_d}}{(m_u + m_d)} \simeq 24 \text{ keV}, \quad (1.43)$$

$$\mathcal{L}_{a\gamma\gamma} = K_{a\gamma\gamma} \frac{\alpha_{\text{em}}}{4\pi} \frac{a}{f_a} F_{\mu\nu} \tilde{F}^{\mu\nu}, \quad (1.44)$$

with $K_{a\gamma\gamma} = N_g (x + 1/x) \frac{m_u}{m_u + m_d}$ and N_g the number of fermion generations, $\alpha_{\text{em}} = \frac{e^2}{4\pi}$ the fine structure constant of QED in natural units, $F_{\mu\nu}$ the electromagnetic field strength tensor. Evidently both the mass and all the couplings are model-dependent, including the axion-gluon-gluon coupling of eq. (1.41) that takes an extra factor $\xi = N_g (x + 1/x)$ in this model:

$$\mathcal{L}_{agg} = \xi \frac{\alpha_s}{8\pi} \frac{a}{f_a} G_{\mu\nu} \tilde{G}^{\mu\nu}. \quad (1.45)$$

The PQWW model, however, has been ruled out by experiment. In fact the predicted branching ratio of the decay $K^+ \rightarrow (\pi^+ + a)$ has been excluded by the measured branching ratio of the process $K^+ \rightarrow (\pi^+ + \text{nothing})$ [21]. Evidences of this type brought to think that it is more likely that theories in which $f_a \gg v$ are more reliable, and since the axion mass and the coupling constants are inversely proportional to f_a this leads to theories with light axions very weakly coupled to SM particles. These are called *invisible* axion models.

Invisible axion models

The two major models of invisible axions are the KSVZ model, from Kim [22] and Shifman, Vainshtein, Zakharov [23] and the DFSZ model, due to Zhitnitsky [24] and Dine, Fischler, Srednicki [25]. In the KSVZ model only a complex scalar field σ and a single heavy quark are added to the SM, with the energy breaking scale $f_a \gg v$. The quark is extremely massive because it acquires a mass $M_Q \propto f_a$. The axion appears in the phase of the σ

field, and its mass has the same form as in the PQWW model, but rescaled with the new f_a value:

$$m_a = \left(\frac{v}{f_a} \right) m_a^{PQWW}. \quad (1.46)$$

Both the new quark and the scalar field are $SU(2)_W \times U(1)_Y$ scalars, and all the SM particles are $U(1)_{PQ}$ scalars, so the axion has not interactions with leptons.

The DFSZ model is an extension of the PQWW one. Here, besides the Higgs doublets Φ_1 and Φ_2 , also a complex scalar field σ is added. As in the PQWW model, all quarks and leptons possess PQ charges, and σ is an $SU(2)_W \times U(1)_Y$ scalar. The axion mass has the same expression as in eq. (1.46), remembering that now⁵ $f_a = \langle \sigma \rangle$. In both models, though, the couplings are different from the PQWW case, because $K_{a\gamma\gamma}$ and ξ are model-dependent.

There are many other details concerning the axion derivation and its dynamics, and here I've only given an idea of the physics beyond it. The goal was to justify the search for axions with theoretically motivated arguments, and to introduce some useful concepts as a starting point for the experimental search. Also, there are many other exotic models that predict axions with different masses and couplings, that I haven't treated and that are summarized, for example, in Refs. [1, 26].

⁵Actually in the DFSZ model f_a is rescaled to $\tilde{f}_a = f_a/2N_g$.

1.2 Searching for axions

In the first section we saw that one way to solve the strong CP problem is introducing a new particle (and possibly other Higgs fields) in the SM, the axion, which is a natural extension of the theory. From the properties that a Goldstone boson of an axial $U(1)$ symmetry must possess, we saw that the axion is a massive pseudoscalar boson electrically neutral. After motivating theoretically the introduction of the axion, in this section I will introduce some basics of the experimental search. I will focus on the detection techniques and will describe which bounds can be put on axion mass and couplings from astrophysical and cosmological observations.

One needs to first illustrate the axion-photon-photon coupling and the Primakoff effect, because the latter is the main process that allows axion production in stars and its detection. For convenience I report here the expression (1.44) of the axion coupling to two photons:

$$\mathcal{L}_{a\gamma\gamma} = K_{a\gamma\gamma} \frac{\alpha_{\text{em}}}{4\pi} \frac{a}{f_a} F_{\mu\nu} \tilde{F}^{\mu\nu},$$

and remember that $K_{a\gamma\gamma}$ is a dimensionless model-dependent parameter. The interaction can be rewritten more compactly defining the coupling constant $g_{a\gamma\gamma}$:

$$\mathcal{L}_{a\gamma\gamma} = \frac{1}{4} g_{a\gamma\gamma} a F_{\mu\nu} \tilde{F}^{\mu\nu}, \quad (1.47)$$

$$g_{a\gamma\gamma} = \frac{\alpha_{\text{em}}}{\pi} \frac{K_{a\gamma\gamma}}{f_a}. \quad (1.48)$$

Now $g_{a\gamma\gamma}$ has dimensions GeV^{-1} but is still model-dependent. It is important to note that $g_{a\gamma\gamma}$ is inversely proportional to the scale constant f_a . Furthermore, the electromagnetic interaction can also be written in terms of the electric and magnetic fields, the components of the $F_{\mu\nu}$ tensor:

$$\mathcal{L}_{a\gamma\gamma} = \frac{1}{4} g_{a\gamma\gamma} a F_{\mu\nu} \tilde{F}^{\mu\nu} = -g_{a\gamma\gamma} a \vec{E} \cdot \vec{B}. \quad (1.49)$$

The equality is explicitly derived in appendix A of Ref. [7]. This expression becomes useful when dealing with the axion conversion into photons in a detector, such as a microwave cavity.

Eq. (1.49) has exactly the same form as the Primakoff process [27], that was first introduced to account for the π^0 production through a two-photon interaction (in that case the field a is substituted by the π^0 field). The decay of π^0 into two photons is called inverse Primakoff process. Now, in the framework of the Standard Model and with the QFT formalism, we know that this decay can happen through a triangle diagram with a virtual fermion in the loop, shown in Fig. 1.2, and it is valid for any pseudoscalar meson

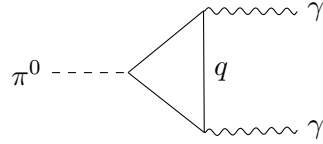


Figure 1.2: Decay of neutral pion into two photons through a quark loop. This is analogous to the triangle diagram 1.1 that gives the chiral anomaly with QCD.

decaying into two photons. This diagram is of the same form as the one in Fig. 1.1, and indeed the major contribution to the neutral pion decay comes from the chiral anomaly with QED⁶. Therefore the axion is subject to the same interaction, because it inherits the electromagnetic interactions from the mixing with the pion and η meson. When axions are produced by two photons, this is called Primakoff effect, as in the case of π^0 production. The two diagrams representing these processes are drawn in Fig. 1.3. In this case the loops receive contributions from both chiral anomaly with QED and with QCD. Although axions



Figure 1.3: (a) Axion decay into two photons via inverse Primakoff effect. (b) Axion production via Primakoff effect in vacuum.

can also have interactions with matter fields, the electromagnetic interactions through Primakoff processes are extremely important in experimental searches for axions. They provide both a detection technique and a production mechanism. The Primakoff effect of Fig. 1.3b could be responsible for an axion flux from stars, since in their cores many photons are produced via nuclear fusions. As we will see in section 1.2.2, axion fluxes from stars can be used to obtain bounds on the $g_{a\gamma\gamma}$ coupling. On the contrary, the inverse Primakoff effect of Fig. 1.3a is the paradigm of axion detection. This can be exploited substituting a real outgoing photon with an external static magnetic field, that provides virtual photons but is treated as a classical electromagnetic field. This situation is depicted in Fig. 1.4. However, if ingoing axion line and outgoing photon line are exchanged in the diagram of Fig. 1.4, this could account for a production mechanism in some regions of the universe where high magnetic fields are achieved, such as pulsar magnetospheres or AGNs.

⁶The reason why I didn't say this before is that QED has not a complicated vacuum structure, so the surface integral of a total derivative $\partial_\mu K^\mu$ appearing in the Noether's current conservation equation is really zero, thus the term doesn't contribute to the action S and can be neglected in the Lagrangian. Nonetheless, it has observable effects.

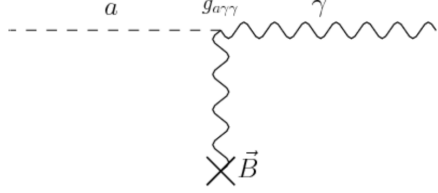


Figure 1.4: The conversion of an axion into a photon stimulated by an external static magnetic field. Taken from [7].

1.2.1 Axion parameter space

In the models described in Sec. 1.1.4, essentially the only free parameter encountered for the axion is f_a , the energy scale of the PQ transition. Then, model-dependent parameters can be defined as a function of f_a , the most important ones being the mass m_a and the axion-photon coupling $g_{a\gamma\gamma}$. Taking eq. (1.43), we can write more generally:

$$m_a = \frac{m_{\pi^0} f_\pi}{f_a} \frac{\sqrt{m_u m_d}}{(m_u + m_d)}. \quad (1.50)$$

Although its value depends on the assumption made on f_a by the model, the form of eq. (1.50) is model-independent. Recalling the definition of the coupling constant $g_{a\gamma\gamma}$:

$$g_{a\gamma\gamma} = \frac{\alpha_{\text{em}}}{\pi} \frac{K_{a\gamma\gamma}}{f_a},$$

we see that for these "QCD axion" models both $g_{a\gamma\gamma}$ and m_a are inversely proportional to f_a , therefore $g_{a\gamma\gamma} \propto m_a$. The parameter space for the electromagnetic interaction is the ($g_{a\gamma\gamma}$ vs. m_a) plane. This is shown in Fig. 1.5. The yellow band is called **model band** and it accounts for QCD axion models, such as KSVZ and DFSZ models (treated in Sec. 1.1.4), where $g_{a\gamma\gamma}$ is proportional to m_a . To understand why it is a band, let's write the mass in the following form:

$$m_a = \frac{m_{\pi^0} f_\pi}{f_a} \frac{\sqrt{z}}{1+z}, \quad (1.51)$$

where $z = m_u/m_d$ is the light quark mass ratio. From [9], its central value is $z = 0.48$, but it can take any value in the interval $0.40 < z < 0.55$, resulting in a range of possible values for the mass. Moreover, $g_{a\gamma\gamma}$ depends on the values that $K_{a\gamma\gamma}$ can take. In section 1.1.4 the expression of $K_{a\gamma\gamma}$ was given for the PQWW model, but more generally for invisible axion models it can be written in the form [28]:

$$K_{a\gamma\gamma} = \frac{1}{2} \left(\frac{E}{N} - \frac{2}{3} \frac{4+z}{1+z} \right), \quad (1.52)$$

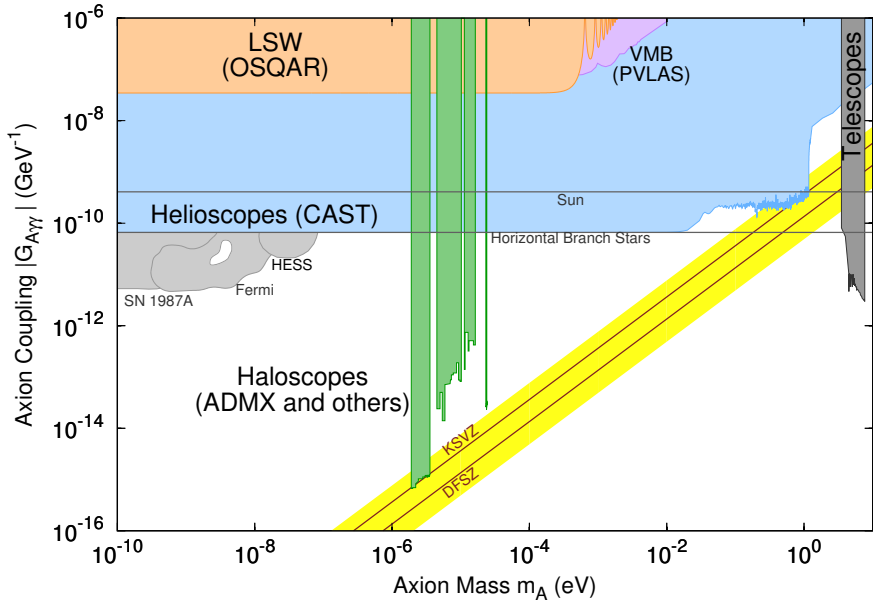


Figure 1.5: Parameter space ($g_{a\gamma\gamma}$ vs. m_a), with exclusion plots by some experiments and astrophysical bounds. In yellow the model band is shown, with KSVZ and DFSZ models marked, haloscope experiments are shown in green, while the blue and orange areas are, respectively, the bounds from helioscopes and LSW experiments. Downloaded from <http://pdg.lbl.gov>, Ref. [9].

where E and N are, respectively, the electromagnetic and color anomaly coefficients, in analogy with the ξ coefficient introduced in eq. (1.45). For instance, $E \neq 0$ when the theory possesses at least one quark charged under both $U(1)_{PQ}$ and $U(1)_{EM}$, so that it can have an axion-quark vertex and a quark-photon vertex, necessary to the diagrams of Fig. 1.3 to exist. For the KSVZ model the new quark does not possess $U(1)_{EM}$ charge, therefore $E = 0$.

For a fixed value of z , there will be different straight lines in the plot, corresponding to different models that have distinct values of the ratio E/N . In Fig. 1.5 two lines are reported: the one for KSVZ model, for which $E/N = 0$, and the one for DFSZ model, that has $E/N = 8/3$. However the ratio E/N is not exactly known, and this allows to define a band of values for $g_{a\gamma\gamma}$ as a function of the mass m_a , the yellow region in the plot.

The region below the model band in the parameter space accounts for other QCD axion models [29], while all the other regions account for Axion-like Particles (ALPs). These are pseudo-Goldstone bosons of any other theory where some symmetry is broken, but the breakdown is not due to chiral anomaly. Here the coupling constant $g_{a\gamma\gamma}$ is not necessarily proportional to the mass, because in principle these two quantities are independent of each other. So, should an experiment not be sensitive to QCD axions, it can still put limits on ALPs parameters.

Finally, we can say that this is an exclusion plot. In fact the coloured regions (except

the yellow one) represent the limits put on axion parameters by various experiments. LSW, helioscopes and haloscopes all refer to different detection techniques, described in Sec. 1.2.5. There are also bounds from astrophysical observations (Sun, SN1987A etc.), some of which are discussed in the next section.

1.2.2 Astrophysical bounds

Constraints on axion (or more generally ALPs) mass and couplings are obtained from astrophysical observations. In fact, assuming that axions exist, they could be produced in astrophysical objects and affect their evolution. The production mechanisms mainly relies on the Primakoff effect: considering a star, axions can be generated in their core if a photon interacts with the Coulomb field of the plasma, $\gamma + Ze \rightarrow Ze + a$. Then since axions are expected to interact very weakly with SM particles, they can escape the core and then the surface, providing a non-standard energy loss mechanism for stars. If the data from measurements on stellar evolution match the predicted rate of standard energy loss, a stringent bound on the axion coupling can be extracted. If the Primakoff effect is assumed, the bound is put on $g_{a\gamma\gamma}$. There are also other processes for axion production, like the nucleon bremsstrahlung $N + N \rightarrow N + N + a$ and electron bremsstrahlung $e + e \rightarrow e + e + a$. The former is a typical ALP production process in neutron stars and Supernovae. Processes involving matter can constrain the couplings g_{aee} and g_{aNN} .

Let us now introduce the form of the interaction between axions and fermions. From eq. (1.41) we saw that it must be a derivative coupling; it can be written as follows (I refer to [1] for notation convenience, but a derivation is given in [30]):

$$\mathcal{L}_{aff} = \frac{\partial_\mu a}{2f_a} \sum_f C_{aff} (\bar{\Psi}_f \gamma^\mu \gamma_5 \Psi_f), \quad (1.53)$$

where Ψ_f is a fermion Dirac field and C_{aff} are model-dependent dimensionless coupling constants. The interaction can be equivalently written as an effective, CP-conserving, Lagrangian term:

$$\mathcal{L}_{aff} = -i g_{aff} a (\bar{\Psi}_f \gamma_5 \Psi_f), \quad (1.54)$$

having defined the (yet dimensionless) coupling constant g_{aff} as:

$$g_{aff} \equiv \frac{C_{aff} m_f}{f_a}, \quad (1.55)$$

with m_f the mass of the fermion entering the interaction.

In the following I summarize some of the astrophysical bounds. All the values and arguments in this section are taken from [9], [1] and [26]; for more details on the data used for constraints see references therein. The most obvious star that can be exploited

to constrain axion parameters is our Sun. Due to the Primakoff effect, axions can be produced in the core and emitted as a flux, whose luminosity L_a is proportional to $g_{a\gamma\gamma}^2$ and the Sun luminosity L_\odot [9]. From observations of solar luminosity, neutrino solar flux and helioseismology it turns out that $L_a \lesssim 0.1L_\odot$, giving the constraint of $|g_{a\gamma\gamma}| \lesssim 4.1 \cdot 10^{-10} \text{ GeV}^{-1}$. This is reported in Fig. 1.5 as the horizontal line called "Sun". One can also attempt to directly measure the solar axion flux; this is discussed in Sec 1.2.5.

A more restrictive bound comes from the study of the Horizontal Branch (HB) of the colour-magnitude diagram of Globular Clusters (GC). Globular Clusters contain many stars with the same age, so their different stage of evolution is due to their masses. The HB stage corresponds to the helium-burning phase; if axions undergo Primakoff effect, they take away energy and as a result the duration of the HB phase is shortened. Comparing the number count of HB stars with the number count of Red Giant Branch (RGB) stars, yields the upper bound $|g_{a\gamma\gamma}| \lesssim 6.6 \cdot 10^{-11} \text{ GeV}^{-1}$ (at 95% CL). This can be converted into limits for f_a and the mass if a value of E/N is fixed. For KSVZ axions ($E/N = 0$) they are $f_a \gtrsim 3.4 \cdot 10^7 \text{ GeV}$ and $m_a \lesssim 0.2 \text{ eV}$. The limit on $|g_{a\gamma\gamma}|$ is represented in Fig. 1.5 with the name "Horizontal Branch Stars".

More important is the observation of the SN1987A Supernova [9]. The duration of the neutrino burst measured on Earth would have been much shorter if axions interacted quite efficiently with nucleons through nucleon bremsstrahlung $N + N \rightarrow N + N + a$. In this case the coupling with nucleons is constrained; assuming that the coupling to neutrons g_{ann} is zero, it is found that the axion-proton coupling is $|g_{app}| \lesssim 6 \cdot 10^{-10}$, while f_a and the mass are limited to $f_a \gtrsim 4 \cdot 10^8 \text{ GeV}$ and $m_a \lesssim 16 \text{ meV}$. Additionally, SN1987A also allows to bound the axion-photon coupling if the mass is very small; in fact axions could be produced in the core via Primakoff effect, and then could reconvert into photons in the intergalactic magnetic field. The lack of a γ -ray peak in correspondence with the neutrino pulse permits to constrain $|g_{a\gamma\gamma}| \lesssim 5.3 \cdot 10^{-12} \text{ GeV}^{-1}$ for masses $m_a \lesssim 4.4 \cdot 10^{-10} \text{ eV}$. This bound is shown in Fig. 1.5 as "SN1987A".

Concerning the coupling to electrons, the processes that contribute to an energy loss in stars are ABC processes, namely axio-recombination ($e + Z \rightarrow (Z, e) + a$), axio-bremsstrahlung due to electrons ($e + e \rightarrow e + e + a$) and Compton scattering ($e + \gamma \rightarrow e + a$). These processes only rise in DFSZ models. The excessive period decrease of pulsating White Dwarfs (WDs) can be thought of as a hint for a non-standard energy loss mechanism, and in addition to the study of GC stars it can be given the limit $|g_{aee}| \lesssim 2.6 \cdot 10^{-13}$ (at 95% CL). With order of magnitude arguments from eq. (1.55), being C_{aff} of $\mathcal{O}(1)$, this bound is translated in $f_a \gtrsim 10^{10} \text{ GeV}$ and $m_a \lesssim \text{meV}$.

To conclude with observational bounds I also want to cite, without any detail, an example of cosmological constraint, exploiting the CMB data. Photons of the CMB could produce axions if they interact with intergalactic magnetic fields or with electric fields present in the intracluster plasma, via Primakoff processes. This would lead to distortions

in the CMB spectrum.

Finally, in the hypothesis that axions constitute Cold Dark Matter (CDM) (explored in the next section), one of the requests that they must satisfy is to be stable particles, i.e. they should have a decay time greater than the age of the universe. The axion decay is the same as for the neutral pion, through two photons. It can be shown that axions become stable in the universe time-scale if (in the KSVZ model) the mass is $m_a \lesssim 20$ eV.

1.2.3 Axion cosmology

In order to justify the presence of Cold Dark Matter, one needs to find a mechanism for its production in a certain early cosmological era. In this regard, axions can account for a part or the entirety of CDM thanks to the PQ mechanism, called the *misalignment mechanism* when considered as a cosmological process, and is not a thermal production mechanism. Remarkably, when imposing that the observed Dark Matter density do not exceed the observed value, an upper limit on f_a (and thus a lower limit on m_a) is obtained.

The equation that describes the dynamics of a scalar field in an expanding universe is [31]:

$$\ddot{a} + 3H(t)\dot{a} + m_a^2(t)a = 0, \quad (1.56)$$

where the axion field a has been considered as the scalar field of interest and $H(t)$ is the Hubble parameter. If H and m_a were constant, this would be simply the equation of a damped harmonic oscillator. The field dynamics depend on the value of $m_a(t)$ with respect to $H(t)$ [31, 7]. When $H(t) \gg m_a(t)$ the mass term can be neglected and the solution consists of a constant, homogeneous field a_i . Note that this initial value corresponds to a value θ_i ($a_i = -\theta_i f_a$ from eq. (1.38)) of the vacuum expectation value of the axion potential. θ_i can be a random value in the interval $[-\pi, \pi]$ and is taken when the $U(1)_{PQ}$ symmetry spontaneously breaks at an energy (or temperature) scale much greater than quark confinement, $T \sim f_a \gg \Lambda_{QCD}$, when the axion is still massless. Then, there exists a time t^* for which $H(t^*) = m_a(t^*)$ and can be considered as the time when the axion field starts its damped oscillations. For $H(t) \ll m_a(t)$ the amplitude is slowly decaying and the oscillations are almost sinusoidal. Actually, these oscillations can start only when the axion acquires a mass. This happens at a temperature scale $T \sim \Lambda_{QCD}$, when the QCD color anomaly becomes effective and the $U(1)_{PQ}$ symmetry is also explicitly broken, with the axion potential suffering from a tilt.

According to Ref. [31], the solution to eq. (1.56) in the $H(t) \ll m_a(t)$ regime is of the form $a(t) \simeq \mathcal{A}(t) \cos(m_a(t)t)$, where the amplitude $\mathcal{A}(t)$ depends on $(m_a(t)\mathcal{R}(t))^{-3/2}$, $\mathcal{R}(t)$ being the universe scale factor of the Friedmann-Robertson-Walker metric. Defining the average energy density among the universe as $\varrho_a \simeq \frac{1}{2}m_a^2\mathcal{A}^2$, it follows that this quantity has a dependence $\varrho_a \propto \mathcal{R}(t)^{-3}$ as the universe expands, and this is typical of non-relativistic fluids. This is a general result for scalar fields satisfying eq. (1.56) and produced by

a cosmological non-thermal process. Therefore, we can say that axions produced by the misalignment mechanism are candidates of Cold Dark Matter, because they behave exactly as non-relativistic matter during the expansion of the universe.

Actually, the initial value of the axion field a_i depends on the moment of the misalignment mechanism, i.e. the time at which the $U(1)_{PQ}$ symmetry is spontaneously broken. If it happens before or during the inflationary era we talk of *pre-inflation scenario*. The misalignment angle θ_i is unique, since before inflation it is required that all regions of the universe be causally connected. Moreover, the axion field is even more homogeneous after inflation. If, on the other hand, symmetry breaking occurs after inflation we talk of *post-inflation scenario*. In this case all the causally disconnected regions of the universe after inflation, called patches, could take independently different θ_i values, and this leads to *domain wall* problems [1]. The drawback of different θ_i values can however be solved if one assumes that many patches exist, so that a unique mediated value of the angle can be considered with negligible uncertainty [1]:

$$\langle \theta_i^2 \rangle = \frac{\pi^2}{3}. \quad (1.57)$$

Now the normalized energy density $\Omega_a = \varrho_a / \varrho_c$, where $\varrho_c = 3H_0^2 / (8\pi G)$ is the critical density of the universe (H_0 the Hubble constant today and G the gravitational constant), can be expressed in dependence of f_a or m_a . Since it depends also on the value of θ_i , it is "scenario-dependent". Ref. [9] reports for the pre-inflation scenario the expression:

$$\Omega_a h^2 \approx 0.12 \left(\frac{f_a}{9 \cdot 10^{11} \text{ GeV}} \right)^{7/6} \mathcal{F} \theta_i^2 \approx 0.12 \left(\frac{6 \mu\text{eV}}{m_a} \right)^{7/6} \mathcal{F} \theta_i^2, \quad (1.58)$$

where here $h = 100 \text{ km s}^{-1} \text{ Mpc}^{-1}$ and H_0 is expressed in units of h . \mathcal{F} is a factor accounting for anharmonicities in the axion potential [9]. The equation shows that Ω_a increase as the mass m_a decrease. Thus the axions cannot be too *invisible*, namely their mass cannot be too small, because the axion energy density must satisfy the observational constraint that the Dark Matter density is [32] $\Omega_{DM} h^2 \simeq 0.12$. This, indeed, can be turned into the condition $\Omega_a h^2 \lesssim 0.12$, thus yielding a lower bound to the mass:

$$m_a \gtrsim \text{few} \cdot 10^{-6} \text{ eV}. \quad (1.59)$$

This was obtained assuming $\mathcal{F} \theta_i^2 \sim \mathcal{O}(1)$. With lower mass values, axions would alone exceed the observed DM density, leading to an "overclosure" of the universe. Correspondingly, an upper bound on f_a is implied:

$$f_a \lesssim 10^{12} \text{ GeV}. \quad (1.60)$$

In conclusion, putting together the astrophysical bounds of Sec. 1.2.2 and the arguments of this section, we can take the axion mass to lie approximately in the range:

$$m_a \in (10^{-6} \div 10^{-3}) \text{ eV}. \quad (1.61)$$

However, lower mass values are still viable if one drops the assumption that $\theta_i \sim \mathcal{O}(1)$ and considers small θ_i values, but this sounds like an arbitrary assumption. Ranges of m_a and f_a obtained with $\theta_i \ll 1$ are called the *anthropic axion window* (more details can be found in [1, 7] and references therein).

1.2.4 Properties of galactic DM axions

The arguments in this section are useful to the understanding of the haloscope concept of Sec. 1.2.5.

To describe the DM halo in our galaxy we would need to specify the density distribution $\rho(\mathbf{r})$ (that also determines the mass distribution) and the energy (or velocity) distribution. However, for the scopes of a detector localized on Earth it suffices to know the value of the *local* DM density and the mean velocity and its dispersion. It is customary to assume that the axion density equals the DM local density, $\rho_a = \rho_{\text{dm}}$ ⁷. From several measurements [33] the local DM density is estimated to lie in the range $(0.2 \lesssim \rho_{\text{dm}} \lesssim 0.56) \text{ GeV cm}^{-3}$, and papers focused on axion searches usually refer to a value of $\rho_{\text{dm}} = 0.45 \text{ GeV cm}^{-3}$ [34]. For what concerns the velocity distribution, it is assumed that the galactic halo has virialized, meaning that it reached an equilibrium condition in which the kinetic and potential energies are related by the virial theorem. In this hypothesis the velocity distribution is approximately Maxwellian and can be parametrized as [35]:

$$f(v) d^3v = n_a \left(\frac{m_a}{2\pi T} \right)^{3/2} \exp(-m_a v^2 / 2T) d^3v, \quad (1.62)$$

where T is the "halo temperature" and n_a the number density of axions:

$$n_a = \frac{\rho_a}{m_a} \simeq 4.5 \cdot 10^{12} \left(\frac{10^{-4} \text{ eV}}{m_a} \right) \text{ cm}^{-3}. \quad (1.63)$$

From the distribution the second moment can be calculated: $\langle v^2 \rangle = \int v^2 f(v) d^3v$. The rms velocity of the halo, often called dispersion, is defined as $\bar{v} \equiv \langle v^2 \rangle^{1/2}$, and from Ref. [35] it is estimated to be $\bar{v} \simeq 270 \text{ km/s}$. In natural units we can take it to be $\bar{v} \sim 10^{-3}$. These quantities are expressed at the center of the galaxy, but Earth moves with respect to it with velocity \mathbf{v}_E . As a consequence the Earth is moving inside the DM halo and on a laboratory on its surface the effective axion "wind" velocity is $\mathbf{v}_a = \mathbf{v} - \mathbf{v}_E$. \mathbf{v}_E is the sum of

⁷To avoid confusion, I underline that the symbol ρ_a was used in the previous section for the average axion density, while here ρ_a indicates the local halo axion density.

the velocity of the Solar System in the galaxy (230 km/s) plus the Earth's orbital velocity about the Sun (29.8 km/s) plus its rotational velocity (0.46 km/s). Thus we can neglect the last two contributions. The axion wind velocity still follows a Maxwellian distribution, but with different parameters. Turner [35] reports the value $\bar{v}_a \simeq 305$ km/s, thus still of order $\sim 10^{-3}$. The above considerations indicate that DM particles constituting the halo are non-relativistic.

For this reason we can say that the energy of an axion is its mass energy, $E_a \simeq m_a$. In fact the halo energy dispersion about the central line is simply:

$$E_a = m_a + \frac{1}{2}m_a\bar{v}_a^2 \simeq m_a [1 + \mathcal{O}(10^{-6})], \quad (1.64)$$

Then the axion linewidth is very narrow, and is defined as:

$$\frac{dE_a}{E_a} = \frac{m_a\bar{v}_a^2/2}{m_a} \simeq 5.2 \cdot 10^{-7}, \quad (1.65)$$

and the inverse of the linewidth, that is the ratio of the energy to the energy spread, is called *figure of merit* or sometimes *quality factor*, of the galactic halo axion:

$$Q_a = \frac{m_a}{m_a\bar{v}_a^2/2} \simeq 1.9 \cdot 10^6. \quad (1.66)$$

This is a useful quantity that characterize the kinetic properties of a generic CDM galactic halo, independently of the axion mass.

Other two interesting properties are the **coherence length** and **coherence time**. To begin, consider the De Broglie wavelength of an axion, that in natural units and using the classical expression for the momentum is:

$$\lambda_a = \frac{2\pi}{m_a\bar{v}_a} \simeq 6.9 \left(\frac{200 \mu\text{eV}}{m_a} \right) \text{ m}. \quad (1.67)$$

This is of order some meters, so it allows the axion field to be treated as uniform in a region of space where an experiment is located⁸. The coherence length is related to λ_a through $\mathcal{O}(1)$ factors, but is not unusual to consider directly λ_a as the coherence length. Qualitatively the coherence length is the region of space in which the axion field can be considered spatially constant, because due to the extremely broad oscillations two points in this volume always have approximately the same phase. The coherence time, instead, is defined as:

$$\tau_a \simeq \frac{2\pi}{m_a} Q_a. \quad (1.68)$$

and is the order of magnitude of the time after which two points within the coherence

⁸In our case the microwave cavities have diameters of order some cm.

length will dephase, because the axion field is not perfectly monochromatic but possesses a frequency spectrum, albeit narrow. Anticipating the concepts of the next sections, we can think of the interaction between the axion field and a resonant cavity as a pair of coupled oscillators. The axion field triggers the resonance of the cavity only for a time $\sim \tau_a$, after which the two oscillators decouple.

1.2.5 Detection techniques

In Fig. 1.5, along with some astrophysical bounds, we saw exclusion plots of the main categories of experiments dedicated to the search for axions. These are: Light-Shining-Through-Walls (LSW) experiments, helioscopes and haloscopes, to which this section is dedicated. There are many other detection schemes, but here I focus on the most exploited ones. Ref. [1] is a complete and recent review on axion detection techniques, summarizing the most recent results in this research field.

A common point to the three detection techniques is that they make use of the axion-to-photons interaction. Before describing the experiments it is worth noting that such a coupling modifies the Maxwell's equations and the propagation of a free axion. Taking the Lagrangian:

$$\mathcal{L} = \frac{1}{2}(\partial_\mu a)^2 - \frac{1}{2}m_a^2 a^2 - \frac{1}{4}F_{\mu\nu}F^{\mu\nu} + \frac{1}{4}g_{a\gamma\gamma}a F_{\mu\nu}\tilde{F}^{\mu\nu},$$

with $F_{\mu\nu} = \partial_\mu A_\nu - \partial_\nu A_\mu$, A_μ the photon vector field, and using the Euler-Lagrange equations for A_μ and a one obtains in the absence of electromagnetic charges [7]:

$$\begin{aligned} \nabla \cdot \mathbf{E} &= g_{a\gamma\gamma} \mathbf{B} \cdot \nabla a \\ \nabla \cdot \mathbf{B} &= 0 \\ \nabla \wedge \mathbf{E} + \partial_t \mathbf{B} &= 0 \\ \nabla \wedge \mathbf{B} - \partial_t \mathbf{E} &= g_{a\gamma\gamma} (\mathbf{E} \wedge \nabla a - \mathbf{B} \partial_t a), \end{aligned} \tag{1.69}$$

$$(\square + m_a^2) a = -g_{a\gamma\gamma} \mathbf{E} \cdot \mathbf{B}. \tag{1.70}$$

Then in eq. (1.69) the axion field is regarded as a source of electromagnetic fields, and vice versa in eq. (1.70), where the solution gives the axion field in terms of an electric and a magnetic field. The experiments here described exploit both interactions.

LSW experiments

Light-Shining-Through-Walls experiments are conceptually very simple to understand, since they use Primakoff process to produce an ALP and then inverse Primakoff process to reconvert them in a photon. The scheme of this process is given in Fig. 1.6. A photon beam is injected in an optical cavity, in presence of a static magnetic field that provides

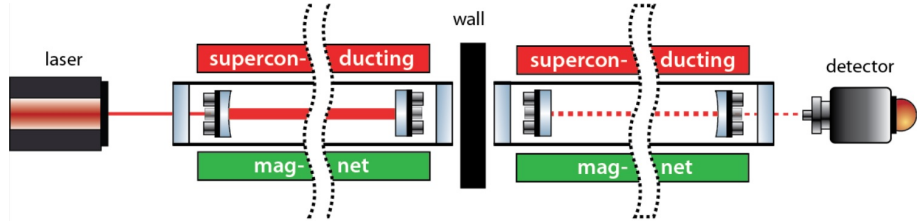


Figure 1.6: Sketch of an LSW experiment. Source: ALPS experiment website, <https://alps.desy.de/>.

a virtual photon. If an ALP is produced, it can pass the opaque wall without interacting with it and reach the second cavity. Here another magnetic field is applied to stimulate the conversion of the ALP into a standard photon. Usually, lasers with optical frequencies are used, but microwave LSW experiments also exist. The probability of the transition $\gamma \rightarrow a \rightarrow \gamma$ is [26]:

$$P(\gamma \rightarrow a \rightarrow \gamma) = 16 \frac{(g_{a\gamma\gamma} B \omega \cos \theta)^4}{m_a^8} \sin^2 \left(\frac{l_1 m_a^2}{4\omega} \right) \sin^2 \left(\frac{l_2 m_a^2}{4\omega} \right), \quad (1.71)$$

where θ is the angle between the laser polarization and the magnetic field, ω the laser frequency, B the static magnetic field and l_1, l_2 the lengths of the production and reconversion regions, respectively. Then this type of experiment is sensitive to different mass values if the ratios l_i/ω are tuned opportunely. The probability can be enhanced if optical resonant cavities (Fabry-Perot) are employed in the production and regeneration regions.

Two experiments are currently using LSW techniques, ALPS (Any Light Particle Search) at DESY and OSQAR at CERN. They use dipole accelerator magnets: ALPS-I employed HERA magnets providing a 5 T field and OSQAR employs CERN magnets giving 8 T. Only ALPS-I made use of resonant cavities in both regions, and thanks to that it reached a sensitivity of about $5 \cdot 10^{-8}$ GeV $^{-1}$ on $g_{a\gamma\gamma}$ for masses below meV, while OSQAR reaches $g_{a\gamma\gamma} \sim 3.5 \cdot 10^{-8}$ GeV $^{-1}$. Although these values are much smaller than that from astrophysical sources, the ALPS-II upgrade could reach comparable sensitivities, namely $g_{a\gamma\gamma} \sim 2 \cdot 10^{-11}$ GeV $^{-1}$. ALPS-II will use magnets in a longer region and will exploit single photon detectors.

The next two classes of experiments are actually the first detection techniques to be proposed for the direct detection of the so-called invisible axions, described in Sec. 1.1.4. The techniques were proposed by Sikivie in 1983 [6], and further elaborated in 1985 by Sikivie [36] and Krauss, Moody, Wilczek, Morris [37], after the models with $f_a = 246$ GeV (the electroweak scale) were ruled out by experiment.

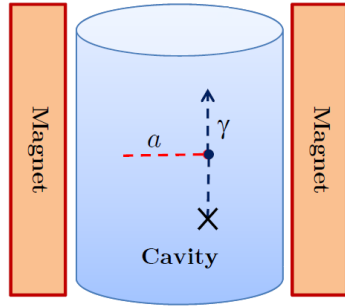


Figure 1.7: A sketch of a microwave cavity in which an axion-photon conversion occurs. Taken from [1].

Conventional haloscopes

Haloscopes are intended to detect axions constituting the galactic DM halo (Sec. 1.2.4), hence the name *halo*-scopes, in the hypothesis that all or part of the measured DM density is explained by axions. The detection technique relies on the inverse Primakoff process $a + \gamma^* \rightarrow \gamma$, where the virtual photon is provided by a static magnetic field. In this case the emitted photon is collected in a microwave cavity and then the signal is read by some electronics (Fig. 1.7). The resonant frequency of the cavity has to be matched to the photon energy, in which case it can excite a cavity mode. The photon energy is equal to the axion energy, $\nu_{\text{res}} = E_a$, because when a magnetic field is static, it is considered as constituted by many virtual photons, so when a single photon interacts the energy transfer is negligible. In turn, because the axion is non-relativistic as seen in Sec. 1.2.4, its energy is equal to its rest mass, $E_a \simeq m_a$; then we can safely state that the photon frequency must equal the axion mass: $\nu_{\text{res}} \simeq m_a$ ⁹. For this reason a microwave cavity must have the possibility to vary somehow its resonant frequency, to scan over a range of axion masses as wide as possible. In Chap. 2 I will describe in some more detail the properties of microwave cavities. However it is important to mention two things at this point. First, if \hat{z} is the axis direction of the cavity and the external magnetic field is applied along \hat{z} , the only cavity modes that can be excited by an axion conversion are TM_{nm0} , transverse magnetic modes, for which the electric field has component along the \hat{z} axis [36]. This is a consequence of the form of the interaction seen in eq. (1.49). Secondly, to scan higher mass values, larger frequencies are needed. This implies smaller cavity volumes, since ν_{res} is inversely proportional to the geometric parameters of the cavity (Sec. 2.3).

ADMX (Axion Dark Matter eXperiment) has become the paradigm of axion searches with haloscopes. The experiment has been built in 1995 and is still running and improving its performances. [1, 38] ADMX employs a NbTi superconducting magnet up to 8 T, with a bore of 60 cm \times 110 cm. The copper microwave cavity has a volume of about 200 L

⁹More precisely we should talk of pulsation ω_{res} , because it was used the notation $\hbar = 1$.

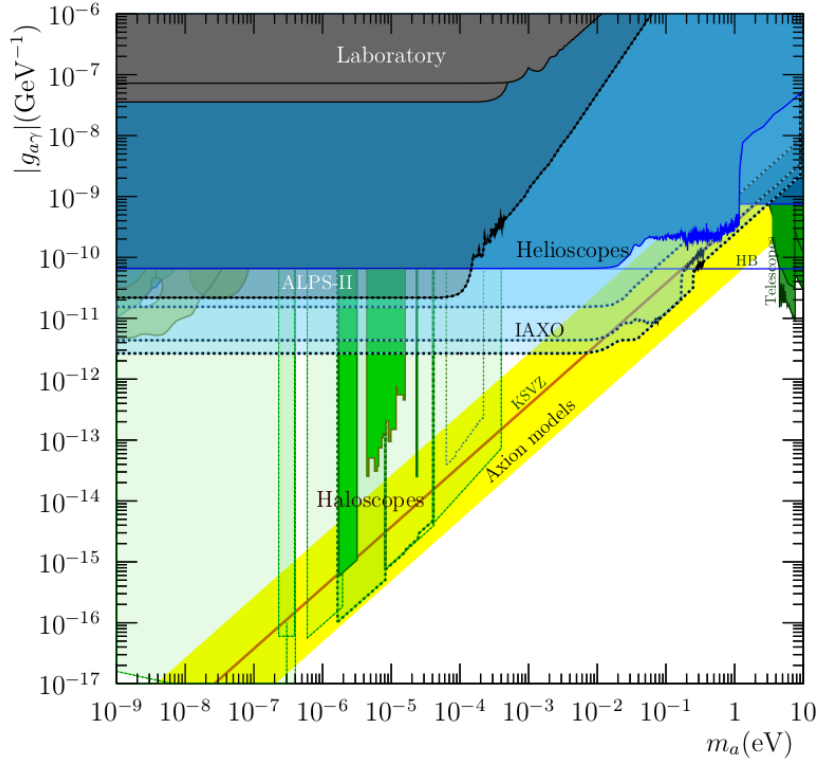


Figure 1.8: Another version of the ($g_{a\gamma\gamma}$ vs. m_a) plane, showing the major categories of axion searches. Semi-transparent regions correspond to future experiments. Source: [1].

and can reach a quality factor¹⁰ of $Q \sim 10^5$. The entire volume is brought to cryogenic temperatures, of order $T \sim K$, to reduce the thermal noise. Inside the cavity there are two movable rods that allow to tune the resonant frequency approximately in the range (0.46÷2) GHz, that corresponds to the mass range (1.9÷8.26) μ eV. With its measurements ADMX managed to reach the sensitivity to the KSVZ axions in the $g_{a\gamma\gamma}$ exclusion plot in the mass range (1.9 ÷ 3.65) μ eV [1, 38]. This result is reported in Fig. 1.8 (that is an alternative version of Fig. 1.5) as the green area that goes down to the KSVZ line, where a sensitivity of $g_{a\gamma\gamma} \sim 10^{-15}$ GeV $^{-1}$ is achieved. Recently [39] ADMX improved its sensitivity and managed to exclude also a slice of the DFSZ axion model parameter space, reaching values of about $g_{a\gamma\gamma} \sim 3 \cdot 10^{-16}$ GeV $^{-1}$ for the mass range (2.67 \lesssim m_a \lesssim 2.8) μ eV.

In the future the ADMX collaboration will scan higher frequencies, ~ 2 GHz corresponding to about 8 μ eV, and plans to reach up to 10 GHz. In the landscape of lower frequencies the KLASH (KLoe magnet for Axion Search) experiment [40] has been proposed; the project plans to employ the KLOE magnet of 0.6 T for a copper cavity of about 35 m 3 , going down to 57 MHz ($m_a \sim 0.2$ μ eV) with predicted sensitivity of about $g_{a\gamma\gamma} \sim 6 \cdot 10^{-17}$ GeV $^{-1}$. More generically, improvements and upgrades are planned for

¹⁰The quality factor is defined in Sec. 2.2.1. Qualitatively it is the ratio between the energy stored in the cavity and the power dissipated by it.

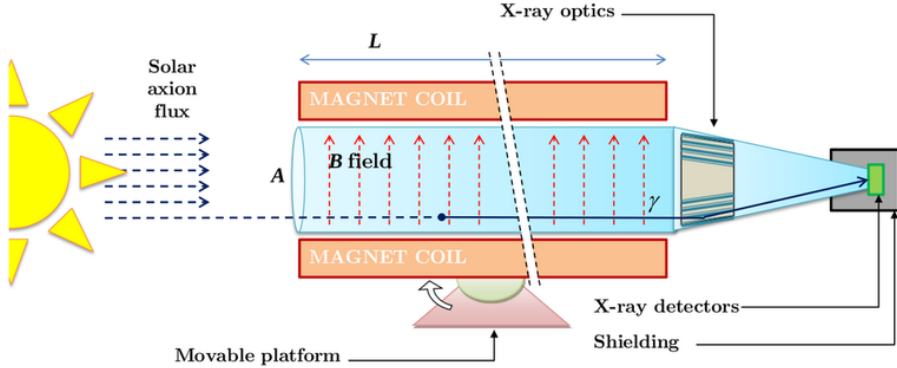


Figure 1.9: Conceptual scheme of an helioscope pointing the Sun, in which an intense magnetic field is applied. Taken from [1].

all the components of a haloscope. These include ultra-high magnetic fields, low noise receivers trying to surpass the quantum limit, cavities made of superconducting materials to achieve higher Qs, and new cavity designs. CAPP (Center for Axion and Precision Physics) in South Korea is active in all these technological challenges within its R&D program [1].

Helioscopes

Helioscopes exploit essentially the same mechanism as LSW experiments, but in this case the source of axions is our Sun. The production process is again the Primakoff effect $\gamma + \gamma^* \rightarrow a$, schematically shown in Fig. 1.4, but in this case the role of an external field is played by the Coulomb field of the plasma. The photon regeneration takes place in a lab, as in the LSW scheme; intense static magnetic fields are applied for the conversion within a movable structure similar to telescopes, pointed towards the Sun. A scheme of this set-up can be seen in Fig. 1.9. Sikivie pointed out [6, 36] that the magnetic field has to be applied in an orthogonal direction with respect to the axion flux, in which case the direction of the generated photon polarization vector is parallel to B_0 . This is necessary to have an electromagnetic interaction with the axion, as its form (eq. (1.49)) suggests.

The temperatures in the core of the Sun are around the \sim keV, so axions with energies in the keV range are produced herein. Subsequently, in the lab, keV axions convert into x-ray photons, and for this reason modern helioscopes are equipped with x-ray focusing optics and x-ray detectors. The differential flux of ALPs at Earth in the 1-11 keV range, due only to the Primakoff process, is [1]:

$$\frac{d\Phi_a}{dE} = 6.02 \cdot 10^{10} \left(\frac{g_{a\gamma\gamma}}{10^{-10} \text{ GeV}^{-1}} \right)^2 E^{2.481} e^{-E/1.205} \frac{1}{\text{cm}^2 \text{s keV}}, \quad (1.72)$$

with E the ALP energy in keV. The peak is at about 3 keV. Thanks to the large number

of photons inside the Sun a high flux of ALPs is expected. However the small coupling $g_{a\gamma\gamma}$ ensures that the flux is not too high, or the Sun would loose energy too fast with significant impact on its evolution.

The reference helioscope experiment still running is CAST (CERN Axion Solar Telescope), that put the most severe constraints among helioscopes until now. [41] It employs a powerful dipole magnet designed by INFN for LHC, up to 9 T over a length of 9.3 m, and the structure is able to track the Sun for some hours. It is also equipped with x-ray optics to focus the photons on the detector. CAST took data in various phases, and the last one gives an upper limit on $g_{a\gamma\gamma}$ comparable to astrophysical bounds. This is [1] $|g_{a\gamma\gamma}| \lesssim 0.66 \cdot 10^{-10}$ GeV (95% CL) for masses $m_a \lesssim 0.02$ eV, and is also reported in Fig. 1.8 as "Helioscopes". Remarkably, for higher masses ($m_a \gtrsim 0.1$ eV) CAST data allowed to reach and exclude part of the QCD axions model band, including part of the KSVZ parameter space.

The improvements that have been planned for CAST will converge in a new project, IAXO (International AXion Observatory). To achieve a better sensitivity and signal-to-noise ratio the performances of the magnet have to be improved. These include the strength of the magnetic field, the length over which it is applied and the cross sectional aperture area of the coils. Together with the magnet, also improvements in x-ray optics and detectors are necessary. The sensitivity on $g_{a\gamma\gamma}$ expected for IAXO is more than one order of magnitude better than CAST's one, and is drawn in Fig. 1.8 as the "IAXO" semi-transparent area.

In the next chapter I will present the QUAX experiment, that will be part of the category of haloscope experiments. Along with the already treated concepts, further details will be provided, like the signal power that can be extracted in a microwave cavity due to an axion interaction.

CHAPTER 2

QUAX R&D at LNF

2.1 The QUAX experiment

QUAX is an experiment aiming at detecting galactic halo axions assuming that they constitute a dominant component of DM, therefore it can be included in the category of haloscopes. As conventional haloscopes, it employs microwave cavities, magnets, cryogenic systems etc. QUAX can operate in two ways: one is exactly the conventional haloscope set-up, alike ADMX, but the novelty of this experiment is the second way of operation. This consists in the employment of magnetized media to exploit the coupling of the axion to the electron spin, as first proposed by Krauss *et al.* [37] in 1985. They stressed that aligned electron spins are catalysts of the axion-photon conversion, and having a spin density of $n_s \sim 10^{23} \text{ cm}^{-3}$ would be equivalent to applying a 270 T magnetic field in a conventional haloscope. This idea was resumed by Barbieri *et al.* [42] in the QUAX proposal. This type of experiments are therefore sensitive to the coupling g_{aee} , but only to DFSZ models, since KSVZ axions don't couple with leptons. In Ref. [42] it was proposed to operate at a frequency of 48 GHz ($m_a \sim 200 \mu\text{eV}$), but for practical and economical reasons the parameters of the QUAX R&D were scaled-down to 14 GHz ($\sim 58 \mu\text{eV}$) [43].

This research activity is divided between LNF (Laboratori Nazionali di Frascati), where the main focus is on the study of new superconducting microwave cavities, and LNL (Laboratori Nazionali di Legnaro), where magnetized media are already employed. At LNL a preliminary test of the apparatus has already been carried out, yielding an upper limit on the coupling of DFSZ axions to electrons of $g_{aee} < 4.9 \cdot 10^{-10}$ (at 95% CL) for a mass $m_a = 58 \mu\text{eV}$ ($\sim 14 \text{ GHz}$) [43].

2.1.1 Coupling to electrons and detection technique

The derivation of the coupling to electron spins starts from the interaction of the axion to electrons, given by the Lagrangian of eq. (1.54):

$$\mathcal{L}_{aee} = -i g_{aee} a (\bar{\Psi} \gamma_5 \Psi),$$

where now $\Psi(x)$ is an electron spinor and g_{aee} is a dimensionless coupling constant. Including also the Lagrangian for the free electron¹ $\bar{\Psi}(i\hbar\gamma^\mu\partial_\mu - m_e c)\Psi$, the equation of motion of an electron in presence of the axion field in the non-relativistic limit is [42]:

$$i\hbar \partial_t \varphi = \left[-\frac{\hbar^2}{2m} \nabla^2 - \frac{g_{aee}\hbar}{2m} \boldsymbol{\sigma} \cdot \boldsymbol{\nabla} a \right] \varphi, \quad (2.1)$$

where φ is a two component field, m the electron mass and $\boldsymbol{\sigma}$ the vector of the Pauli matrices. The last term on the r.h.s. of the equation has the form of an interaction between the spin magnetic moment and a magnetic field (as in the Zeeman effect in atomic physics), since it can be rewritten as:

$$-\frac{g_{aee}\hbar}{2m} \boldsymbol{\sigma} \cdot \boldsymbol{\nabla} a = -2 \frac{e\hbar}{2m} \boldsymbol{\sigma} \cdot \left(\frac{g_{aee}}{2e} \right) \boldsymbol{\nabla} a \equiv -2\mu_B \boldsymbol{\sigma} \cdot \boldsymbol{B}_a, \quad (2.2)$$

$\mu_B = (e\hbar)/(2m)$ is the Bohr magneton, and an effective oscillating magnetic field has been defined: $\boldsymbol{B}_a \equiv (g_{aee}/2e)\boldsymbol{\nabla} a$. Then the electron spins see the axion wind as an external oscillating field that will change their magnetization.

The properties of the B_a field can be obtained by the axion field. After the arguments of Sec. 1.2.4, the axion field can be written as a plane wave, approximately monochromatic [42]:

$$a(\mathbf{x}, t) \simeq a_0 \cos \left(\frac{p^0 ct - \mathbf{p}_a \cdot \mathbf{x}}{\hbar} \right), \quad (2.3)$$

with $\mathbf{p}_a \simeq m_a \mathbf{v}_a$ the classical momentum, $cp^0 = \sqrt{m_a^2 c^4 + |\mathbf{p}_a|^2 c^2} \approx m_a c^2 + |\mathbf{p}_a|^2 / 2m_a$, and $a_0 = \sqrt{(n_a \hbar^3)/(m_a c)}$ the field amplitude. n_a is the number density of axions (1.63), but in the QUAX experiment $\rho_{DM} = 0.3 \text{ GeV cm}^{-3}$ is assumed for the DM halo density, so n_a becomes $n_a \simeq 3 \cdot 10^{12} (10^{-4} \text{ eV}/m_a) \text{ cm}^{-3}$. Taking the gradient of the axion field yields the expression of the effective magnetic field:

$$\boldsymbol{B}_a = \frac{g_{aee}}{2e} \left(\frac{n_a \hbar}{m_a c} \right)^{1/2} \mathbf{p}_a \sin \left(\frac{p^0 ct - \mathbf{p}_a \cdot \mathbf{x}}{\hbar} \right). \quad (2.4)$$

In the framework of the DFSZ model, assuming a coupling constant of $g_{aee} \simeq 3 \cdot 10^{-11} (m_a/(1 \text{ eV}))$ and putting the magnetic material in $\mathbf{x} = \mathbf{0}$, the field mean amplitude and the frequency

¹In this section the factors \hbar and c are restored.

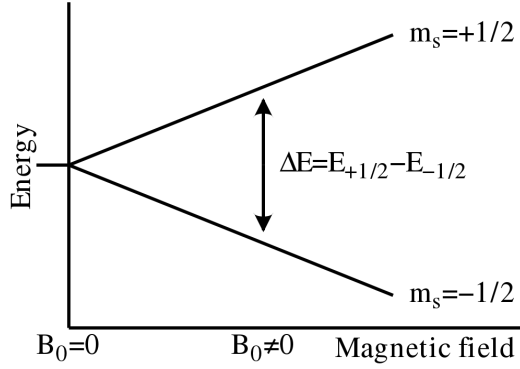


Figure 2.1: The energy splitting of an atom with unpaired spin in the presence of an external magnetic field. Downloaded from <https://www.wikipedia.org/>.

of \mathbf{B}_a take the following values [42]:

$$\begin{aligned} B_a &= 2 \cdot 10^{-22} \left(\frac{m_a}{200 \mu\text{eV}} \right) \text{ T}, \\ \nu_a &= 48 \left(\frac{m_a}{200 \mu\text{eV}} \right) \text{ GHz}. \end{aligned} \quad (2.5)$$

ESR technique. The detection technique exploits the Electron Spin Resonance (ESR), that is a spectroscopic technique used to study electronic properties of atoms with unpaired spins. When a single electron is subject to an external static magnetic field B_0 , the magnetic moment of the electron aligns with it and two states are accessible, those corresponding to the two spin projections along the field direction. Consider a magnetic field directed along the \hat{z} direction; the magnetic energy for a single electron can be written as $U = -\boldsymbol{\mu} \cdot \mathbf{B}_0$, where $\boldsymbol{\mu} = g_s \frac{(-e)\hbar \mathbf{s}}{2m} \hbar$ is the spin magnetic moment and \mathbf{s} the spin operator ($g_s = 2$ the electron giromagnetic factor). After the alignment the energy becomes $U = -\mu_z B_0 = g_s B_0 \mu_B m_s$, with $m_s = \pm 1/2$ the spin projection along the \hat{z} direction. The lower level occurs for $m_s = -1/2$, as shown in Fig. 2.1. The two levels differ by the amount $\Delta U = U_+ - U_- = g_s B_0 \mu_B$, that assuming $g_s = 2$ is exactly h times the Larmor frequency ν_L :

$$\begin{aligned} \Delta U &= g_s B_0 \mu_B = h \nu_L, \\ \nu_L &= \frac{e}{2\pi m} B_0. \end{aligned} \quad (2.6)$$

Usually, in atomic physics, the electron changes its energy by absorbing or emitting a photon having the Larmor frequency. In this case one hopes to have a transition caused by an axion interaction, thus the energy difference of the two levels must be equal to the

axion energy, i.e. its mass energy, $E_a \simeq m_a c^2$. Therefore imposing that:

$$\Delta U = h\nu_L = m_a c^2,$$

we see that the static magnetic field B_0 has to be properly tuned, depending on what is the value of the axion mass to search for:

$$B_0 = m_a c^2 \frac{m}{\hbar e} \simeq 1.7 \left(\frac{m_a}{200 \mu\text{eV}} \right) \text{ T.} \quad (2.7)$$

Then if the system initially stands in the lower state and is excited by an energy transfer due to an axion, it subsequently will re-emit the energy as radiation. It is for this reason that also the resonant frequency of the microwave cavity has to be tuned to the axion mass.

2.1.2 Signal power

The phenomenon can also be treated from a different point of view: the effects caused by the oscillating \mathbf{B}_a field on the total magnetization of the sample. From this point of view it is also straightforward to calculate the signal power that can be extracted from the cavity after an axion interaction.

The dynamics of the magnetization \mathbf{M} of a magnetic material are described by the Bloch equations including also dissipations and radiation damping [42]:

$$\begin{aligned} \frac{dM_x}{dt} &= \frac{e}{m} (\mathbf{M} \wedge \mathbf{B})_x - \frac{M_x}{\tau_2} - \frac{M_x M_z}{M_0 \tau_r} \\ \frac{dM_y}{dt} &= \frac{e}{m} (\mathbf{M} \wedge \mathbf{B})_y - \frac{M_y}{\tau_2} - \frac{M_y M_z}{M_0 \tau_r} \\ \frac{dM_z}{dt} &= \frac{e}{m} (\mathbf{M} \wedge \mathbf{B})_z - \frac{M_0 - M_z}{\tau_1} - \frac{M_x^2 + M_y^2}{M_0 \tau_r}, \end{aligned} \quad (2.8)$$

where \mathbf{M} is the sum of the magnetic moments of all the electrons per unit volume, M_0 the static magnetization along the \hat{z} axis only due to the B_0 field, \mathbf{B} is an external magnetic field, and the τ s account for the natural relaxation of the spins. τ_1 and τ_2 are the longitudinal (or spin-lattice) and transverse (or spin-spin) relaxation times, respectively, while τ_r is the radiation damping time due to the reaction of the material to its own radiation.

In this case the \mathbf{B} field is just the $\mathbf{B}_a(t)$ effective field induced by the axion wind. We may think that without the presence of $\mathbf{B}_a(t)$ the medium possesses a magnetization \mathbf{M}_0 parallel to the \mathbf{B}_0 field. The axion wind causes this magnetization to change, because it acquires transverse components. This results in a precession of the spins about the B_0 direction with a Larmor frequency, and the solution of eq.s (2.8) is a time dependent

magnetization of the form [42]:

$$M_a(t) = \frac{e}{m} \mu_B B_a n_s \tau_{\min} \cos \omega_a t, \quad (2.9)$$

where B_a and ω_a are given in eq. (2.5), n_s is the spin density, and τ_{\min} is the minimum time that drives the relaxation process:

$$\tau_{\min} = \min(\tau_{\nabla a}, \tau_2, \tau_r). \quad (2.10)$$

Here $\tau_{\nabla a}$ is the coherence time associated to the gradient of the axion field, $\tau_{\nabla a} \simeq 0.68 \tau_a$, and τ_1 is not considered because it is usually greater than τ_2 . It is the magnetization $M_a(t)$ that excites the microwave cavity, being the source of the magnetic field inside it². A microwave cavity is also necessary to inhibit the radiation damping. In fact, in the cavity only specific resonant modes can be excited (see Sec. 2.3), so its phase space is limited. It follows that the radiation damping time is equal to the cavity decay time τ_c (this is defined in eq. (2.81) of Sec. 2.4). Moreover, with a high spin number, hybridization between electron spins and the cavity electromagnetic field can occur, and can be qualitatively thought as the coupling between two harmonic oscillators. The resonance curve splits into two peaks in this case. Calling $k_c = 1/\tau_c$ and $k_2 = 1/\tau_2$ the linewidth of, respectively, the cavity and the ferromagnetic resonances, the total linewidth of a single hybridized mode is [42]:

$$k_h = \frac{1}{2}(k_c + k_2).$$

Then the characteristic time of the hybridized mode is $\tau_h = 1/k_h$, and the minimum relaxation time appearing in eq. (2.9) becomes $\tau_{\min} = \min(\tau_{\nabla a}, \tau_h)$, so that radiation damping is no longer effective.

Now the average power transferred from the axion wind to the sample is $P_{\text{in}} = \mathbf{B} \cdot \frac{d\mathbf{M}}{dt}$, that in this case becomes:

$$P_{\text{in}} = B_a \frac{dM_a}{dt} V_s = \frac{e}{m} \mu_B n_s \omega_a B_a^2 V_s \tau_{\min}, \quad (2.11)$$

where V_s is the volume of the magnetic material. From conservation principles, this must be the sum of the power P_0 dissipated by the cavity walls and the power P_{sig} extracted from a photon receiver coupled to the cavity: $P_{\text{in}} = P_0 + P_{\text{sig}}$. Introducing the coupling coefficient κ as the ratio $\kappa \equiv P_{\text{sig}}/P_0$, the signal power that can be read by the receiver after an axion interaction and subsequent photon emission is:

$$P_{\text{sig}} = \frac{\kappa}{1 + \kappa} P_{\text{in}}. \quad (2.12)$$

²This derives from Maxwell's equations in the presence of a magnetization vector and in absence of current densities, as in the case of a permanent magnet that generates a magnetic field thanks to its residual magnetization \mathbf{M}_r .

The coupling coefficient will be also defined in the next paragraph and in eq. (2.48) of Sec. 2.2.1 in terms of quality factors. A receiver is said to be critically coupled when $\kappa = 1$, and in this case the power signal is finally:

$$P_{\text{sig}} = \frac{P_{\text{in}}}{2} = 3.8 \cdot 10^{-26} \left(\frac{m_a}{200 \mu\text{eV}} \right)^3 \left(\frac{V_s}{100 \text{cm}^3} \right) \cdot \left(\frac{n_s}{2 \cdot 10^{28}/\text{m}^3} \right) \left(\frac{\tau_{\min}}{2 \mu\text{s}} \right) \text{W.} \quad (2.13)$$

It is clear that this power is very tiny, so QUAX should possibly have the chance to use a single microwave photon counter to suitably detect such a signal.

Signal power for an empty cavity

As discussed earlier, QUAX could also operate in the ADMX configuration, i.e. with an external magnetic field applied in an empty cavity. The signal power in this case depends on different parameters. After an axion-photon conversion the power P_{in} transferred to the cavity must be dissipated in the cavity walls and in the receiver coupled to the microwave device, $P_{\text{in}} = P_0 + P_{\text{sig}}$. As before, P_{sig} is only a fraction of P_{in} , precisely $P_{\text{sig}} = P_{\text{in}} \kappa / (1 + \kappa)$. In this case we can express P_{in} as:

$$P_{\text{in}} = \omega_{\text{res}} \frac{U}{Q_L}, \quad (2.14)$$

where ω_{res} is the resonant pulsation, U is the electromagnetic energy stored in the cavity and Q_L a loaded quality factor. A quality factor is the ratio between the stored energy and the power losses in a cavity, and is well defined in Sec. 2.2.1. There it is shown (eq. (2.28)) that $1/Q_L = 1/Q_0 + 1/Q_r$, where Q_0 is the unloaded quality factor and takes into account the resistive losses of the cavity walls, while Q_r takes into account the additional losses introduced by the external receiver. Therefore from the general expression of P_{sig} (2.12) and eq. (2.14) we can express the power that will be read by the receiver as:

$$P_{\text{sig}} = \frac{\omega_{\text{res}} U}{Q_L} \frac{\kappa}{1 + \kappa}. \quad (2.15)$$

Now U is the energy due to an axion-to-photon conversion in the cavity. I quote the results given in Refs. [36, 37] and readapted in [7]. In natural units the energy is:

$$U = g_{a\gamma\gamma}^2 \frac{\rho_a}{m_a^2} B_0^2 V_c C_{nml} Q_L^2, \quad (2.16)$$

thus the final expression for the signal power from an axion-to-photon conversion is:

$$P_{\text{sig}}(a\gamma \rightarrow \gamma) = \omega_{\text{res}} \frac{\kappa}{1 + \kappa} g_{a\gamma\gamma}^2 \frac{\rho_a}{m_a^2} B_0^2 V_c C_{nml} Q_L. \quad (2.17)$$

Here V_c is the cavity volume and ρ_a the DM axion energy density. The coefficient C_{nml} is the *form factor* of the TM_{nml} resonant modes of the cavity and is defined as:

$$C_{nml} = \frac{\left| \int \hat{\mathbf{z}} \cdot \mathbf{e}_{nml}^*(\mathbf{x}) d^3x \right|^2}{V_c \int \epsilon |\mathbf{e}_{nml}(\mathbf{x})|^2 d^3x}. \quad (2.18)$$

A resonant mode is a particular field configuration in the cavity, see Sec. 2.3 for their description. The subscripts n, m, l are integer numbers that characterize each field configuration, and $\mathbf{e}_{nml}(\mathbf{x})$ is the spatial dependence of the electric field of the cavity mode. ϵ is the electric permittivity. The form factor C_{nml} indicates what resonant mode can be excited by the axion in an empty cavity. Since $\mathbf{e}_{nml}(\mathbf{x})$ is projected in the $\hat{\mathbf{z}}$ direction, only TM_{nml} modes can be excited, because they present a non-zero component of the electric field along $\hat{\mathbf{z}}$ (see Sec. 2.3). Actually, only TM_{0m0} modes can be excited by the axions, because electric field configurations for $n > 0$ and $l \neq 0$ give contributions that cancel out in the integral. Moreover $C_{nml} < 1$ and falls off rapidly with increasing mode number. Physically, this factor provides a quantitative feeling of the overlap between the electric field of the excited cavity mode and the external field B_0 .

All these quantities are obtained making some assumptions: a) the dimensions of the cavity are much smaller than the coherence length (1.67) of the axion field, so that it can be considered homogeneous over the whole cavity; b) the external magnetic field is directed along the $\hat{\mathbf{z}}$ direction, $\mathbf{B}_0 = B_0 \hat{\mathbf{z}}$; c) it is assumed that $Q_L < Q_a$, where Q_a is the axion figure of merit (1.66), but if this hypothesis doesn't hold Q_L must be substituted with $\min(Q_L, Q_a)$ in the expressions of the energy U and the power P_{sig} .

It is worth noticing the dependence of P_{sig} (2.17) on the model-dependent parameters and experimental quantities. The coupling $g_{a\gamma\gamma}$ appears with a squared power, and this is very limiting to the power magnitude of the signal. ρ_a and Q_a actually depend on the nature of the galactic halo and are fixed by observations. The dependence on the mass is only $\sim 1/m_a$, in fact the resonant frequency has to be tuned to the axion mass, so that $\omega_{\text{res}} \simeq m_a$, removing a power of m_a from the denominator of eq. (2.17). The volume V_c is strictly related to the mass range that one chooses to investigate, since the resonant frequency of the cavity is determined by its dimensions. The two parameters that can be increased to achieve higher powers are the magnitude of the magnetic field B_0 and the cavity quality factor Q_L (along with the coupling coefficient κ). For this reason the quantity $Q_0 B_0^2$ has been studied for one of the cavities taken into account, and the result is reported in Sec. 3.2.2. In any case, there would be no advantage having a quality factor $\gtrsim 10^6$, because in that case Q_a would dominate the signal power.

To conclude this section I quote here the signal power of the ADMX experiment [38], for comparison with the power emitted by a magnetic sample (2.13). Taking into account

again the constants \hbar and c , this is:

$$P_{\text{ADMX}} = 0.345 \cdot 10^{-21} \left(\frac{V}{500 \text{ L}} \right) \left(\frac{B_0}{7 \text{ T}} \right)^2 \left(\frac{K_{a\gamma\gamma}}{0.36} \right)^2 \times \left(\frac{\rho_a}{1/2 \cdot 10^{-24} \text{ g/cm}^3} \right) \left(\frac{m_a}{2\pi \text{ (GHz)}} \right) \left(\frac{\min(Q_L, Q_a)}{10^5} \right) \text{ W}, \quad (2.19)$$

where the TM₀₁₀ mode ($C_{nml} = 0.69$) has been considered and $K_{a\gamma\gamma}$ is given in eq. (1.52). This expression of the power shows that also in this case it is a very small quantity, so an appropriate choice of the photon receiver is necessary.

Thus far, talking about haloscopes and in general axion detectors, I mentioned the use of magnetic fields, resonant cavities, superconductors and cryogenics. Then this chapter is dedicated to putting together all these topics to describe the current QUAX R&D activity. These are concepts of radio-frequency and superconductivity, given in Sec. 2.2, and electromagnetic properties of microwave cavities treated with a field theory approach (Sec. 2.3). The current experimental set-up at LNF is also described, see Sec. 2.5. The main purposes of the QUAX R&D and of this thesis work are summarized in Sec. 2.4.

2.2 Tools to study resonant cavities

2.2.1 Radiofrequency concepts

As described in Appendix A, a resonant cavity is made of conducting walls and can be seen as a waveguide short-circuited at both ends. Moreover, the working frequencies of QUAX are in the microwave range (order 10 GHz), so in what follows some radio-frequency concepts are introduced, primarily the scattering matrix, enabling the description of cavities from a circuit point of view. In this subsection the theory is readapted from the complete and exhaustive textbook of Ref. [44]. This is a rather technical subsection, so if the reader wants to skip it, here I summarize the highlights: eq. (2.26) is the definition of the quality factor, eq. (2.28) defines the loaded quality factor; eq.s (2.47) and (2.48) contain the definition of the coupling coefficients κ , eq. (2.49) is the relation between κ and the loaded and unloaded quality factors. Finally eq. (2.54) and eq. (2.57) are, respectively, the S_{11} and S_{21} expressions. These are the measured parameters that were fitted to extract the quality factors of the cavities, as described in Sec. 3.1.2.

Parallel RLC parameters

Here the results and parameters for a parallel RLC circuit will be briefly summarized, since the cavity under inspection will be parametrized as a parallel RLC circuit, that behaves as a resonator. Lumped-element circuit theory is assumed, and the calculations

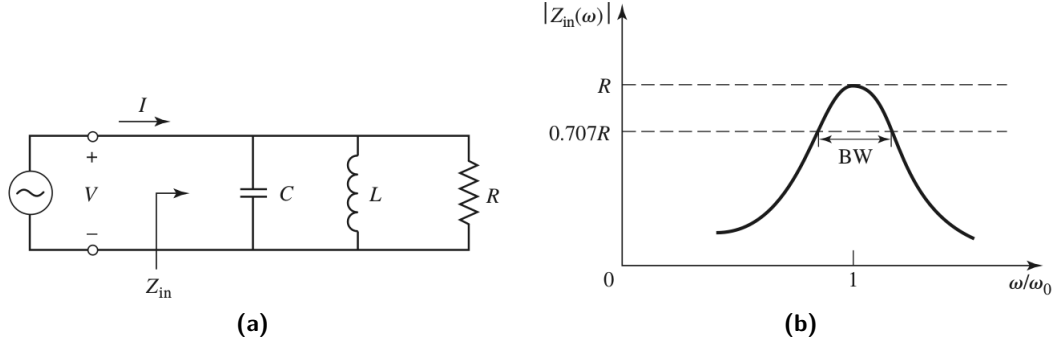


Figure 2.2: (a): a parallel RLC circuit without losses. (b): the frequency dependence of the input impedance $|Z_{in}|$ of a parallel RLC circuit; the value of $|Z_{in}|$ corresponding to half power delivered to the circuit is also reported. Taken from [44].

are made in phasor notation.

One can start writing the input impedance of a parallel RLC circuit, shown in Fig. 2.2a, that is:

$$Z_{in} = \left(\frac{1}{R} + \frac{1}{j\omega L} + j\omega C \right)^{-1}. \quad (2.20)$$

In circuit theory, using the phasor notation, the complex time-averaged power delivered to the resonator can be written as:

$$P_{in} = \frac{1}{2} Z_{in} |I|^2 = \frac{1}{2} |V|^2 \frac{1}{Z_{in}^*} = \frac{1}{2} Z_{in} \frac{|V|^2}{|Z_{in}|^2}. \quad (2.21)$$

Using the following expressions for, respectively, the real power dissipated in the circuit, the electric and magnetic energies stored in the resonator:

$$P_{loss} = \frac{1}{2} \frac{|V|^2}{R} \quad W_e = \frac{1}{4} |V|^2 C \quad W_m = \frac{1}{4} |V|^2 \frac{1}{\omega^2 L}, \quad (2.22)$$

equation (2.21) becomes:

$$P_{in} = P_{loss} + 2j\omega(W_m - W_e), \quad (2.23)$$

and then the impedance:

$$Z_{in} = \frac{2P_{in}}{|I|^2} = \frac{P_{loss} + 2j\omega(W_m - W_e)}{\frac{1}{2}|I|^2}. \quad (2.24)$$

The phenomenon of resonance occurs when the electric and magnetic stored energies are equal, $W_m = W_e$, and correspondingly the impedance, $Z_{in} = R$, reaches its maximum for the parallel RLC (Fig. 2.2b). The *resonant frequency*³ is found by equating the expressions

³It is customary to call the pulsation and the frequency with the same name, but they still hold their own identity.

for W_e and W_m , and is:

$$\omega_0 = \frac{1}{\sqrt{LC}}. \quad (2.25)$$

The *quality factor* is defined as the ratio of the energy stored in the cavity and the power dissipated by it:

$$Q = \omega \frac{W_m + W_e}{\text{en./sec}}, \quad (2.26)$$

and for the parallel *RLC* circuit, evaluating it at resonance, it is:

$$Q = \omega_0 \frac{2W_m}{P_{\text{loss}}} = \omega_0 RC = \frac{R}{\omega_0 L}. \quad (2.27)$$

The Q of a resonator quantifies its losses, that can be conductor, dielectric or radiation losses and are represented by R . It also quantifies the width of the resonance curve of a resonator in its power spectrum. Expressions in (2.26) and (2.27) are referred to as *unloaded* quality factor, Q_0 , representing the intrinsic Q factor of a resonator, evaluated when it is isolated. However, in order to feed and measure the response of a resonator, one needs to couple it to other circuit elements. This effectively lowers the quality factor, because external elements introduce additional losses. The new system is characterized then by a *loaded* quality factor, Q_L , that is a combination of the unloaded and external quality factors. Since powers are additive quantities, so are the inverse of the quality factors, and the loaded Q can be expressed as:

$$\frac{1}{Q_L} = \frac{1}{Q_0} + \frac{1}{Q_{\text{ext}}}. \quad (2.28)$$

With the definition of the unloaded quality factor and resonant frequency, the input impedance of eq. (2.20) can be rewritten in the following way:

$$Z_{\text{in}} = \frac{j\omega RL}{R - \omega^2 RLC + j\omega L} = \frac{R}{1 + jQ_0\delta}, \quad (2.29)$$

where δ is defined by:

$$\delta = \frac{\omega}{\omega_0} - \frac{\omega_0}{\omega}. \quad (2.30)$$

Equation (2.27) is valid for the unloaded quality factor of an ideal parallel *RLC* circuit. In real applications resonators are more complicated objects, like cavities in the case of this work. The theoretical unloaded quality factor of a cavity of any shape is then calculated considering it as a conductor with losses, so $Q_c = 2\omega_0 W_e / P_c$. P_c is the real power dissipated on the wall surfaces of the conductor. Ultimately, in vacuum, the quality

factor becomes in this case [44]:

$$Q_0 \equiv Q_c = \frac{G}{R_s}, \quad (2.31)$$

where G is a factor depending only on the geometry of the conductor and the properties of the material that may fill it (μ, ϵ), while R_s is the *surface resistivity*, defined as:

$$R_s = \sqrt{\frac{\omega\mu\rho}{2}} \equiv \frac{\rho}{\delta_s}, \quad (2.32)$$

where here ρ is the electric (bulk) resistivity and δ_s the skin depth. The surface resistivity is frequency-dependent, and is the resistivity encountered by a current flowing only on the surface of a conductor.

Scattering Matrix

Networks in radio-frequency regime cannot be treated with lumped-element circuit theory, since the wavelengths of electromagnetic signals are comparable in size with circuit elements themselves, causing a given branch to have not unique voltage and current values at every point. Therefore, a distributed-element theory has to be adopted. Here all electrical and magnetic quantities are expressed in phasor form and are complex quantities. The time dependence can be added simply multiplying by $e^{j\omega t}$.

The complete characterization of a generic N-port network would require the solution of Maxwell's equations, giving the expression of the fields at any point. However, usually one only needs voltage, current, power flow at some port, so only terminal quantities are of interest. Techniques based on concepts of circuit theory are then developed, leading to different ways to characterize a network. In the following I adopt the formalism said of the *scattering matrix*.

Taking into account an arbitrary lossless waveguide, equivalent voltages and currents can be defined, according to the discussion in Section 4.1 of [44]. Considering z as the direction of propagation, they are:

$$V(z) = V_0^+ e^{-j\beta z} + V_0^- e^{j\beta z}, \quad (2.33a)$$

$$I(z) = I_0^+ e^{-j\beta z} - I_0^- e^{j\beta z}, \quad (2.33b)$$

where V_0^\pm and I_0^\pm are arbitrary complex amplitudes of the incident and reflected waves respectively, $\beta = \frac{2\pi}{\lambda}$ is the propagation constant (or wave number) and the characteristic impedance Z_0 of the line is defined as:

$$\frac{V_0^+}{I_0^+} = \frac{V_0^-}{I_0^-} \equiv Z_0. \quad (2.34)$$

In Figure 2.3 a generic N-port network is shown, where any kind of transmission line

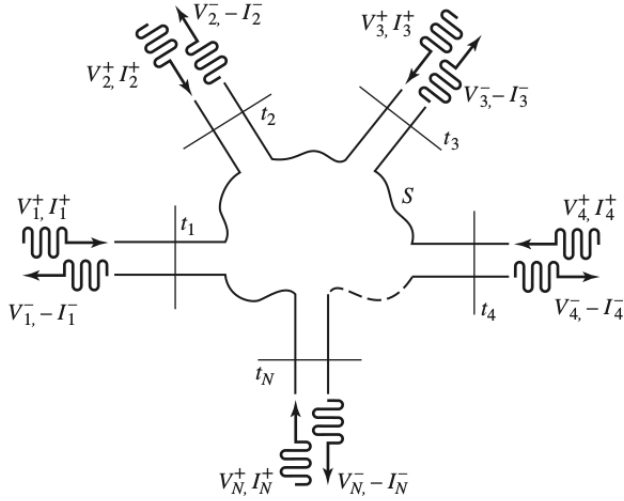


Figure 2.3: Generic N-port network. Forward waves (entering the network) are labeled with their voltages and currents, V_i^+, I_i^+ , while backward waves (outgoing from the network) are labeled with V_i^-, I_i^- . The t_n are phase reference planes. Source: [44].

or waveguide can converge in a port. In the picture t_n indicates a phase reference plane, meaning that the coordinate of the direction of propagation of the n-th line is zero at that plane: $z_n = 0$. Thus V_n^+ is the voltage amplitude of an incident wave in the n-th port entering the network, V_n^- the amplitude of the outgoing wave, and the same applies to I_n^\pm . At the plane t_n the total voltage and currents are then:

$$V_n(z_n = 0) = V_n^+ + V_n^-, \quad (2.35a)$$

$$I_n(z_n = 0) = I_n^+ - I_n^-. \quad (2.35b)$$

The *scattering matrix* relates the amplitudes of the incident waves with the ones of the reflected waves from the ports. The basic idea is that the voltage outgoing from the n-th port is due to a fraction of the incident wave into the same port and a fraction of the incident waves entering the network from all the other ports: $V_n^- = S_{nn}V_n^+ + S_{n1}V_1^+ + S_{n2}V_2^+ + \dots$. The voltage values are referred to the $\{t_1, t_2, \dots, t_N\}$ phase reference planes. In matrix form:

$$\begin{bmatrix} V^- \end{bmatrix} = [S] \begin{bmatrix} V^+ \end{bmatrix}, \quad (2.36a)$$

$$\begin{bmatrix} V_1^- \\ V_2^- \\ \vdots \\ V_N^- \end{bmatrix} = \begin{bmatrix} S_{11} & S_{12} & \dots & S_{1N} \\ S_{21} & S_{22} & \dots & S_{2N} \\ \vdots & \vdots & \ddots & \vdots \\ S_{N1} & S_{N2} & \dots & S_{NN} \end{bmatrix} \begin{bmatrix} V_1^+ \\ V_2^+ \\ \vdots \\ V_N^+ \end{bmatrix}. \quad (2.36b)$$

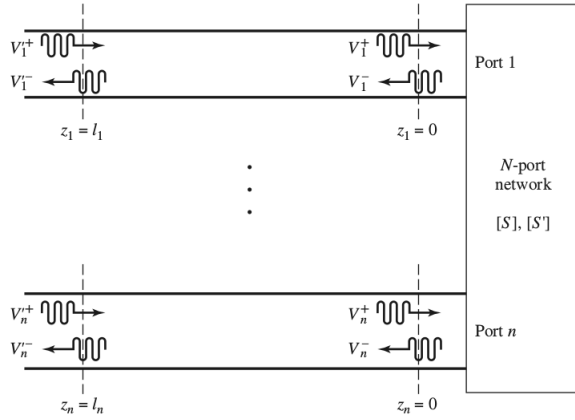


Figure 2.4: Sketch of the shifted t'_n planes. Source: [44].

An element of the scattering matrix S_{ij} is defined as

$$S_{ij} = \left. \frac{V_i^-}{V_j^+} \right|_{V_k^+ = 0, k \neq j}, \quad (2.37)$$

and can be determined by driving port j with an amplitude V_j^+ and measuring an amplitude V_i^- at port i , when all other k ports are matched⁴, so there are neither incoming V_k^+ nor reflected V_k^- waves from that ports. Therefore elements S_{ii} can be obtained as reflection coefficients at port i , with the constraint that all other ports are matched, and elements S_{ij} can be calculated as transmission coefficients from port j to port i with the constraint that all other ports are matched.

A useful concept that will be used later is that of the change of the reference planes t_n , where voltages and currents are defined or measured. Referring to Fig. 2.4, in positions $z_1, \dots, z_n = 0$ the values of V_n and I_n are defined as in eq. (2.35), and call the scattering matrix of the network $[S]$ in this case. If, now, one moves the terminal planes at $z_1 = l_1, \dots, z_n = l_n$ along the line, the scattering matrix will become $[S']$. Propagating from t_n to t'_n the waves acquire a phase factor, so the voltages become:

$$V'_n^+(z_n = l_n) = V_n^+ e^{j\beta_n l_n}, \quad (2.38a)$$

$$V'_n^-(z_n = l_n) = V_n^- e^{-j\beta_n l_n}, \quad (2.38b)$$

⁴A transmission line is said to be matched when ended with a load impedance equal to its characteristic impedance, so that the reflection coefficient is zero.

or in matrix form:

$$[V'^{\pm}] = [V^{\pm}] \begin{bmatrix} e^{\pm j\beta_1 l_1} & & 0 \\ & e^{\pm j\beta_2 l_2} & \\ & & \ddots \\ 0 & & e^{\pm j\beta_N l_N} \end{bmatrix}. \quad (2.39)$$

The scattering matrices are defined in the two configurations as:

$$[V^-] = [S][V^+], \quad (2.40a)$$

$$[V'^-] = [S'][V'^+], \quad (2.40b)$$

thus substituting eq. (2.39) in eq. (2.40a) the following result can be obtained, with some algebra:

$$[V'^-] = [e^{-j\beta_n l_n}][S][e^{-j\beta_n l_n}][V'^+], \quad (2.41)$$

where the new $[S']$ matrix can be recognized:

$$[S'] = \begin{bmatrix} e^{-j\beta_1 l_1} & 0 \\ & e^{-j\beta_2 l_2} \\ & & \ddots \\ 0 & & e^{-j\beta_N l_N} \end{bmatrix} [S] \begin{bmatrix} e^{-j\beta_1 l_1} & 0 \\ & e^{-j\beta_2 l_2} \\ & & \ddots \\ 0 & & e^{-j\beta_N l_N} \end{bmatrix}. \quad (2.42)$$

Scattering matrix of a resonant cavity

In our set-up we have a resonant RF cavity connected to a VNA⁵ (see Sec. 2.5) that provides and measures the power delivered to and from the cavity. Two antennas are coupled with the cavity, so our device is a 2-port network, and has a scattering matrix of the form:

$$[S] = \begin{bmatrix} S_{11} & S_{12} \\ S_{21} & S_{22} \end{bmatrix}, \quad (2.43)$$

with $S_{12} = S_{21}$ because the device is reciprocal, meaning that it does not contain anisotropic or active materials that could give a different response if inspected from different directions. The calculation of all the scattering parameters follows.

To construct a simple model that makes use of circuit laws, assumptions and parameterizations are necessary; therefore the cavity will be parametrized as a parallel RLC circuit, because the walls are short-circuited for construction. Here the resistance R accounts for conductor losses due to the metallic walls, the inductance L and the capacity C are dynamic quantities that account for the energy stored in the cavity. The coupling of the antennas can be schematized as two ideal transformers. Fig. 2.5a shows the parametrized

⁵Agilent E5071C, frequency range: 300 kHz – 20 GHz.

circuit; this is the particular case in which the device is excited from port 1, where an ideal generator has been placed, and the impedances Z_0 account for lossless transmission lines feeding the cavity. To calculate the scattering parameters the circuit can be further simplified. Hereafter this is done from the generator point of view. For a generic ideal transformer of primary N_1 windings and secondary N_2 windings, the following relations between voltages and currents of its primary and secondary circuits are valid:

$$\frac{v_1}{v_2} = \frac{N_1}{N_2}, \quad \frac{i_1}{i_2} = -\frac{N_2}{N_1}. \quad (2.44)$$

In our case, as in Fig. 2.5a, if the ratio of the windings between the cavity and the second antenna is set to $n_2 : 1$, port 2 can be thought as an impedance in parallel to the cavity. In fact, calling V_{cav} the voltage of the parallel RLC and V_2, I_2 the voltage and current at port 2, from eq. (2.44) we have:

$$V_{\text{cav}} = \frac{n_2}{1} V_2 = n_2 (-Z_0 I_2) = n_2 Z_0 I_{\text{cav}} \frac{n_2}{1} \equiv Z_2 I_{\text{cav}}, \quad (2.45)$$

with $Z_2 = n_2^2 Z_0$ the impedance seen by the cavity looking towards port 2. The equivalent circuit is displayed in Fig. 2.5b. With the same argument the impedance seen by the generator looking towards port 1 is $\frac{1}{n_1^2}$ times the parallel of Z_{cav} and Z_2 :

$$Z_1 \equiv \frac{1}{n_1^2} Z_{\text{cav}} // Z_2 = \frac{1}{n_1^2} \left(\frac{n_2^2 Z_0 \cdot \frac{R}{1+jQ_0\delta}}{n_2^2 Z_0 + \frac{R}{1+jQ_0\delta}} \right), \quad (2.46)$$

where use of eq. (2.20) for Z_{cav} has been made. The resulting equivalent circuit is shown in Fig. 2.5c.

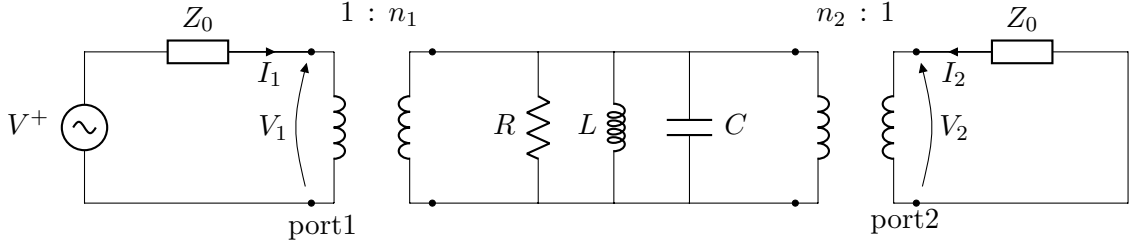
Before evaluating the impedance Z_1 it is convenient to incorporate the arbitrary constants n_1 and n_2 in observable quantities. These are the coupling coefficients κ_1 and κ_2 , that give quantitatively the fraction of energy communicated to the cavity, and are defined as the ratio of the power dissipated in the external circuitry and the power dissipated inside the cavity:

$$\kappa_1 \equiv \frac{P_1}{P_{\text{cav}}}, \quad \kappa_2 \equiv \frac{P_2}{P_{\text{cav}}}. \quad (2.47)$$

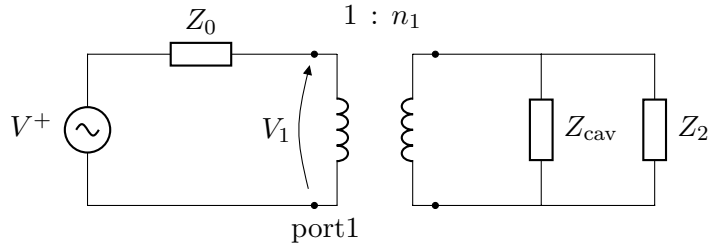
(Note that, in general, if one defines an external quality factor with the power dissipated by external circuitry $Q_{\text{ext}} = \omega_0 U_{\text{cav}} / P_{\text{ext}}$, whit U_{cav} the energy stored in the cavity, the definition of eq. (2.47) for a coupling κ is equivalent to:

$$\kappa \equiv \frac{Q_0}{Q_{\text{ext}}}. \quad (2.48)$$

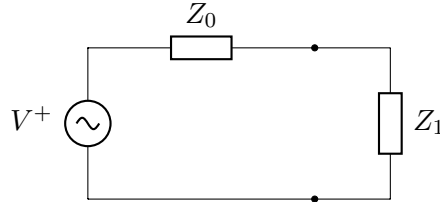
Referring to eq. (2.28) for the loaded quality factor and using the definition (2.48), the



(a) Equivalent circuit of the cavity, assumed as a parallel RLC , and the exitation of the antennas, schematized as transformers.



(b) Equivalent circuit with second port seen as an impedance Z_2 .



(c) Equivalent circuit as seen by the generator.

Figure 2.5: Equivalent circuits of the system formed by resonant cavity and antennas.

former becomes now:

$$Q_L = \frac{Q_0}{1 + \kappa}. \quad (2.49)$$

This will be useful in the subsequent sections.

Returning to the couplings κ_1 and κ_2 , Fig. 2.6 helps to evaluate them. The picture shows the equivalent circuit as seen from the cavity. From this point of view Z'_1 and Z'_2 , the impedances seen by the cavity towards port 1 and port 2 respectively, are:

$$\begin{aligned} Z'_1 &= n_1^2 Z_0 \\ Z'_2 &= n_2^2 Z_0, \end{aligned} \quad (2.50)$$

and since they are both in parallel with Z_{cav} , the voltage at their edges is equal to V_{cav} . P_1 and P_2 of eq. (2.47) are the powers dissipated on the impedances Z'_1 and Z'_2 , while the power dissipated by the cavity is real and only due to the resistance R (that is the real part of Z_{cav}). From circuit theories, time averaged powers can be calculated as

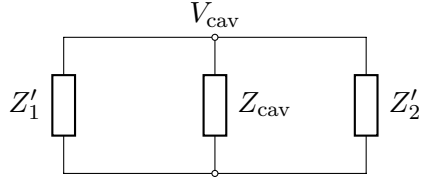


Figure 2.6: Equivalent circuit as seen from the cavity, for the evaluation of κ_1 and κ_2 .

$P = \frac{1}{2}Z|I|^2 = \frac{1}{2}\frac{|V|^2}{Z^*}$, thus for our equivalent circuit they are:

$$P_1 = \frac{1}{2}\frac{|V_{\text{cav}}|^2}{n_1^2 Z_0}, \quad P_2 = \frac{1}{2}\frac{|V_{\text{cav}}|^2}{n_2^2 Z_0}, \quad P_{\text{cav}} = \frac{1}{2}\frac{|V_{\text{cav}}|^2}{R}. \quad (2.51)$$

Therefore, the coupling coefficients are:

$$\kappa_1 = \frac{P_1}{P_{\text{cav}}} = \frac{R}{n_1^2 Z_0}, \quad \kappa_2 = \frac{P_2}{P_{\text{cav}}} = \frac{R}{n_2^2 Z_0}. \quad (2.52)$$

Equation (2.46) is thus rewritten as:

$$Z_1 = \frac{Z_{\text{cav}}/n_2^2 Z_0}{n_1^2} = Z_0 \kappa_1 \left(\frac{\frac{1}{\kappa_2} \cdot \frac{1}{1+jQ_0\delta}}{\frac{1}{\kappa_2} + \frac{1}{1+jQ_0\delta}} \right) = \frac{Z_0 \kappa_1}{1 + \kappa_2 + jQ_0\delta}. \quad (2.53)$$

The S_{11} parameter can now be obtained. The contributions to the voltage at port 1, V_1 , come from an incident wave V_1^+ and a reflected wave V_1^- , so $V_1 = V_1^+ + V_1^-$, and the coordinate z_1 is set to zero at port 1. From its definition, S_{11} is the reflection coefficient Γ at port 1, if one considers Z_0 as a lossless transmission line terminated on a load Z_1 (see Fig. 2.5c).

$$S_{11} = \frac{V_1^-}{V_1^+} \Big|_{V_2^+=0} = \Gamma(z_1=0) = \frac{Z_1 - Z_0}{Z_1 + Z_0} = \frac{\frac{Z_0 \kappa_1}{1 + \kappa_2 + jQ_0\delta} - Z_0}{\frac{Z_0 \kappa_1}{1 + \kappa_2 + jQ_0\delta} + Z_0} = \frac{\kappa_1 - (1 + \kappa_2 + jQ_0\delta)}{\kappa_1 + 1 + \kappa_2 + jQ_0\delta}. \quad (2.54)$$

Note that Z_0 appearing in Z_1 is the impedance of the second transmission line, while Z_0 present in the definition of $\Gamma(z_1=0)$ is the impedance of the first transmission line. In general they can be different, but here they are assumed equal and this is a reasonable assumption, since the two coaxial cables that feed the cavity are equal in length, material and geometry.

It is now straightforward to compute S_{21} . It is defined as

$$S_{21} = \frac{V_2^-}{V_1^+} \Big|_{V_2^+=0},$$

so, again, port 2 must be adapted to have $V_2^+ = 0$. Then the total voltage V_2 reduces to $V_2 = V_2^-$, setting the coordinate $z_2 = 0$ at port 2. V_2 is derived from transformer laws, seeing the circuit of Fig. 2.5a from port 2 towards the generator. The relation between the cavity voltage and the voltage at port 1 is $V_{\text{cav}} = n_1 V_1$, and the relation between the voltage at port 2 and V_{cav} is $V_2 = \frac{V_{\text{cav}}}{n_2}$, and putting them together:

$$V_2 = \frac{V_{\text{cav}}}{n_2} = \frac{n_1}{n_2} V_1. \quad (2.55)$$

As before, $V_1 = V_1^+ + V_1^- = V_1^+(1 + \Gamma)$, where $\Gamma = \frac{V_1^-}{V_1^+} = S_{11}$, because we know that $V_2^+ = 0$; therefore V_2 is now determined:

$$V_2 = V_2^- = \frac{n_1}{n_2} V_1^+(1 + \Gamma). \quad (2.56)$$

Equation (2.56) then gives the parameter S_{21} :

$$\begin{aligned} S_{21} &= \left. \frac{V_2^-}{V_1^+} \right|_{V_2^+ = 0} = \frac{n_1}{n_2} (1 + \Gamma) = \frac{n_1}{n_2} (1 + S_{11}) = \\ &= \sqrt{\frac{\kappa_2}{\kappa_1}} \left[1 + \frac{\kappa_1 - (1 + \kappa_2 + jQ_0\delta)}{\kappa_1 + (1 + \kappa_2 + jQ_0\delta)} \right] = \frac{2\sqrt{\kappa_1\kappa_2}}{1 + \kappa_1 + \kappa_2 + jQ_0\delta}. \end{aligned} \quad (2.57)$$

Thanks to the symmetry of the configuration, S_{22} is easily found by swapping the roles of κ_1 and κ_2 in the expression of S_{11} :

$$S_{22} = \frac{\kappa_2 - (1 + \kappa_1 + jQ_0\delta)}{1 + \kappa_1 + \kappa_2 + jQ_0\delta}. \quad (2.58)$$

Finally, as discussed before $S_{12} = S_{21}$, being our device a reciprocal network.

These are ideal values obtained from assumptions and simplifications. In the experimental set-up (see Sec. 2.5) the power feeding the cavity is provided by the VNA. This power is first delivered by two cables to the antennas, and then they feed the cavity. The procedure of calibration for the two cables has been executed, so that the Analyzer measures voltages and currents at the beginning of the two antennas, and these positions are now the actual port 1 and 2. A shift of the reference planes has to be performed. Referring to Fig. 2.4 and equation (2.42) and assuming the antennas to be equal in length and composition, so that $l_1 = l_2 \equiv l$ and $\beta_1 = \beta_2 \equiv \beta$, the new $[S']$ scattering matrix can be computed as:

$$\begin{aligned} [S'] &= \begin{bmatrix} e^{-j\beta l} & 0 \\ 0 & e^{-j\beta l} \end{bmatrix} \begin{bmatrix} S_{11} & S_{12} \\ S_{21} & S_{22} \end{bmatrix} \begin{bmatrix} e^{-j\beta l} & 0 \\ 0 & e^{-j\beta l} \end{bmatrix} = \\ &= \begin{bmatrix} e^{-2j\beta l} & 0 \\ 0 & e^{-2j\beta l} \end{bmatrix} \begin{bmatrix} S_{11} & S_{12} \\ S_{21} & S_{22} \end{bmatrix}. \end{aligned} \quad (2.59)$$

The new elements are:

$$\begin{aligned} S'_{11} &= e^{-2j\beta l} S_{11} \\ S'_{12} &= S'_{21} = e^{-2j\beta l} S_{12}. \end{aligned} \quad (2.60)$$

The shift consists in the acquisition of a phase factor, then it only affects the real and imaginary parts of the scattering parameters, while the modulus remains unchanged. The modulus of the S_{11} and S_{21} scattering parameters are plotted in Fig. 3.1. $|S_{11}|$ has a minimum at the resonant frequency, because energy is stored inside the cavity and, ideally, no power is reflected back by port 1. For the same reason $|S_{21}|$ has a maximum at the resonant frequency.

2.2.2 Elements of superconductivity

Here I give an introduction to the concepts of superconductivity, giving a rather qualitative description and introducing only the fundamental equations useful to our goals. A particular attention is given to the behaviour of superconductors in applied magnetic fields, since in both the QUAX operation modes external static magnetic fields are present (Sec. 2.1).

Superconductivity was first introduced by K. Onnes in 1911 as a new state of matter, while studying the resistivity of metals at low temperatures. He saw that below 4 K pure mercury presents zero electrical resistance. This observations allow to introduce two features of superconductivity: phenomenologically superconductors present zero electric resistance, or perfect conductivity; the onset of superconductivity occurs at a *critical temperature* T_c , below which the material enters the superconducting phase. A consequence of the perfect conductivity is that superconductors can hold electric currents without any loss for a ideally infinite time. A characteristic that distinguishes superconductors from perfect conductors is the **Meissner effect**. Suppose to cool a superconductor and a perfect conductor with a null external magnetic field $\mathbf{B} = \mathbf{0}$, and then turn the magnetic field on when the temperature has reached $T < T_c$. This process is called Zero-Field Cooling (ZFC) and is depicted in Fig 2.7. Both the materials *exclude* the magnetic field lines from their interior ($\mathbf{B} = \mathbf{0}$), behaving as perfect diamagnets with magnetization $\mathbf{M} = -4\pi/\mathbf{H}$.⁶ On the contrary, if the two materials are cooled while a magnetic field $\mathbf{B} \neq \mathbf{0}$ is applied (Field Cooling (FC) process), when the temperature reaches $T < T_c$ the perfect conductor admits field lines in its interior, while the superconductor *expels* the magnetic field. This is the Meissner effect, and the superconductor can be considered always as a perfect diamagnet.

⁶Properly \mathbf{B} is an external magnetic field, while $\mathbf{H} = \mathbf{B} - 4\pi\mathbf{M}$ is the magnetic field in the medium.

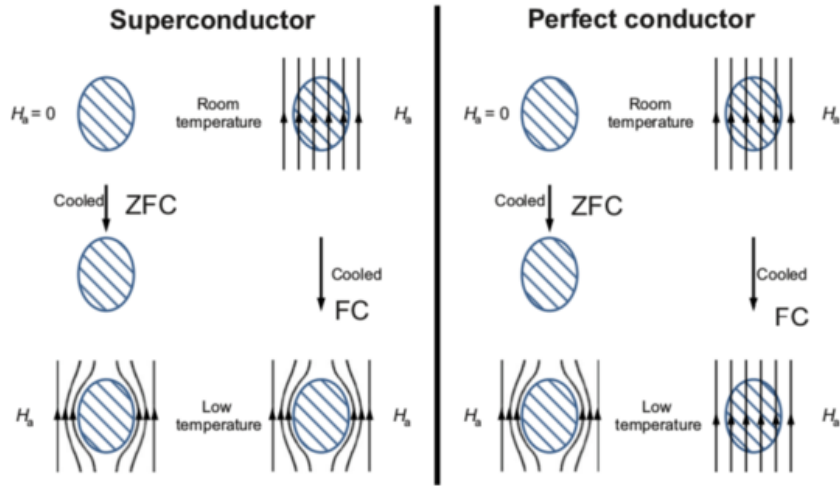


Figure 2.7: A schematic view of the Zero-Filled Cooling and Field-Cooling processes for both a superconductor and a perfect normal conductor. Here the applied magnetic field is called H_a , while in the text it is referred to as B . Adapted from [45].

London equations. London equations describe in an easy way the electrodynamic behaviour of superconductors, and allow to explain the Meissner effect. They are [46]:

$$\mathbf{E} = \Lambda \frac{\partial \mathbf{J}_s}{\partial t}, \quad (2.61a)$$

$$\mathbf{B} = -c\Lambda \nabla \wedge \mathbf{J}_s, \quad (2.61b)$$

and

$$\Lambda = \frac{4\pi\lambda^2}{c^2} = \frac{m_e}{n_{sc}e^2}. \quad (2.62)$$

\mathbf{E} and \mathbf{B} represent the external electric and magnetic fields, while \mathbf{J}_s the supercurrent flowing in the superconductor in the presence of these fields. n_{sc} is the number density of superconducting electrons, Λ is a phenomenological parameter, and λ is known as the *London depth* or *penetration depth*, for reasons that will be clear soon. Combining now the Maxwell's equations with the superconducting current \mathbf{J}_s and the London equations (2.61), we find for the electrical and magnetic fields:

$$\nabla^2 \mathbf{E} = \frac{\mathbf{E}}{\lambda^2}, \quad \nabla^2 \mathbf{B} = \frac{\mathbf{B}}{\lambda^2}. \quad (2.63)$$

The solution of these equations is a decaying exponential; as an example the x component of a magnetic field from the exterior of the superconductor surface to the interior is $B(x) = B(0)e^{-x/\lambda}$, where $B(0)$ is the field value at the surface. This shows that the superconductor is screened from external magnetic fields, and this explains the Meissner effect described before for static magnetic fields. The only region where B is allowed is within a size $\sim \lambda$ from the surface (typically ~ 50 nm), where B decays exponentially; thus the name

penetration depth. The penetration depth has a temperature dependence, that empirically is [46]:

$$\lambda(T) \approx \lambda(0) \left[1 - \left(\frac{T}{T_c} \right)^4 \right]^{-1/2}.$$

Critical fields and currents. Superconductors can't screen magnetic fields of any magnitude, there exists a limit value called *thermodynamic critical field* B_c . If magnetic fields $B > B_c$ are applied, the superconductor transits to the normal state. This is due to minimum energy arguments, i.e. the critical field is related to the difference of the Gibbs free energies of the normal and superconducting state, and when $B > B_c$ the free energy is minimized by the normal state. Corresponding to the critical field is the concept of the *critical current density* J_c , the maximum value of a current that does not spoil superconductivity. It can be understood by thinking of an applied supercurrent flowing in a superconductor. This will generate an induced magnetic field; if the current density is such that B_{ind} reaches B_c , this will cause the transition.

The dependence of the critical field on temperature is [46]:

$$B_c(T) \approx B_c(0) \left[1 - \left(\frac{T}{T_c} \right)^2 \right].$$

The thermodynamic critical field and the critical temperature are intrinsic properties of the material, and are thermodynamically connected: not only B_c varies with the temperature, but also T_c decreases if a magnetic field is applied to the superconductor.

BCS theory. A microscopic explanation of the phenomenon of superconductivity is given by the BCS theory (after Bardeen, Cooper and Schrieffer, 1957) [46]. Here an attractive force between pairs of electrons is supposed, due to an electron-lattice interaction. Qualitatively speaking, an electron interacts with the lattice and deforms it; this modifies the potential generated by the positive ion of the lattice, and a second electron sees this deformation as an attractive force. The binding of such two electrons is called a Cooper pair. The Cooper pairs behave like bosons, with the consequence that the ground state of a superconductor is lowered with respect to the Fermi energy level of a normal material. An energy gap across the Fermi level is created, that divides the state occupied by the Cooper pair from an excited state. This energy gap, at temperature $T = 0$, is equal to $2\Delta(0) = 3.52 k_B T_c$, with k_B the Boltzmann constant. Its temperature dependence is:

$$\Delta(T) \approx 1.76 \Delta(0) \left(1 - \frac{T}{T_c} \right)^{1/2}.$$

The superconducting state can exist if the Cooper pairs form and overlap their wavefunctions. Cooper pairs can form if the distance between electrons in the interaction is such that the second electron is affected by the lattice deformation generated by the passage of the first. A *coherence length* ξ is then introduced, that is the size within which Cooper pairs can form. From an uncertainty principle argument it is estimated to be [46]:

$$\xi \simeq a \frac{\hbar v_F}{k_B T_c}, \quad (2.64)$$

where v_F is the Fermi velocity and a is a parameter of $\mathcal{O}(1)$ to be determined experimentally for each material.

Ginzburg-Landau theory The Ginzburg-Landau (GL) theory [46] was actually proposed in 1950, before the BCS theory. It was the first phenomenological theory describing superconductivity with a quantum mechanical approach. They assumed that a material is composed by a normal density of electrons and a superconducting one. The superconducting electrons are described by an order parameter ψ , that is a pseudo-wavefunction and is related to the density of superconducting electrons as $n_{sc} = |\psi(x)|^2$. More physically, ψ can be thought of as the wavefunction of the center-of-mass motion of the Cooper pairs, that have mass and charge twice that of electrons. The theory introduced a GL coherence length ξ , that is the distance over which ψ can vary without increasing the free energy. Later, Abrikosov showed that the ratio between the London penetration depth λ and the coherence length ξ defines the distinction between type-I and type-II superconductors (see the next paragraph for their description). If $\lambda/\xi < 1/\sqrt{2}$ the superconductor is type-I, if $\lambda/\xi > 1/\sqrt{2}$ is type-II. From the GL theory the London equations naturally follow.

As just mentioned, there exist two types of superconductors, referred to as type-I and type-II, that present some differences. Since now, only the type-I superconductors were described.

Type-II superconductors. These were introduced by Abrikosov in 1957, because they presented discrepancies with the theories developed for type-I superconductors. The first important difference is the behaviour in the presence of an applied magnetic field. The response of type-II superconductors to magnetic fields can be divided in three regimes, separated by two critical field values, B_{c1} and B_{c2} . From 0 to B_{c1} the behaviour is equal to that of a type-I superconductor, except that B_{c1} is not the thermodynamic critical field that drive their transition. The superconductor shows perfect diamagnetism (Meissner effect), with external magnetic fields totally excluded or expelled. Above B_{c2} the superconductor undergoes the transition to the normal state. Instead, from B_{c1} to B_{c2} the superconductor enters a *mixed state* characterized by an imperfect Meissner effect, because

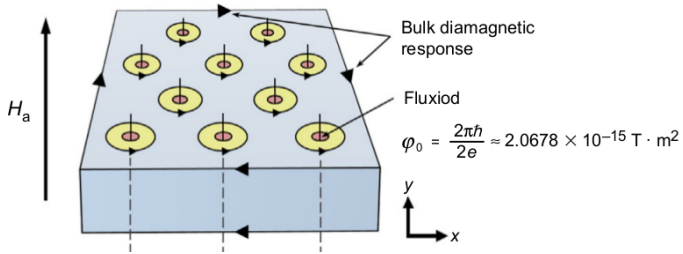


Figure 2.8: Sketch of a section of type-II superconductor with an applied field (here named H_a and along the y direction) in the range $H_{c1} < H_a < H_{c2}$. Fluxons penetrate in the normal cores, in red, having a size $\sim \xi$, while the yellow area marks the region of extension of the magnetic field, of size $\sim \lambda$. Taken from [45].

some magnetic lines are allowed to penetrate in the bulk. These *flux lines* penetrate in cylinder-shaped regions, with the internal core in the normal state. These structures, schematically shown in Fig. 2.8, are often called *vortices*, because the magnetic field lines generate currents flowing in loops at the surface of the cylinders. It is found that the magnetic field lines can enter the superconductor only in flux quanta, called *fluxons* or *fluxoids*, having a value of [46, 45]:

$$\Phi_0 = \frac{hc}{2e} \simeq 2.0678 \cdot 10^{-15} \text{ T m}^2. \quad (2.65)$$

The extension of the normal core region is of order the coherence length ξ , while the magnetic field that penetrates in these structures has an exponential decay from the center to the walls of the cylinders, and extends for a size of order the penetration depth λ . Since in type-II superconductors $\lambda > \xi$, it follows that they undergo mutual repulsive electromagnetic interactions, because the current around a core interacts with the magnetic field coming from a neighbouring core. Each fluxon is then affected by a Lorentz force given by [46]:

$$\mathbf{f}_L = \mathbf{J}_s \wedge \frac{\Phi_0}{c}, \quad (2.66)$$

where \mathbf{J}_s is the supercurrent density locally generated by all the other fluxons. Φ_0 has magnitude Φ_0 and the same direction as the applied field. Fluxons, however, reach an equilibrium arranging in (usually) triangular arrays, called Abrikosov lattices, with a lattice length of $d \approx \sqrt{\Phi_0/B}$, where B is an applied magnetic field.

Pinning, flux flow and losses in type-II superconductors

The concepts described in this paragraph, all discussed in Ref. [46], will be important in the understanding of the dependence of the quality factor Q of the cavity on the applied magnetic field in Sec. 3.2.

Pinning and flux flow. Consider an undefected type-II superconductor in the mixed state, obtained applying a magnetic field (but the same argument works with an applied current). The drawback of such a pure material is that it easily dissipates energy, as explained in a while. The Lorentz force is responsible for the movement of the fluxons, and the Lorentz force density can be written as:

$$\mathbf{F}_L = \mathbf{J}_s \wedge \frac{\mathbf{B}}{c}, \quad (2.67)$$

This is a generalization of eq. (2.66), where the field \mathbf{B} is expressed in terms of the flux quantum: $\mathbf{B} = n\Phi_0$ (n is the number of fluxons per unit area). The supercurrent density \mathbf{J}_s now accounts for both the contribution due to neighbouring fluxons and the contribution of an external applied current. This force will induce an electric field parallel to \mathbf{J}_s :

$$\mathbf{E} = \mathbf{B} \wedge \frac{\mathbf{v}}{c}, \quad (2.68)$$

where here \mathbf{v} is the velocity of fluxons, now in motion. The presence of an electric field generates a voltage, and this leads to power dissipation. The electrons present in the normal cores moving with velocity \mathbf{v} suffer from Joule effect; the produced heat could also cause the transition of the superconductor.

This dissipation is, however, avoided if there exists some mechanism that makes the Lorentz force ineffective. This is the *pinning*, consisting in the presence of impurities, defects and/or dislocations in the material. The presence of these defects is seen as a potential well by the normal cores, that locally minimize the free energy, so if the potential is strong enough to prevent the action of the Lorentz force the fluxons remain "pinned" in their positions. However, if the applied currents or magnetic fields are strong enough, there will be a *flux creep*, that causes the hopping of the vortices from one pinning site to another. And if the pinning is weak with respect to the Lorentz force, the continuous hopping of the vortices results in a rather steady motion of the latter. This regime is known as *flux flow* and then the material presents a resistivity ρ_f even greater than the normal resistivity ρ_n . The resistivity ρ_f , responsible for the losses in a superconducting material, can be found with various models. Before discussing them in the next paragraphs, note that in both pure type-I and type-II superconductors there is no magnetic hysteresis, meaning that when the external magnetic field is turned off, the magnetization becomes null again, $\mathbf{M} = \mathbf{0}$. On the contrary, in defected type-II superconductors, where pinning is effective, flux lines remain trapped in the bulk resulting in a non-null magnetization even if the external field is turned off.

Bardeen-Stephen model. Phenomenologically the dissipation due to flux flow can be thought introducing a viscosity η of the medium, and assuming that the vortices reach a

velocity \mathbf{v}_L . The viscous force is then $-\eta \mathbf{v}_L$, and the power dissipated by a single fluxon is $-\mathbf{F}_{\text{visc.}} \cdot \mathbf{v}_L = \eta \mathbf{v}_L^2$. Combining this viscous force with eq.s (2.66) and (2.68), the expression of the resistivity ρ_f in this simple model is:

$$\rho_f = \frac{E}{J} = \frac{B\Phi_0}{\eta c^2}. \quad (2.69)$$

The problem reduces to finding the viscosity η . In the simple model of Bardeen-Stephen [46] its approximate expression is:

$$\eta \approx (\Phi_0 B_{c2}) / (\rho_n c^2), \quad (2.70)$$

and then the flux flow resistivity takes a rather intuitive form:

$$\frac{\rho_f}{\rho_n} = \frac{B}{B_{c2}}. \quad (2.71)$$

ρ_f can be greater than ρ_n because B_{c2} is a temperature-dependent parameter, and for $T \rightarrow T_c$ it becomes small, so that ρ_f increases fast. Now, taking the definition of the surface resistance $R_s = \rho/\delta_s$ (eq. (2.32)), using the expression of the flux flow resistivity it is:

$$R_s \approx \frac{\rho_n}{\lambda} \frac{B}{B_{c2}}, \quad (2.72)$$

where the penetration depth has been used in place of the skin depth. Remembering that $Q \sim 1/R_s$, we see that increasing a magnetic field applied on a superconducting RF cavity, its quality factor decreases (in this model) linearly.

Gittleman-Rosenblum model. In the Bardeen-Stephen model a regime of flux flow is assumed. Gittleman and Rosenblum [47, 48] developed a model for the motion of flux tubes subject to driving currents, assuming a particular form for the *pinning potential*. The equation of motion of fluxons can be solved with various approximations, depending on the experimental conditions that apply in the specific cases, and the resistivity ρ_f can be estimated.

They assume the following conditions: the superconductor is in a mixed state, with $B_{c1} \ll B \ll B_{c2}$; the temperature is well below T_c ; the fluxons lattice is rigid, meaning that all flux tubes move approximately rigidly together, and the interaction between fluxons is negligible; the driving current is orthogonal to the applied magnetic field. They call "pinning potential" the increase of pinning energy due to fluxons displacements, and extends on the whole flux tubes lattice. The potential is assumed to be periodic in the lattice constant d , and in one dimension it takes the form [47, 48]:

$$V(x) = A \left(1 - \cos \left(\frac{2\pi x}{d} \right) \right), \quad (2.73)$$

with A a constant. The lattice constant can be found by the relation $B = n\Phi_0$, where n is the number of fluxons per unit surface and then, in a rigid lattice, is simply $n = 1/d^2$. It follows that $d = (\Phi_0/B)^{1/2}$. When the lattice moves for the presence of a current (and then a Lorentz force), each vortex is subject to the force:

$$F_{\text{pin}} = -\frac{\partial V(x)}{\partial x} = -A \frac{2\pi}{d} \sin\left(\frac{2\pi x}{d}\right). \quad (2.74)$$

The equation of motion of a flux tube in this model can then be written as [48]:

$$m\ddot{x} + \eta\dot{x} + A \frac{2\pi}{d} \sin\left(\frac{2\pi x}{d}\right) = \frac{J\Phi_0}{c}, \quad (2.75)$$

where x represents the fluxon displacement, m is an effective mass of a flux tube, $\eta\dot{x}$ is the term accounting for dissipation and η is taken from the Bardeen-Stephen model (eq. (2.70)), the third term on the l.h.s is the *pinning force*, and on the r.h.s. there is the magnitude of the Lorentz force of eq. (2.66). If one solves this equation for \dot{x} , from equation (2.68) the induced electric field can be calculated, and then $\rho_f = E/J$ is obtained. In our case, the current density J of eq. (2.75) is a high frequency current density, J_{RF} , because we are dealing with radio-frequency signals.

The equation of motion (2.75) can be solved making approximations, some of these are reviewed in Ref.s [48, 49, 50]. For example, if the mass term and the x -dependent term are neglected, in Ref. [49] a dependence of $R_s \propto B$ is found for small fields, while for fields close to B_{c2} they find the relation $R_s \propto \sqrt{B}$. Gittleman and Rosenblum note that for frequencies higher than the *depinning frequency* the pinning force is no more effective, and the superconductor enters the flux flow regime even if it has pinning centers. This can be understood thinking of a classical oscillator: when it is driven with a frequency much higher than its characteristic constant, it will not give a response to the external stimulus. In this case the x -dependent term of eq. (2.75) (the pinning force) is neglected.

However, we have seen that R_s always depends on a power of B , and this inevitably causes losses in a superconducting material, and in particular in our case the quality factors of resonant cavities result lowered.

2.3 Resonant cavities

Microwave resonant cavities can be considered as volumes enclosed by conducting surfaces, in which electromagnetic fields can be excited. Therefore they can also be seen as a section of a waveguide, short-circuited at both ends by two conducting plates. The different electric and magnetic field configurations that can be excited in a resonant cavity are called *resonant modes*. Three types of resonant modes exist. Transverse electric modes (TE), characterized by a field configuration with null longitudinal component of the electric

field, $E_z = 0$, but $H_z \neq 0$. Transverse magnetic modes (TM) possess null longitudinal magnetic field component, $H_z = 0$, but $E_z \neq 0$. TEM modes are, indeed, characterized by only transverse field components and no longitudinal ones, $E_z = H_z = 0$. The most simple example of TEM modes are plane waves. In a cylindrical resonant cavity only TE and TM modes can be excited. In appendix A the derivation of these resonant modes in a cylindrical resonant cavity is summarized.

Resonant modes in a cavity are characterized by a *resonant frequency*. The resonant frequencies of TE and TM modes of a cylindrical cavity with radius a and length d are[44]:

$$f_{nml}^{\text{TE}} = \frac{1}{2\pi\sqrt{\mu\epsilon}} \sqrt{\left(\frac{p'_{nm}}{a}\right)^2 + \left(\frac{l\pi}{d}\right)^2}, \quad f_{nml}^{\text{TM}} = \frac{1}{2\pi\sqrt{\mu\epsilon}} \sqrt{\left(\frac{p_{nm}}{a}\right)^2 + \left(\frac{l\pi}{d}\right)^2}, \quad (2.76)$$

where μ and ϵ are, respectively, the magnetic permeability and electric permittivity of a dielectric that may fill the cavity, n m and l are integer numbers. p_{nm} are the m -th roots of the n -th Bessel functions of the first kind, $J_n(p_{nm}) = 0$, and p'_{nm} are the roots of their derivatives, $J'_n(p'_{nm}) = 0$. From eq. (2.76) we see that the resonant frequencies vary with the inverse of the geometric dimensions, and this explains the fact that smaller cavity volumes are needed to probe higher axion masses, that correspond to higher frequencies.

Note that no solutions are possible for frequencies different from the resonant frequencies, meaning that an infinite but discrete number of electromagnetic modes can exist in a resonant cavity. They are denoted by TE_{nml} and TM_{nml} . The index n represents the number of variations that the fields perform in the ϕ direction from 0 to 2π , the m index indicates the field variations along the ρ direction from 0 to a , and l represents the variations along z from 0 to d . Eq.s (A.19) and (A.21) in appendix A contain the expressions for TE_{nml} and TM_{nml} modes. These have the form of standing waves. In particular they depend on $\cos n\phi$ and $\sin n\phi$ terms, that represent independent field solutions. It follows that both the cosine-dependent and sine-dependent modes can be excited in a resonant cavity, thus yielding at the presence of degenerate modes, i.e. with the same resonant frequency.

Not all the infinite modes can be excited as standing waves in a resonant cavity. This derives from the solution of propagating modes in a waveguide: there exists a *cutoff frequency* $f_{c_{nm}}$ below which the propagation constant becomes pure imaginary and the waveguide modes are *evanescent*, meaning that the electromagnetic fields decay exponentially to zero with the distance (see eq. (A.9) and comments below). Correspondingly, in a resonant cavity only modes with $f > f_{c_{nm}}$ are excited as standing waves. The cutoff frequencies for TE and TM modes are:

$$f_{c_{nm}}^{\text{TE}} = \frac{p'_{nm}}{2\pi a\sqrt{\mu\epsilon}}, \quad f_{c_{nm}}^{\text{TM}} = \frac{p_{nm}}{2\pi a\sqrt{\mu\epsilon}}. \quad (2.77)$$

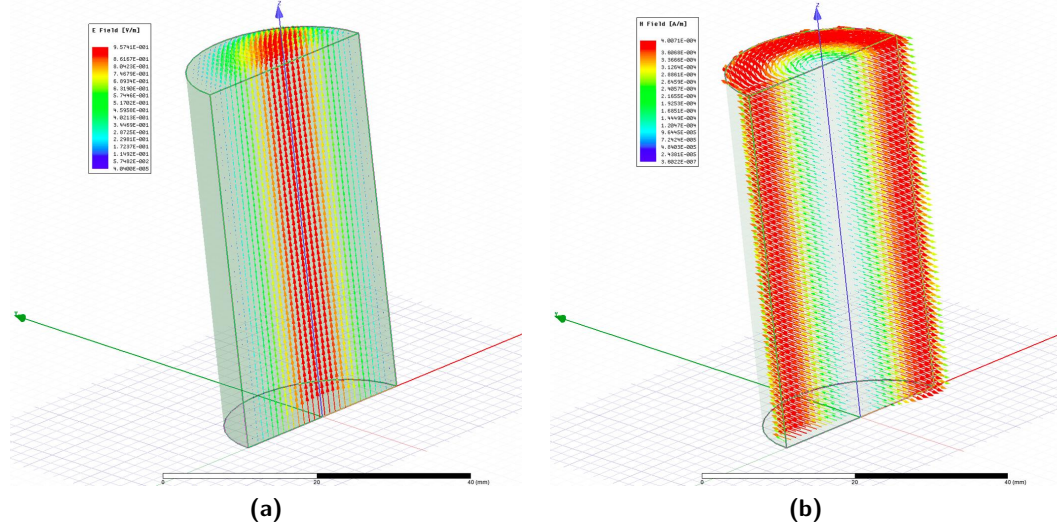


Figure 2.9: A simulation of the fields of TM₀₁₀ mode. Field lines of electric (left) and magnetic (right) fields are drawn. The pictures are obtained with the ANSYS-HFSS software. Provided by Ing. Simone Tocci.

This fact has been exploited for the design of Niobium-Titanium cavities (Sec. 3.2.2).

The two modes taken into account in this work are TM₀₁₀ and TM₁₁₀, and their field configurations are shown in Fig.s 2.9 and 2.10 respectively. For clarity, the pictures show only half of the cavity. Red arrows correspond to regions where the field is more intense. In both modes $l = 0$ and this corresponds to the fact that the electric field has no variations along the z axis. The difference between the electric field of the two modes resides in the n index: in TM₀₁₀ there is no variation in the ϕ coordinate, the field is maximum at $\rho = 0$ and falls off until it reaches a null value at $\rho = a$; in TM₁₁₀ the electric field varies with the ϕ coordinate and forms two lobes with opposite directions. The resonant frequency of all TM _{n m 0} modes doesn't depend on the length d and scales linearly with the radius a , so that it becomes:

$$f_{nm0} = \frac{c}{2\pi\sqrt{\mu_r\epsilon_r}} \frac{p_{nm}}{a}. \quad (2.78)$$

TM₀₁₀ is the mode configuration utilized in the search for axions through the axion-photon interaction with conventional haloscopes, like in the ADMX experiment (Sec. 1.2.5). Remembering the interaction term of eq. (1.49), the coupling is proportional to $\mathbf{E} \cdot \mathbf{B}$, where \mathbf{E} is the electric field of the excited resonant mode and $\mathbf{B} = \hat{z}B_0$ is the external static magnetic field. The interaction can then be maximized by the field lines of TM₀₁₀ of Fig. 2.9a, where \mathbf{E} is parallel to the z axis and maximum at $\rho = a$. Correspondingly the form factor C_{nml} , defined by eq. (2.18), is maximum for this mode thus optimizing the signal power for the axion-photon conversion of eq. (2.17) with respect to other resonant modes.

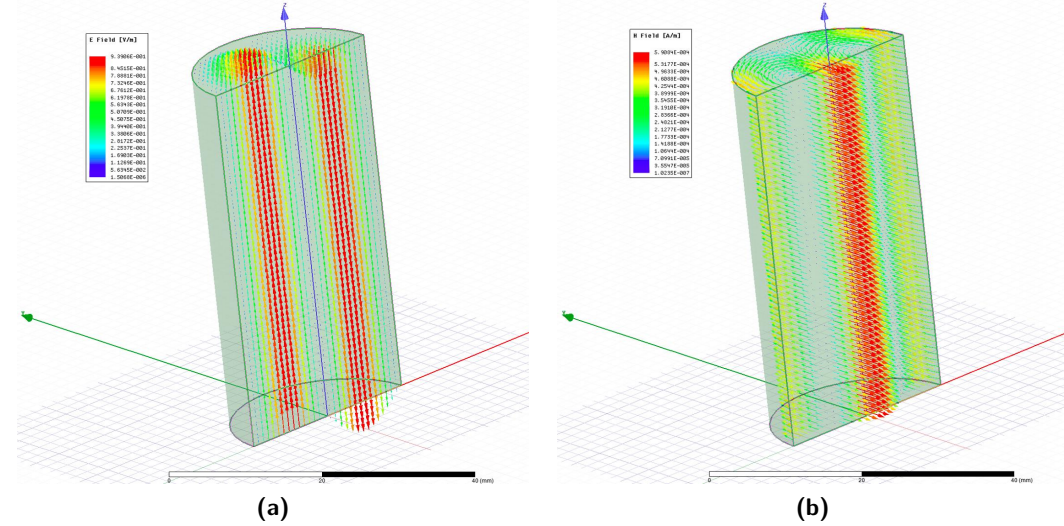


Figure 2.10: A simulation of the fields of TM₁₁₀ mode. Field lines of electric (left) and magnetic (right) fields are drawn. The pictures are obtained with the ANSYS-HFSS software. Provided by Ing. Simone Tocci.

TM₁₁₀, on the contrary, can be exploited for the detection of axions through their coupling with the electron spin, as in the QUAX experiment, described in Sec. 2.1.1. There we saw that the magnetization of the sample induced by the axion wind is the source of the magnetic field in the cavity. The two loops that the magnetic field lines of TM₁₁₀ of Fig 2.10b form have transverse components, and this allows to couple with the spin precession, that acquires a transverse component after the interaction. Furthermore, the magnetic field magnitude is maximum at the center of the cavity, where the magnetized samples are placed. Note also that the two opposite directions of the electric field of TM₁₁₀ cause a cancellation in the numerator of C_{nml} of eq. (2.18). This is the reason why TM_{nmo} modes, with $n \neq 0$, cannot be exploited for the axion-to-photon conversion in an empty cavity.

2.4 Goals of QUAX R&D and this thesis work

In the first chapter a particular attention was devoted to two axion detection techniques, here briefly summarized. Firstly it was proposed by Sikivie [6] that axions could be detected exploiting the axion-photon coupling. Axions can be converted into photons in the presence of a static magnetic field, and the emitted photons are collected in a microwave cavity. The power that can be read by a detector coupled to the microwave cavity is:

$$P_{\text{sig}}(a\gamma \rightarrow \gamma) = \omega_{\text{res}} \frac{\kappa}{1 + \kappa} g_{a\gamma\gamma}^2 \frac{\rho_a}{m_a^2} B_0^2 V_c C_{nml} Q_L. \quad (2.79)$$

Subsequently, Krauss *et al* [37] proposed to exploit the interaction between axions and electrons to detect the former. If a magnetized medium is put in a resonant cavity, when the axion couples to the spin of electrons the total magnetization is changed, and this excites a resonant mode. The power available after this interaction is:

$$P_{\text{sig}} = \frac{\kappa}{1 + \kappa} \frac{e}{m} \mu_B n_s \omega_a B_a^2 V_s \tau_{\min}. \quad (2.80)$$

The QUAX R&D is mainly directed at increasing these signal powers, that are small quantities and constitute a remarkable experimental challenge. One tries to enhance the emitted powers working on the experimental quantities that enter their expressions. The signal power for an axion-photon interaction (eq. (2.79)) depends on the quantity $Q_L B_0^2$, while the power for an axion-electron interaction (eq. (2.80)) depends on τ_{\min} , which contains the spin-spin relaxation time τ_2 and the cavity decay time τ_c defined as:

$$\tau_c \equiv \frac{Q_0}{\omega_{\text{res}}} \simeq 70 \mu\text{s} \left(\frac{Q_0}{10^6} \right) \left(\frac{14 \text{ GHz}}{\omega_{\text{res}}} \right), \quad (2.81)$$

and is the time after which $1/e$ of the energy stored in the cavity is dissipated (the energy decays exponentially with time).

Therefore the main purposes of the QUAX R&D are:

- to find a microwave cavity with high enough quality factor ($\sim 10^6$);
- to find a magnetized material with relaxation time as large as possible;
- to develop a single photon counter for suitable detection of the signal;
- secondly, to ensure a high uniformity of the external magnetic field.

This thesis work concentrates on the first topic. To achieve high quality factors, microwave cavities made of superconducting materials are employed. Due to the presence of an external magnetic field (in the first case to stimulate the axion conversion into a photon, in the second case to polarize the medium) type-II superconductors are involved, because they possess higher critical fields B_{c2} with respect to thermodynamic critical fields B_c of type-I superconductors (see Sec. 2.2.2 for the definition of the critical fields). During the period of the present work four superconducting cavities were characterized: a Niobium cavity, two Niobium-Titanium cavities and a Magnesium Diboride one. Among these, it was found that the most suitable resonant cavity that can be employed in the QUAX experiment is the Niobium-Titanium one, showing higher quality factors in the presence of B_0 with respect to the other cavities. To characterize the cavities, the unloaded quality factors were obtained with a fit procedure, presented in this work. These measurements are described in Sec. 3.2.

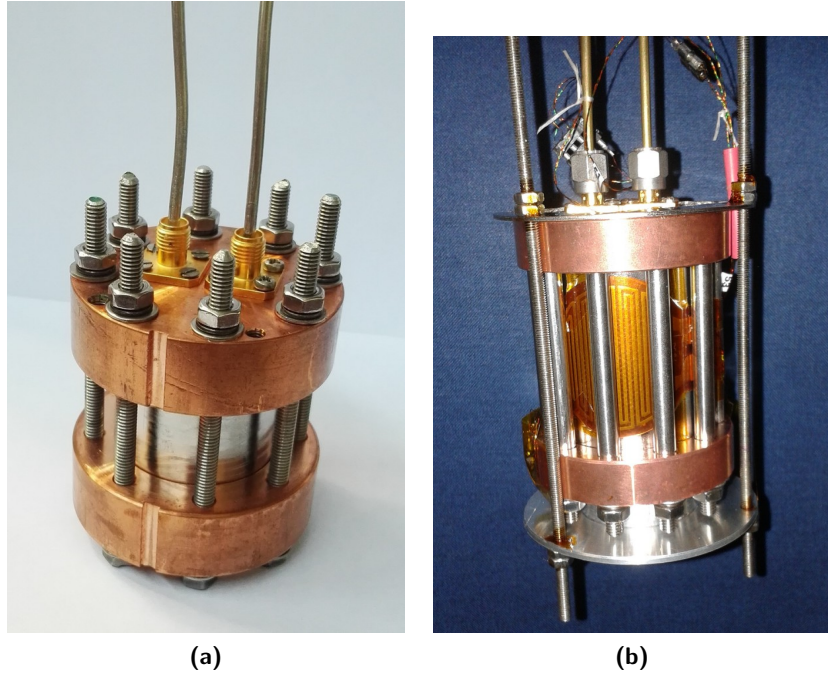


Figure 2.11: (a): Picture of a Niobium cavity. The copper coverings on the upper and lower edges of the cylinder contain the two Niobium lids and are employed to tighten the latter to the cylindrical walls. On the top there are two coaxial cables, outgoing from SMA connectors, that contain the antennas connected to the VNA (not shown). (b): The heater in contact with the external Nb cavity wall is visible.

On the other hand, the study of magnetic materials with high spin density n_s and large relaxation times is carried out at LNL. Currently YIG and GaYIG are being used, with a relaxation time of about $\tau_2 \simeq 0.11 \mu\text{s}$ [43].

2.5 Experimental set-up

This section is dedicated to the set-up of all the instrumentation that serves to the characterization of superconducting resonant cavities studied in the QUAX R&D phase at the National Laboratories of Frascati (LNF).

Cavities and cryogenic insert. For the scopes of the study the cavities under inspection are empty, so their relative permittivity ϵ_r and permeability μ_r are taken to be $\epsilon_r = \mu_r = 1$. The cavities must be fed with some source of power to test them, so they are coupled to two antennas entering their volume. The Fig. 2.11 shows a cavity of Niobium as an example. The two cables outgoing from two SMA connectors are coaxial cables, about 1 meter long, that contain antennas coupled to the cavity. The antennas are connected to the Vector Network Analyzer. The superconducting state is reached with low temperatures, so the cavity has to be inserted in a cryostat. It is therefore mechanically attached



Figure 2.12: (a): Cryogenic insert, with the cavity assembled at its edge. (b): Micrometers at the end of the cryogenic insert. They allow to finely tune the quote of the antennas in the cavity, with a resolution of $10 \mu\text{m}$. The copper cables are the antennas coming from the cavity.

to a cryogenic insert, shown in Fig. 2.12a. The antennas pass through the insert, and at its end there are two micrometers (Fig. 2.12b) to finely tune the position of the antennas inside the cavity. The resolution is $10 \mu\text{m}$. The cavity is also isolated from the outside thanks to an aluminum container (not shown in figure). The reason will be explained in the paragraph dedicated to the cryostat at page 68.

All the measured cavities have roughly the same dimensions, that are 26,1 mm of diameter and 50 mm of height. Correspondingly they have approximately the same resonant frequency.

The cavity is provided with a heater (Fig. 2.11b) and a temperature sensor (Cernox), while the pressure of the cryogenic insert is monitored by a pressure sensor.

Vector Network Analyzer. In our set-up the Vector Network Analyzer (VNA) (shown in Fig. 2.13), model Agilent E5071C, is the main instrument for radio-frequency measure-



Figure 2.13: The Vector Network Analyzer (VNA) connected to the antennas through low attenuation cables.

ments. It sends electromagnetic signals at microwave frequencies towards the cavity from one port and reads them back from a second port. Its range of frequencies covered goes from 300 kHz to 20 GHz. The most important quantities measured by the VNA are of course the frequency dependences of the real and imaginary parts of the scattering parameters of a network. An important feature, used for the characterization of the cavities, is the automatic calculation of the loaded quality factor of a resonance curve through the 3-dB method (described in Sec. 3.1.1).

From the ports of VNA two low attenuation cables come out (the black thick cables in Fig. 2.13). They are connected to the antennas housed in the cryogenic insert through SMA connectors. As discussed at the end of Sec. 2.2.1, a calibration procedure has been carried out for these cables, so the reference planes t_1 and t_2 of Fig. 2.3 are placed at the beginning of the antennas for our two-port measurements.

Cryostat. A cryostat is an instrument designed to cool the temperature of objects using cryogenic liquids, as liquid nitrogen or liquid helium. It is possible to control its temperature, increasing, decreasing or maintaining it constant. Our cryostat is shown in Fig. 2.14. Schematically it is a cylindrical container made of multiple concentric volumes⁷, each one having a different function; this schematization is drawn in Fig. 2.15, showing also the dimensions of the external case (clearly not in scale). We want to bring the temperature down to about 4 K in the region where the cavity lies, starting from a room temperature.

⁷Actually the structure is more complicated, but for the scopes of this chapter it is sufficient to describe it as a series of concentric cylinders.



Figure 2.14: The black cylindrical container is the cryostat. Also shown are a vacuum pump (the red one at the left of the cryostat) and the VNA (above the cryostat).

This would be impossible if the only shielding between the room environment and the volume at 4 K were the metallic external surface of the cryostat. Indeed, various stages comprising thermal isolation realized by vacuum volumes and liquid nitrogen (LN_2) reservoirs are realized. The heat transfer in this systems is mainly due to thermal conduction of the walls of the cryostat, convection of gases and radiation. To reduce conduction and convection, in the outer volume of the cryostat vacuum is realized. A pressure of about $(10^{-5} \div 10^{-6})$ mbar is reached when the system is at cryogenic temperatures. Heat transfer by radiation is due to the blackbody emission of the walls. The power emitted by a perfect blackbody follows the Stefan-Boltzmann law:

$$P(T) = \sigma_s A T^4,$$

with A the emission surface area and $\sigma_s = 5.67 \cdot 10^{-8} \text{ W m}^{-2} \text{ K}^{-4}$ the Stefan-Boltzmann constant. Thus, considering two parallel plates at temperatures T_1 and T_2 with the same area and emissivities different from zero, the power transfer per unit area is [51]:

$$P_{1 \rightarrow 2} \approx \sigma_s (T_1^4 - T_2^4). \quad (2.82)$$

For this reason after the first vacuum hollow there is a liquid nitrogen reservoir at a temperature of $T_{\text{LN}_2} \simeq 77 \text{ K}$, depicted with magenta lines in Fig. 2.15, so that the inner

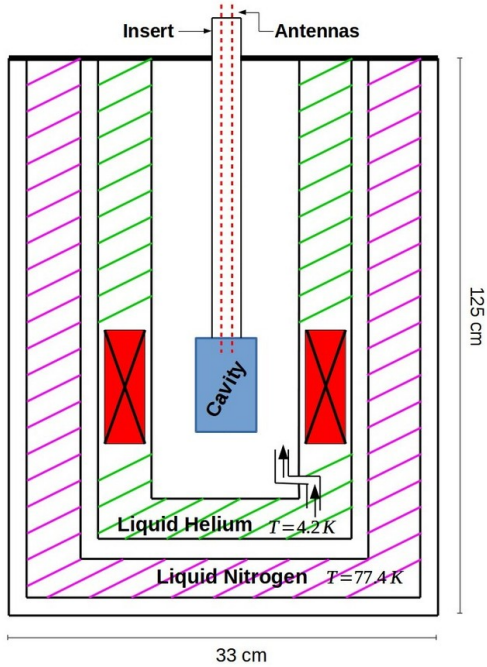


Figure 2.15: Simple concept of the concentric volumes in the cryostat. Also shown the cryogenic insert that connects the cavity and the antennas (in red dotted lines) to the external environment.

volume is thermally decoupled from the room temperature. After the LN_2 chamber, another vacuum hollow is present. Subsequently a ${}^4\text{He}$ container is found (the green area in Fig. 2.15). This reservoir is cooled down to $T_{\text{LHe}} = 4.2 \text{ K}$ that is the boiling temperature of helium under the pressure at sea level (1 bar). Here, immersed in the liquid helium bath, the superconducting solenoidal magnet is located (shown in red with black crosses in the figure), which produces the magnetic field inside the cryostat. The last hollow consists of the experimental volume, in which the test objects are placed, in this case the cryogenic insert with the cavity. The volume is cooled down to $T_{\text{LHe}} = 4.2 \text{ K}$ thanks to a needle valve together with a pumping system. The needle valve extracts liquid helium from the previous container and takes it in the experimental volume. The cavity is enclosed in an aluminum container, because the helium that evaporates in this last hollow causes the resonant frequency to shift towards lower values. In fact ϵ_r (the relative permittivity) grows if the helium density is increased, and correspondingly the resonant frequency changes as $f_{\text{res}} = f_0 / \sqrt{\epsilon_r}$, where f_0 is the resonant frequency in vacuum. Moreover, the helium that evaporates causes the cavity to vibrate, introducing noise in the measurements. However, the Al container is filled with some helium gas ($\sim 100 \text{ mbar}$) to ensure a heat exchange between the experimental volume and the cavity.

The experimental volume is provided with a pressure sensor, while the magnet housing has four temperature sensors at different altitudes to monitor the liquid helium level. A

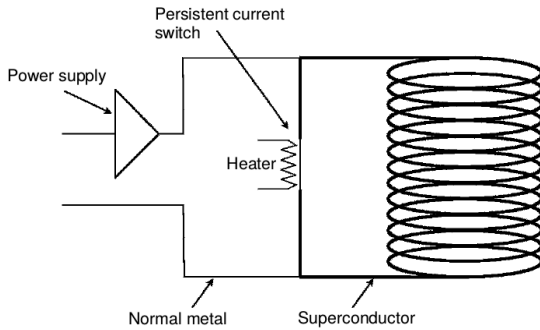


Figure 2.16: Sketch of magnet power supply with a superconducting switch. Taken from [51].

heater in contact with the external cavity walls (Fig. 2.11b) is used to change the increasing rate of the cavity temperature.

Magnet. The magnet providing the magnetic field in the experimental volume is a superconducting one. This is a solenoid made of NbTi wires shielded by a copper matrix, that has the safely function of dissipating the heat developed in case of quenching. Quenching consists of a sudden transition from superconducting to normal state in all the superconductor, and since generally the wires sustain high currents, the amount of power generated in the transition would cause evaporation of the LHe bath. The magnet's maximum field magnitude is 8 T, the bore diameter is 77 mm and the homogeneity degree is 1 part in 10^3 over a 10 cm diameter sphere about the magnetic center.

The magnet is energized by a power supply through a superconducting *switch*, schematically shown in Fig. 2.16. The wined lines represent the magnet wires; they are short-circuited by the switch, that is a superconducting filament of NbTi (called "persistent current switch" in the picture). At the edges of the switch also the normal metal cables are connected, and they carry the energizing current from the power supply. When the *heater* is on, the filament is in a normal state and current flows from the cables to the superconducting wires. When the desired current value (or equivalently a magnetic field value) is reached, the heater is switched off and the filament transitions to the superconducting state, thanks to the cryogenic bath surrounding it, short-circuiting the wires. From now on the current can flow in the magnet without additional power supply.

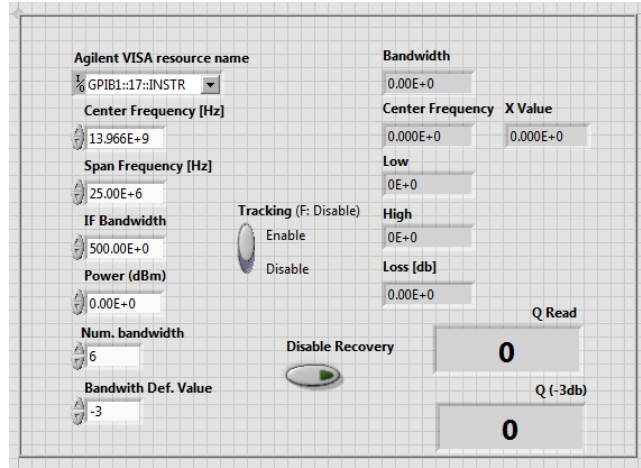
Pre-cooling operations. Each volume of the cryostat is connected to the outside with some valve. Before any operation with the cryostat, they are all pumped with cryogenic pumps. The vacuum hollows are connected to the same pump and a pressure of about $(10^{-3} \div 10^{-4})$ mbar is reached (lower values are attained when cooling at cryogenic temperatures, because of the cryopumping). All the other volumes are firstly pumped at about 1 mbar, then a *flushing* process with helium gas is performed. Flushing operations are

necessary to eject the air that may be present in the cryostat. About 80% of air consists of nitrogen, and the solidification temperature of N₂ is about 63 K. Thus, when liquid helium is inserted, if nitrogen is present it undergoes an unwanted solidification. This can cause the needle valve to get stuck.

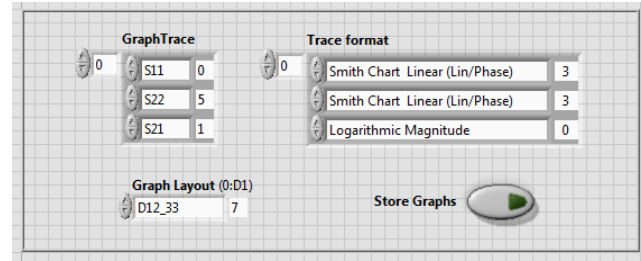
The flushing procedure is as follows. After pumping, helium gas is introduced in the magnet housing (that subsequently will host liquid helium) and then it is again pumped away. The operation is iterated two or three times. Afterwards, this volume is filled again with gas helium and a small overpressure is realized. Then, opening the needle valve, helium is transferred from the magnet hollow to the experimental volume, and consequently it is pumped away. Also these steps are repeated two or three times.

After that, the cooling procedure can start: firstly the cryostat is filled with liquid nitrogen, and when a temperature of ~ 100 K is reached liquid helium is inserted. This reduces the initial helium consumption; in fact helium has a small latent heat and if it got in contact with surfaces at room temperature it would quickly evaporate.

All the instrumentation is controlled via the software LabVIEW. In Figures 2.17 and 2.18 the main functions of the control panel are shown. In the panel of Fig 2.17a the features that allow to change some parameters of the VNA, like the frequency range and the central frequency of the spectrum, are reported along with an indicator of the loaded quality factor determined by the 3-dB method (Sec. 3.1.1). The controls shown in Fig. 2.17b allow the storage of the $S_{11}(\omega)$, $S_{21}(\omega)$ and $S_{22}(\omega)$ data. Figure 2.18 shows the panels that control the thermodynamic parameters: temperature and pressure. The temperature sensor is positioned on the external surface of the cavity wall. The first pressure value refers to the pressure measured in the experimental volume, where the cryogenic insert is stored, while the second value refers to the pressure inside the aluminum container for the cavity.

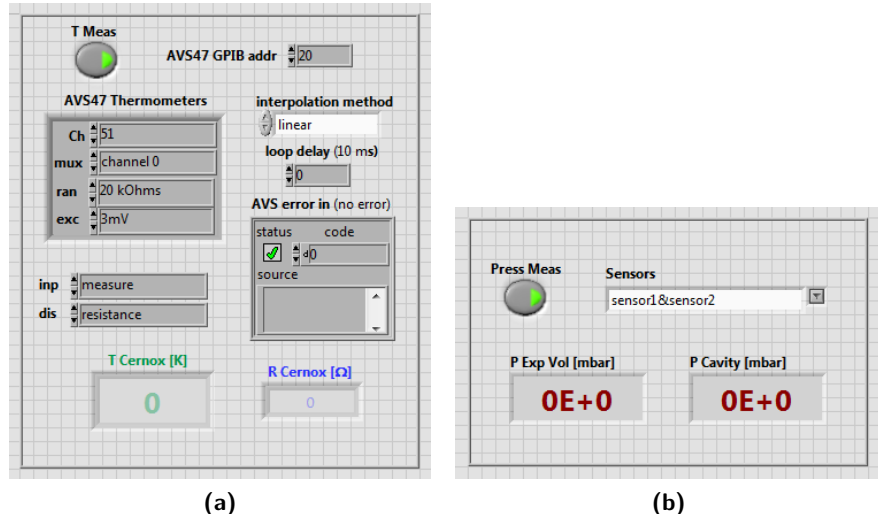


(a)



(b)

Figure 2.17: (a): Part of the panel control that allows to set some of the VNA parameters, such as the center frequency of the sweep, its range and the power injected in the cavity. Also shown the Q_L value measured with the 3-dB method. (b): These features allow to select the curves to store and their visualization format, like linear units or decibels.



CHAPTER 3

Characterization of the resonant cavities

In this final chapter the measurements of the microwave superconducting cavities available at LNF during the period of this work are described, and the results obtained are presented. In Sec. 3.1 the methods to determine the quality factors are discussed. In particular the 3-dB method is used by the VNA to measure Q_L values, while a modified Lorentzian fit was employed in this work to characterize the unloaded quality factors. In Sec. 3.2 the measurements performed are reviewed and commented.

3.1 Q determination

The loaded quality factor Q_L of a resonator is easily found by measuring the bandwidth of a resonance curve. Nevertheless, looking at eq. (2.49) $Q_L = Q_0/(1 + \kappa)$, where now with two ports κ is $\kappa_1 + \kappa_2$, we see that Q_L is a function of the couplings to the external circuit. Thus the determination of the unloaded Q_0 is needed to fully characterize a resonant cavity.

There are many techniques to measure the Q_L and Q_0 quality factors and resonant frequencies [52, 53, 54]. Nowadays the measurements are digital and automatically made by network analyzers or made using data collected by them. The techniques employed in this work are the 3-dB method used by the VNA for the determination of Q_L and a modified Lorentzian fit to extract the Q_0 values.

3.1.1 Q_L measurements through the 3-dB method

The 3-dB method, treated in more detail in Appendix B, relies on the measurement of the bandwidth of the resonance curve $S_{21}(\omega)$ at a particular value. The loaded quality factor of a resonator is determined by:

$$Q_L = \frac{1}{BW} \equiv \frac{\omega_0}{\bar{\omega}_2 - \bar{\omega}_1}, \quad (3.1)$$

where BW is a *fractional bandwidth*. The frequencies $\bar{\omega}_1$ and $\bar{\omega}_2$ in its expression are the frequencies at which $|S_{21}(\bar{\omega})|^2 = (1/2)|S_{21}(\omega_0)|^2$. The difference between the $|S_{21}(\bar{\omega})|^2$ and $|S_{21}(\omega_0)|^2$ values in decibels is 3 dB (see eq. (B.8)). Thus it suffices to find the maximum of the $|S_{21}|^2$ curve (occurring at ω_0) and measure the frequencies $\bar{\omega}_1$ and $\bar{\omega}_2$, for which the curve has a value 3 dB lower than $|S_{21}(\omega_0)|^2$, to determine the loaded quality factor (eq. (3.1)). This determination of Q_L is automatically performed by our Vector Network Analyzer. As explained in the next subsection, these Q_L values can only be used *together* with a Lorentzian fit to extract the Q_0 factors, since the VNA fails to measure Q_L when the two antennas interfere.

Note that one could extract the Q_0 values by only performing a fit of the S_{11} and S_{21} functions, but this would require to store S_{11} and S_{21} data for all the magnetic field values¹ and analyze them. This is a time-expensive procedure. Then, we proceed as follows:

- We take some points as reference values (see the star black points in Fig. 3.6) and store offline the S_{11} and S_{21} data for these points.
- We perform the fit procedure (see the next subsection) to extract the Q_0 values for the reference points.
- We convert all the measured Q_L points in Q_0 values through a linear interpolation between the reference points.

This scheme is again motivated and expanded in the next subsection.

3.1.2 Q_0 determination through a fit procedure

As anticipated at the beginning of this chapter, the unloaded quality factor Q_0 is necessary to fully characterize a resonant cavity. The standard measurements of Q_0 [55, 53] rely on, separately, reflection-type methods, in which S_{11} is measured, or transmission-type measurements. In the latter, S_{21} is determined in the condition that the coefficients κ_1 and κ_2 are equal, so that using eq. (B.6) at resonance and defining $\kappa \equiv \kappa_1 = \kappa_2$, it becomes:

$$S_{21}(\omega_0) = \frac{2\kappa}{1 + 2\kappa},$$

¹We are interested in $Q_0(B)$ dependences, see Fig. 3.6 for an example.

and determining κ by the inverse yields:

$$\kappa = \frac{S_{21}(\omega_0)}{2(1 - S_{21}(\omega_0))}$$

Using now eq. (2.49), the unloaded quality factor can be calculated knowing Q_L and $S_{21}(\omega_0)$:

$$Q_0 = \frac{Q_L}{1 - S_{21}(\omega_0)}. \quad (3.2)$$

Often cited in the literature is also the Lorentzian fit procedure [52, 56] to determine the quality factor and the resonant frequency. The acquired frequency and S_{21} data are fitted with an ideal Lorentzian curve. In fact, taking the expression of the complex transmission coefficient (eq. (2.57)) and calculating its magnitude as $|S_{21}(\omega)| = \sqrt{\text{Re}^2(S_{21}) + \text{Im}^2(S_{21})}$, gives:

$$|S_{21}(\omega)| = \frac{S_{21}(\omega_0)}{\sqrt{1 + Q_L^2 \delta^2}}. \quad (3.3)$$

The trend of this curve is shown in Fig. 3.1b.

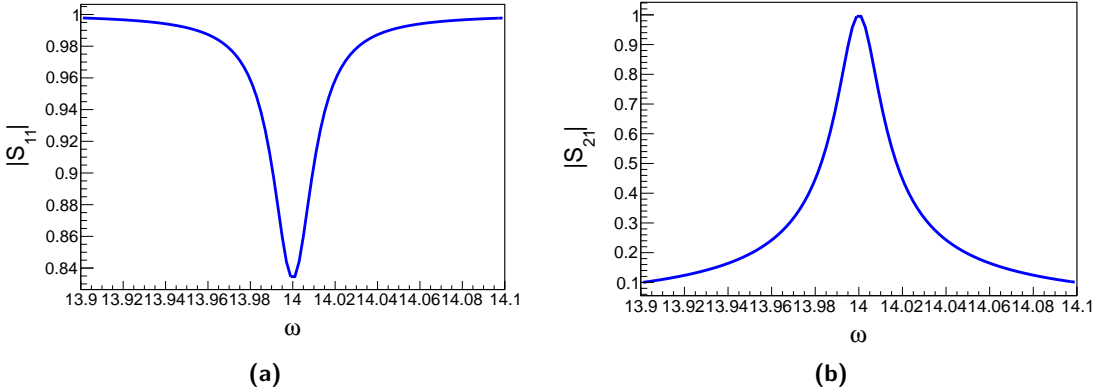


Figure 3.1: (a): the ideal reflection coefficient. (b): the ideal Lorentzian resonance curve. Both quantities are plotted in arbitrary units, and the parameters are $S_{21}(\omega_0) = 1$, $Q_L = 700$, $\omega_0 = 14$ and $\kappa = 0.1$.

Note that from eq. (3.2) a Q_0 value could be determined measuring Q_L with the 3-dB method of subsec. 3.1.1 and $S_{21}(\omega_0)$, but this requires $\kappa_1 = \kappa_2$. In our case the coupling coefficients κ_i are neither equal nor under control. In fact the antennas are very close to each other, within a distance of about 1 cm, and this causes a cross-talk between them (they exchange energy with each other). Then eq. (3.2) is no longer reliable. Moreover, when the cross-talk is present, the VNA measures wrong values of Q_L : this is due to the fact that the cross-talk causes a distortion of the S_{21} curve, introducing an asymmetry as shown in Fig. 3.2b, but the instrument assumes a symmetric curve to make its calculations. The distortion of the cross-coupling between antennas to the S_{21} shape also causes the

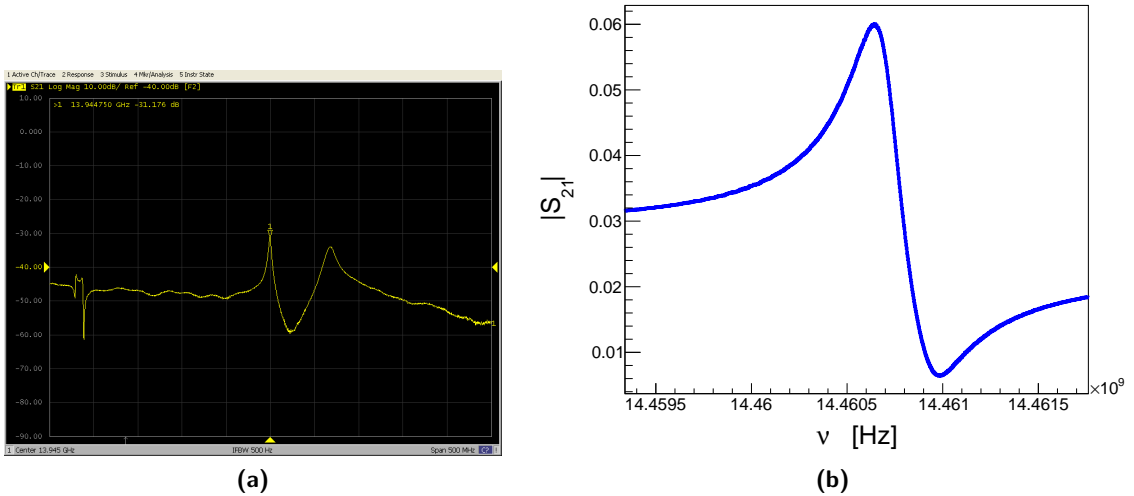


Figure 3.2: (a): a shot of the VNA screen, showing the frequency sweep. There is a resonant mode at the central frequency, with its right tail distorted by the cross-talk and a close resonant mode to the right. The y axis is in dB units. (b): an example of the S_{21} asymmetry for a NbTi cavity mode at about $\nu_0 \approx 14.46$ GHz, at a temperature of $T = 4.2$ K.

ideal Lorentzian fit to fail.

For these reasons we determine the quality factor executing a combined fit of $|S_{11}(\omega)|$ and $|S_{21}(\omega)|$, using a customized Lorentzian model for the $S_{21}(\omega)$ curve. For only *some*² of the Q_L values measured by the VNA we store offline the data of the corresponding S_{11} and S_{21} scattering parameters. The fit is executed to obtain a Q_0 value for these points. Subsequently, a linear interpolation function is used to convert *all* the measured Q_L values in unloaded quality factors. This method has been first tested with the Niobium cavity (Sec. 3.2.1), and Fig. 3.7 shows the points where the fit was executed as black squares. Between each couple of Q_L fitted values there are all the other measured Q_L s, and these are converted in Q_0 values thanks to the interpolation function shown as a grey line.

The S_{11} and S_{21} data stored offline consist in the values of frequency ν , real part $\text{Re}(S_{ij})$ and imaginary part $\text{Im}(S_{ij})$ of all the sampled points of the curves. The default sampling of the instrument consists of 1001 points for any choice of the frequency range, so that the resolution of a frequency sweep is $\Delta\nu = (\nu_{\max} - \nu_{\min})/1001$.

Fitting function. In Ref. [56] the importance of a fitting strategy with non-idealities (e.g. adding asymmetries to the S_{21} curve) is emphasized. The authors stress that the best-behaving fitting approach for their data is the one that considers an ideal Lorentzian curve with the addition of a cross-coupling term due to the ports. In our case both the cross-coupling and the presence of spurious modes are taken into account, because they

²As shown in Fig. 3.6a the fitted points are taken at different magnetic field values. The star points are approximately equally separated, and they cover the whole range of magnetic field values.

are both present (see Fig. 3.2a). Two additional modes are considered, one called $S_{21}^{(1)}$ with resonant frequency $\nu_1 < \nu_0$, where ν_0 pertains the mode of interest, and one called $S_{21}^{(2)}$ with $\nu_2 > \nu_0$. They parametrize the skewness of the main curve with their tails. Since they parametrize two modes, $S_{21}^{(1)}$ and $S_{21}^{(2)}$ are written as Lorentzian curves alike $S_{21}^{(0)}$ of eq. (2.57). The most general form of these quantities is obtained by adding a phase to each one and considering the factor $e^{-2j\beta l}$ due to a phase shift of the waves travelling through the antennas (see eq. (2.59) and its derivation). However, $e^{-2j\beta l}$ can be dropped since it is a common phase to each term, irrelevant when considering the modulus, and it was found that it suffices to consider only one relative phase between the resonances. Thus the total S_{21} curve has been written as:

$$S_{21}^{\text{TOT}} = S_{21}^{(0)} e^{j\theta} + S_{21}^{(1)} + S_{21}^{(2)}.$$

Note that to take into account the cross-talk of the antennas, it would be sufficient to add a complex number to the ideal Lorentzian curve. Thus in this case the extra terms $S_{21}^{(1)}$ and $S_{21}^{(2)}$ written as Lorentzian functions parametrize both the cross-coupling and the spurious modes. Taking equation (B.6) and redefining it adding the $e^{j\theta}$ factor, the $S_{21}^{(0)}$ of the mode of interest is:

$$S_{21}^{(0)} = \frac{S_{21}^{(0)}(\nu_0)}{1 + jQ_L\delta} e^{j\theta} = \frac{2\sqrt{\kappa_1\kappa_2}}{1 + \kappa_1 + \kappa_2 + jQ_0\delta} e^{j\theta},$$

where now κ_1 , κ_2 , Q_0 and ν_0 (present in the definition of δ , see eq. (2.30)), as well as θ , are parameters to be determined by the fit. After rationalization, the real and imaginary parts of $S_{21}^{(0)}$ are:

$$\text{Re}(S_{21}^{(0)}) = \frac{S_{21}(\nu_0)}{1 + Q_L^2\delta^2} \cos \theta - \frac{S_{21}(\nu_0)Q_L\delta}{1 + Q_L^2\delta^2} \sin \theta, \quad (3.4a)$$

$$\text{Im}(S_{21}^{(0)}) = -\frac{S_{21}(\nu_0)}{1 + Q_L^2\delta^2} \sin \theta - \frac{S_{21}(\nu_0)Q_L\delta}{1 + Q_L^2\delta^2} \cos \theta. \quad (3.4b)$$

The expression of the other modes is simply:

$$S_{21}^{(k)} = \text{Re}(S_{21}^{(k)}) + j \text{Im}(S_{21}^{(k)}) = \frac{A^{(k)}}{1 + (Q_L^{(k)}\delta^{(k)})^2} - j \frac{A^{(k)}Q_L^{(k)}\delta^{(k)}}{1 + (Q_L^{(k)}\delta^{(k)})^2},$$

with $k = 1, 2$. Here $A^{(k)}$ (real), $Q_L^{(k)}$ and ν_k (present in $\delta^{(k)}$) are the maximum values of the resonances, the loaded quality factors and the resonant frequencies, respectively, of the spurious modes. The real and imaginary parts of the total S_{21} can be taken to be the

sum of the three functions defined above:

$$\text{Re}(S_{21}^{\text{TOT}}) = \sum_k \text{Re}(S_{21}^{(k)}) \quad \text{Im}(S_{21}^{\text{TOT}}) = \sum_k \text{Im}(S_{21}^{(k)}), \quad (3.5)$$

and then the modulus:

$$|S_{21}^{\text{TOT}}| = \alpha_{21} \sqrt{\text{Re}^2(S_{21}^{\text{TOT}}) + \text{Im}^2(S_{21}^{\text{TOT}})}, \quad (3.6)$$

where α_{21} is a real constant parameter accounting for the cables attenuation, typical of transmission lines. This is the function used to fit the S_{21} data.

On the contrary, for the scattering parameter S_{11} only the contribution of the mode of interest, $S_{11}^{(0)}$, is considered. This is a good approximation for high Q values, since correspondingly the bandwidths are very narrow. The function has some discrepancies with data when lower Q fits are executed, because the power spectrum is modulated by a sinusoidal function due to spurious reflections in the cables (see Fig. 3.8b). Taking eq. (2.54), the real and imaginary parts are:

$$\text{Re}(S_{11}^{(0)}) = \frac{\kappa_1^2 - (1 + \kappa_2)^2 - Q_0^2 \delta^2}{(1 + \kappa_1 + \kappa_2)^2 + Q_0^2 \delta^2}, \quad (3.7a)$$

$$\text{Im}(S_{11}^{(0)}) = \frac{-2\kappa_1 Q_0 \delta}{(1 + \kappa_1 + \kappa_2)^2 + Q_0^2 \delta^2}, \quad (3.7b)$$

and then the modulus:

$$|S_{11}^{(0)}| = \alpha_{11} \sqrt{\text{Re}^2(S_{11}^{(0)}) + \text{Im}^2(S_{11}^{(0)})}, \quad (3.8)$$

where α_{11} is the real and constant attenuation parameter for this function. This is the function used to fit the S_{11} data.

Finally, the ROOT software routine for fitting unidimensional histograms has been used to perform the *combined* fit of the S_{11} and S_{21} shapes. Their data are put beside in a single histogram, as shown in Fig. 3.3. To do this, the frequency values of the S_{21} curve have been shifted as follows:

$$f = \nu + (\nu_{\max} - \nu_{\min}),$$

where ν are the frequencies acquired by the VNA and $(\nu_{\max} - \nu_{\min})$ is the range selected with the instrument. With this definition, the fitting function has been built as follows:

$$FF = \begin{cases} |S_{11}^{(0)}(\nu)| & \text{if } \nu_{\min} \leq \nu < \nu_{\max}, \\ |S_{21}^{\text{TOT}}(\nu)| & \text{if } \nu_{\max} \leq f < (2\nu_{\max} - \nu_{\min}). \end{cases} \quad (3.9)$$

This is the function that parametrizes the data to extract the unloaded quality factor, and

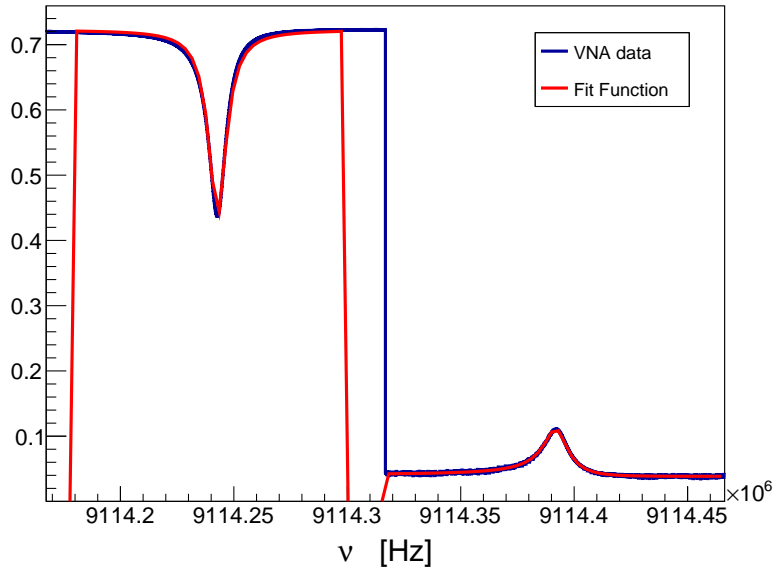


Figure 3.3: Example of a fit executed on the NbTi cavity mode TM_{010} , with resonant frequency $\nu_0 \simeq 9.114$ GHz at $T = 4.2$ K. The S_{21} data (the peak on the right) are put beside the S_{11} data with a frequency shift. The blue line represents the data taken from the VNA, while the red line is the fitting function.

has a total of 13 free parameters: κ_1 , κ_2 , Q_0 , $Q_L^{(1)}$, $Q_L^{(2)}$, ν_0 , ν_1 , ν_2 , $A^{(1)}$, $A^{(2)}$, α_{11} , α_{21} and θ .

Table 3.1: The table reports the values of critical temperatures and critical magnetic fields of the superconducting materials involved in these measurements. All the critical temperatures are taken by the measured data with no applied magnetic field, $B = 0$ T. The critical fields B_{c1} and B_{c2} of Nb are estimated by our data, while the value of B_{c2} of NbTi is a theoretical value at $T = 0$ K taken from [57] (B_{c1} is very small). The estimate of B_{c1} for MgB₂ is taken from [58], while B_{c2} is estimated at 4 K from the work of Ref. [59].

	Nb	NbTi	MgB ₂
type	bulk	film	bulk
T_c [K]	≈ 9	≈ 7.8	≈ 38
B_{c1} [T]	≈ 0.22		$0.025 \div 0.048$
B_{c2} [T]	$0.5 \div 0.6$	13	≈ 15

3.2 Measurements

Four cavities have been studied during the period of this thesis work: a Niobium (Nb) cavity, two Niobium-Titanium (NbTi) cavities and a very first test of a Magnesium Diboride (MgB₂) one was performed. Niobium is an element, NbTi is an alloy and MgB₂ is an ionic compound. They all are type-II superconductors (see Sec. 2.2.2), and their main properties are summarized in Tab. 3.1. Since in both the QUAX operation modes (one testing $g_{a\gamma\gamma}$ and the other testing g_{aee} , see Sec. 2.1) a static magnetic field has to be applied, we are interested in the unloaded quality factor Q_0 dependence on the external magnetic field B . This gives informations about the superconducting properties of the cavities, such as the resistivity and the type of flux pinning. In fact Q_0 is directly related to the surface resistivity (eq. (2.31)) and then to RF losses. The $Q_0(B)$ dependence also allows to deduce some results concerning the sensitivity for the axion detection. The trend of the loaded quality factor Q_L with temperature is also studied. These measurements and the interpretation of the results are given in this section. The Niobium-Titanium cavity is, among the studied cavities, the most suitable for the scopes of the QUAX experiment. Here the notions of superconductivity given in Sec. 2.2.2 are used, as the Meissner state, fluxons, flux flow regime, flux flow resistivity and losses, etc.

Measurement procedures

Before starting with the analysis of the cavities, here a summary of the measurement procedures is given.

- (a) The resonant cavity is assembled to the cryogenic insert (Fig. 2.12a). The latter is inserted in the cryostat (Fig. 2.14) at room temperature.
- (b) The flushing process with helium gas is performed to clean the cryostat. Subsequently, it is cooled with liquid nitrogen, and when temperature reaches ≈ 100 K the cryostat

is filled with liquid helium. $T = 4.2$ K is reached.

- (c) Q dependence on B at $T = 4.2$ K: the magnetic field is increased since B_{c2} is exceeded, while the VNA acquires the Q_L values. Then B is brought again to zero. During this measurement the waveforms of S_{11} and S_{21} are stored offline.
- (d) Q dependence on T : a magnetic field value is chosen and kept fixed. The heater (Fig. 2.11b) is used to warm the cavity since T_c is exceeded, while the VNA acquires Q_L data. Then the cavity is cooled again, with the same applied field value.
- (e) Data analysis is performed to extract Q_0 values with the fit of the S_{11} and S_{21} waveforms.

3.2.1 Niobium resonant cavity

The Niobium cavity was the first superconducting cavity that has been tested, and was mainly used to improve the experimental set-up and to test the fit procedure. As discussed below, the Nb cavity cannot be used in the QUAX experiment, because it has a too small critical field B_{c2} (see Sec. 2.2.2 for the definition of the critical field).

In a first measurement the Nb cylinder was closed with copper lids, that allowed to make an aperture to house a Hall probe, with which the magnetic field inside the cavity was directly measured. At this time the cavity was not isolated with the aluminum container³. The magnetic field values inside the cavity were taken with a Hall probe and are plotted in Fig. 3.4. Both Zero-Field Cooling (ZFC) type and Field-Cooling (FC) type measurements were performed, but in a slightly different way as described in Sec. 2.2.2.

- The ZFC data are obtained, as illustrated in Sec. 2.2.2, by cooling the sample at the desired temperature, $T = 4.2$ K in our case, with no applied magnetic field. Once reached this working temperature, the magnetic field is turned on, and is increased until $B_{app} > B_{c2}$ (at 4.2 K) is reached. This field value causes the material to transition to the normal state.
- At this point the sample is not re-heated (and this is the difference with the procedure of Sec. 2.2.2), and the magnetic field is brought back to zero at fixed temperature (always 4.2 K), giving the FC-type measurement.

On the basis of what was just explained, a graph showing ZFC and FC data (as Fig. 3.4) has to be read starting from the ZFC data at $B_{app} = 0$ T. Then magnetic field values must be followed until the maximum applied field is reached. From this point the FC data must be taken into account, following decreasing B_{app} fields until 0 T (still on the FC curve).

³See the paragraph "Cryostat" at page 68 for a discussion on why this was introduced.

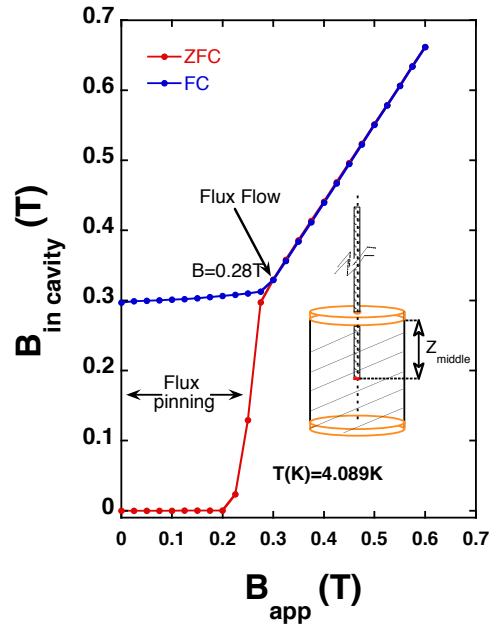


Figure 3.4: Measurement of the trapped magnetic field in the Nb cavity versus the applied magnetic field at temperature $T \simeq 4$ K. The measurement was performed with the Hall probe. ZFC data is in red and FC data is in blue. The value of the field at which flux flow starts is also indicated.

In Fig. 3.4 ZFC data is in red and FC data is in blue; the Hall probe measures magnetic field values, so the ZFC curve indicates that applied magnetic fields $B_{app} \lesssim 0.2$ T are completely excluded from the superconductor, corresponding to the Meissner state, where B inside the cavity is zero (see Sec. 2.2.2). For higher values, in the range $0.2 \text{ T} \lesssim B \lesssim 0.28$ T flux quanta (paragraph "Type-II superconductors" in Sec. 2.2.2) start to penetrate the material. Above $B \approx 0.285$ T the sample enters the flux flow regime (pag 58 of Sec. 2.2.2), where the flux tubes move and the hysteretic behaviour of the magnetization is not present. This value of magnetic field can be extracted thanks to the deviation of the FC curve (blue data) with respect to the ZFC curve. In fact, when the magnetic field is turned off, the FC data show that there is trapped field inside the cavity, because flux lines are not perfectly expelled. This behaviour is due to the presence of flux pinning (see page 58 of Sec. 2.2.2).

A second measurement was realized with the cavity closed with Nb lids, one of which had two apertures allowing the antennas to enter the cavity volume. The antennas were not movable, and the aluminum container to isolate the cavity was not yet present. In

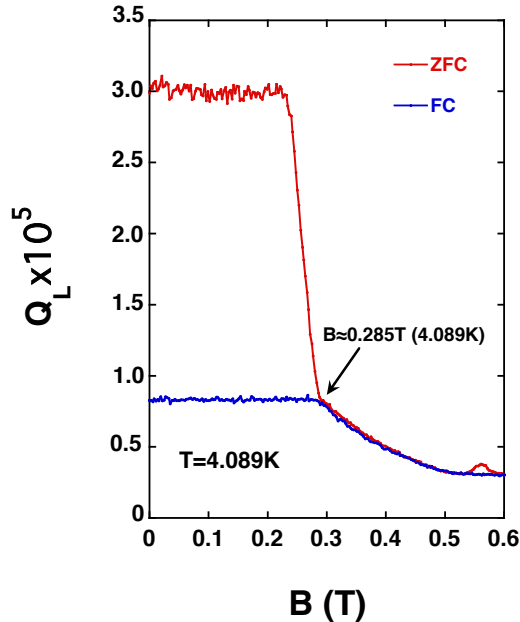


Figure 3.5: Loaded quality factor of the TM_{110} of the Nb cavity at $T \simeq 4$ K. In red the ZFC data and in blue the FC data. Also shown the value of magnetic field at which flux flow starts.

this case a different quantity was measured: the loaded quality factor Q_L dependence on the external field B , varying from 0 T to 0.6 T (at temperature $T \simeq 4.1$ K). Both ZFC type and FC type measurements were performed, shown in Fig. 3.5. In the ZFC curve the quality factor maintains a constant value until about $B \approx 0.22$ T, since the magnetic field is excluded (Meissner state). Then it falls off rapidly because the superconductor starts to enter its mixed state, and then undergoes flux flow. The reason of the quality factor decrease resides in the fact that the flux tubes penetrating the superconductor have a normal core, that dissipate energy. In a flux flow regime the fluxons move, and this results in the presence of a resistivity ρ_f (as described in Sec. 2.2.2, eq. (2.71)). Furthermore, as can be seen from the plot, the Q_L values of the FC curve (blue data) do not reach the same values as the ZFC curve, at fields $B \lesssim 0.285$ T. As before, this is an indication of the presence of trapped magnetic field (or a magnetization different from zero) in the superconductor, and this hysteretic behaviour is due to the pinning. So, when turning the magnetic field off, flux lines are not completely expelled, but some are trapped inside. Thus the remained normal cores continue to dissipate energy.

It must be noted that the fixed position of the antennas doesn't allow to tune the coupling coefficients κ_1 and κ_2 , and this reflects on the low measured values of Q_L at

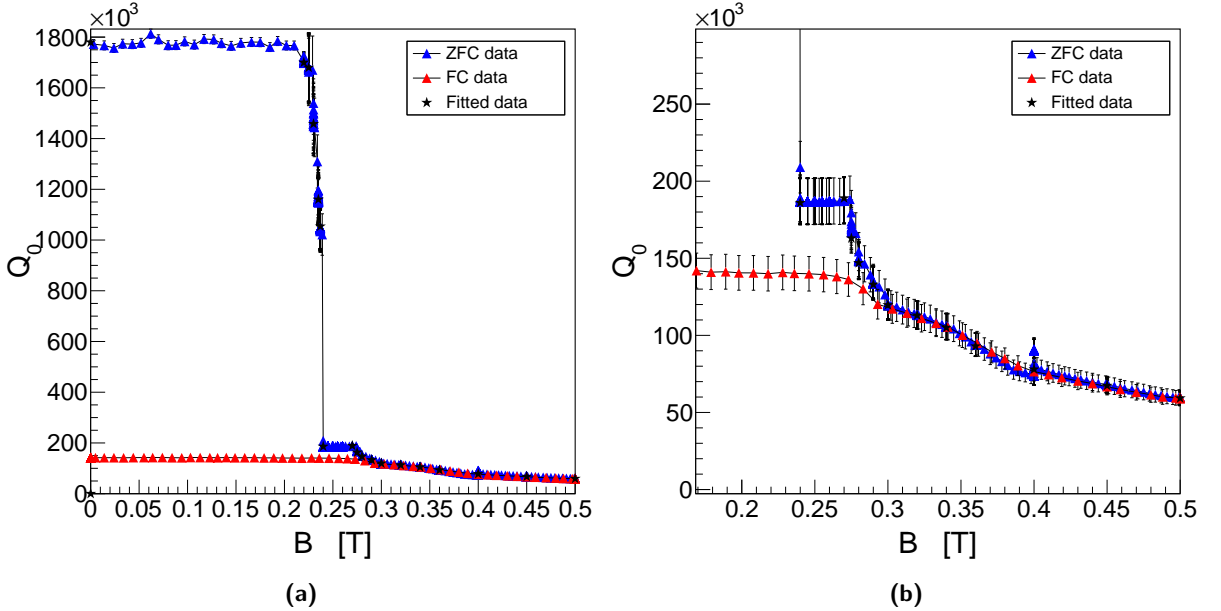


Figure 3.6: (a): the plot shows the trend of Q_0 in the range $0 \text{ T} \leq B \leq 0.5 \text{ T}$ for the TM_{110} mode of the Nb cavity (resonant frequency $\nu_0 = 13.994 \text{ GHz}$), at temperature $T = 4.2 \text{ K}$. (b): a detail of the ZFC and FC curves for $B > 0.17 \text{ T}$; at about $B \simeq 0.28 \text{ T}$ the FC curve deviates from the ZFC curve, indicating the presence of trapped magnetic field in the bulk of the cavity.

small B fields for the ZFC curve with respect to the expected ones, of about a million. Furthermore, the absence of the aluminum container lets the helium vapours enter the cavity, and this causes the resonant frequency to shift and to strongly vary with temperature fluctuations (paragraph "Cryostat" at page 68).

The last and ultimate set-up, instead, includes the possibility to finely tune the depth of the antennas inside the cavity thanks to the micrometers, as described at page 66, and the aluminum container is used. The latter is filled with some helium gas ($\sim 100 \text{ mbar}$) to ensure a thermal contact between the liquid helium in the experimental volume and the cavity, without appreciably changing its resonant frequency. The Nb cavity employed has been shown in Fig. 2.11. In this configuration the application of the fitting function of eq. (3.9) was tested for the first time. Fig. 3.6a shows the Q_0 values extracted from the fit procedure for both the ZFC curve (blue data) and FC curve (red data). Data are relative to the TM_{110} mode (see Sec. 2.3 for a description of the modes), with resonant frequency $\nu_0 = 13.994 \text{ GHz}$ at $T = 4.2 \text{ K}$. We see that in this case the cavity mode reaches $Q_0 \simeq 1.8 \cdot 10^6$ for magnetic fields $B \lesssim 0.24 \text{ T}$, corresponding to $Q_L \simeq 1.5 \cdot 10^6$ (see Fig. 3.7), thanks to the possibility to have a small coupling between the cavity and the power source, tuning the antennas.

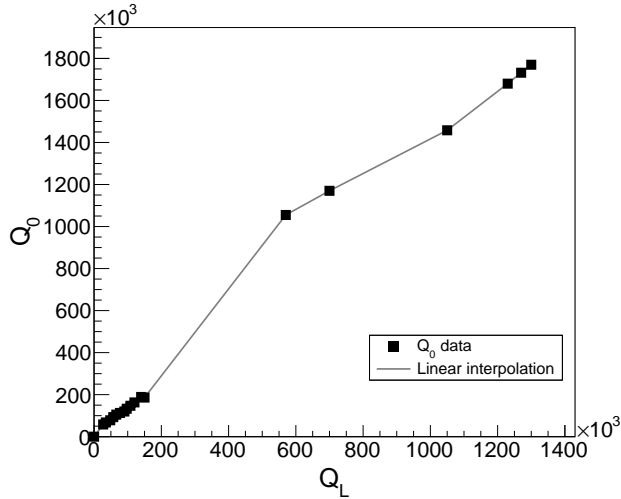


Figure 3.7: The correspondence between Q_L values and interpolated Q_0 values for the Nb cavity. The black squares are the fitted data and the line represents the interpolation function. The error bars are not present, see the discussion in the text.

The star black points in Fig. 3.6a represent the actual points for which the fit to achieve the unloaded quality factor was performed. Then, a linear interpolation function of the ROOT software was used to obtain all the other Q_0 values between the fitted points, from the Q_L data acquired by the VNA. In Fig. 3.7 the correspondence between Q_0 and Q_L values is shown for the ZFC data of the TM₁₁₀ mode, along with the interpolation curve that allows to associate a Q_0 value for each Q_L . No uncertainties are associated to the experimental points on the (Q_0 vs Q_L) figure. The uncertainty on the single Q_L measurement should come from the VNA. However, as stated in Sec. 3.1.2, the instrument fails in the case of two, closely placed, interfering antennas. Thus the couplings κ_1 and κ_2 are not under control. Neither the Q_0 uncertainties are present in the figure, but have been added in the (Q_0 vs B) plots. See the next subsection (page 88) for their evaluation. From this Q_0 uncertainty analysis it is also seen that κ_1 and κ_2 are affected by large uncertainties, even 100%. However they don't limit the Q_0 determination, since Q_0 values are affected by uncertainties up to 10%. Note that knowing the uncertainties on Q_0 and κ_1 and κ_2 from the fit analysis, the uncertainty on the measured Q_L values can be propagated (see eq. (2.49)). Having an uncertainty on directly measured Q_L values can be useful for future cavity characterizations. Moreover, lower uncertainties on Q_0 and mostly on κ_1 and κ_2 (and thus on Q_L) could be achieved improving the sensitivity of the fit function to the data. In particular non-idealities can be added to the S_{11} curve, such as a frequency-dependent slope and a skewness.

The trend of Q_0 in dependence on B is the same as in the previous measurement (Fig. 3.5). The cavity remains in a Meissner state until $B \simeq 0.22$ T, then enters the mixed state and, at about 0.28 T, flux flow begins. From the detail of Fig. 3.6b it is

evident the deviation of the FC curve from ZFC curve, at $B \simeq 0.285$ T. In the region 0.24 T $< B < 0.275$ T this Nb cavity shows a flux pinning independent of the applied field. This is probably due to a different loss mechanism dominating in this region.

From the detail of Fig. 3.6b we also see that the data approaching $B = 0.5$ T is almost flat, and this indicates that the superconductor is almost in the normal state. Although the critical magnetic field B_{c2} cannot be determined by these data, we stress without the claim of being precise that B_{c2} of this Nb cavity is situated between 0.5 T and 0.6 T. Instead, the critical magnetic field B_{c1} can be taken to be approximately $B_{c1} \approx 0.22$ T, the field value after which the Meissner state seems to end.

Note that, from an applicative point of view, a strong pinning in a superconductor prevents it from dissipating energy inhibiting the flux flow, and this implies that quality factors are maintained high even with applied magnetic fields. Although the Q_0 values of the FC curve for $B \lesssim 0.24$ T are much smaller than ZFC values, this Nb cavity seems not to have a strong pinning, because flux flow begins soon after the transition from the Meissner to the mixed state. In any case, a Nb cavity is not suitable for the QUAX detection technique exploiting magnetized media. From eq. (2.7) we see that the search for an axion with mass $m_a \simeq 58$ μ eV would require a magnetizing field $B \simeq 0.5$ T, that is very close to the critical field B_{c2} of this Niobium cavity. Working with magnetic fields $B < 0.5$ T would also limit the axion-photon coupling and the signal power associated with it, that depends quadratically on B (eq. (2.79)).

Uncertainties of the Q_0 determination

In this paragraph the procedure to assign an uncertainty to the Q_0 extracted values is described. From Fig. 3.6a it is seen that the ZFC curve can be divided into three regimes, as described above, and the Q_0 values in these regions have different error bars. This is justified by the fact that for high Q_0 values ($\sim 10^6$) the bandwidth is very narrow, and then the S_{11} curve is only slightly affected by a slope due to frequency-dependent attenuation or by cross-coupling between antennas. It follows that the fit is more accurate in this region. On the contrary, for lower Q_0 values ($\lesssim 10^5$) the S_{11} curve is more affected by the aforementioned distortions, and it deviates from the ideal shape shown in Fig. 3.1a. Figure 3.8 shows the comparison of the cases just described. On the other hand, the S_{21} data are always well fitted, thanks to the more elaborate fit function employed for S_{21} (see Sec. 3.1.2).

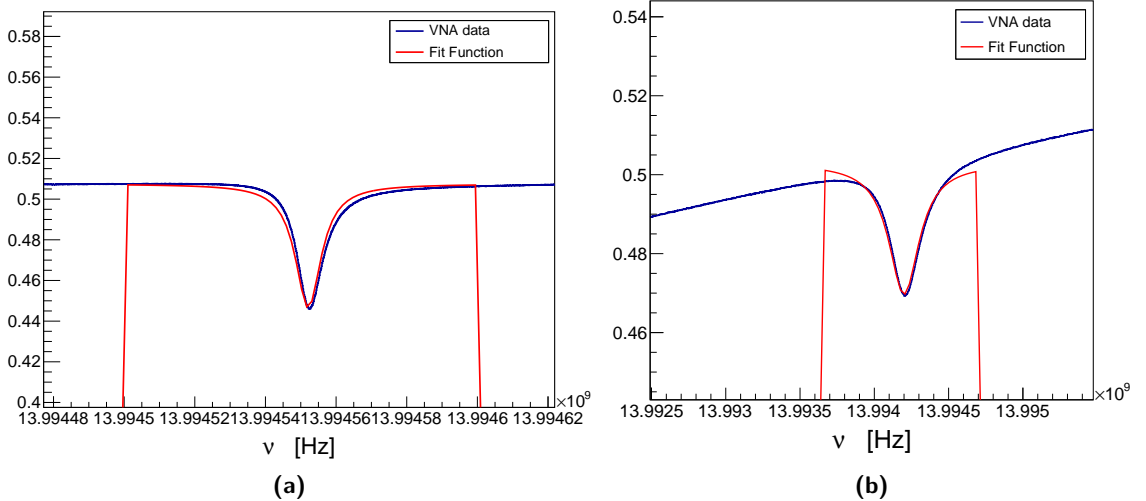


Figure 3.8: (a): S_{11} curve for $B = 0.22$ T with the fitting function (in red); the quality factor here is $Q_0 \simeq 1.47 \cdot 10^6$. The plateau of the curve assumes the same values before and after the resonance. (b): S_{11} curve for $B = 0.5$ T and fitting function; $Q_0 \simeq 5.93 \cdot 10^4$. The plateau is distorted by the sinusoidal modulation due to spurious reflections in the cables.

The Q_0 error bars are assigned by taking the waveforms (Fig. 3.8) of the fitted points of each region (the star black points in Fig. 3.6) and repeating the fit procedure varying the frequency range of the S_{11} fit for each point. The Q_0 values obtained are mediated, and a percentage error is assigned as:

$$\sigma_Q = \frac{\delta Q}{\bar{Q}_0} = \frac{Q_{\max} - Q_{\min}}{2\bar{Q}_0}, \quad (3.10)$$

where δQ is the semi-difference of the Q_0 values obtained by repeating the fit, and \bar{Q}_0 is the mean of that values. After this analysis, the uncertainties given for the ZFC data in

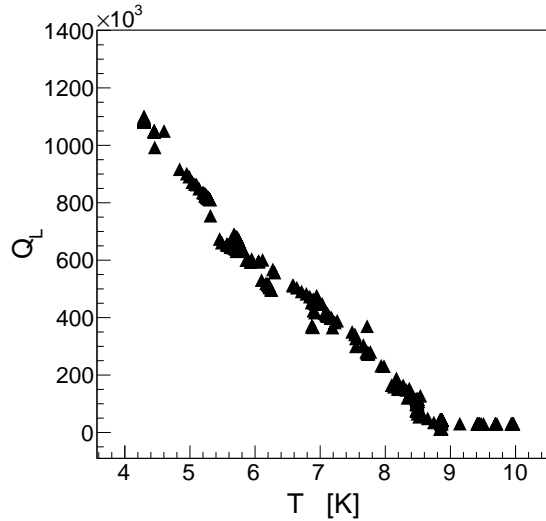


Figure 3.9: Temperature dependence of the loaded quality factor of TM_{110} mode of Niobium, from $T = 4.3$ K to $T = 10$ K, with $B = 0$ T. The transition from superconducting to normal state occurs at $T_c \simeq 9$ K. The errors on the temperature are negligible, while the error bars of Q_L are not present, see the discussion in the text.

the three regions are:

- $\sigma_Q = 1\%$ in the range $0 \text{ T} \leq B \leq 0.22 \text{ T}$;
- $\sigma_Q = 8\%$ in the range $0.22 \text{ T} < B \leq 0.25 \text{ T}$, where the transition occurs;
- $\sigma_Q = 8\%$ in the range $0.25 \text{ T} < B \leq 0.5 \text{ T}$.

The uncertainties assigned at FC data for $B < 0.24$, where the trapped field is present, are the same as for $B > 0.25$ (8%).

The fit procedure described in Sec. 3.1.2, however, can be further improved by parametrizing the S_{11} curve with non-idealities. These can be, for example, a slope and a skewness that add to the ideal S_{11} shape.

Temperature dependence. The temperature dependence of the loaded quality factors of the samples was also studied. For the Niobium cavity this dependence at $B = 0$ T is plotted in Fig. 3.9: Q_L decreases quite linearly as the temperature increases and then a plateau is reached. The temperature value at which this occurs can be taken as the critical temperature, denoting the transition from the superconducting to the normal state. Fig 3.9 is taken for the TM_{110} studied mode with $B = 0$ T, and the critical temperature is found to be about $T_c \simeq 9$ K, while the plateau has a value of $Q_L \approx 30000$. However, since B and T are two thermodynamically coupled quantities for superconductors, if a magnetic field is applied the critical temperature results lowered.

The plot also points out the importance of keeping the temperature constant during an experiment involving magnetic fields applied to superconducting microwave cavities, because superconducting losses are strongly dependent on temperature. Finally, the temperature dependence of Q_L for Niobium suggests that, at least with $B = 0$ T, going to lower temperatures (e.g. hundreds of mK) could improve the quality factor.

3.2.2 Niobium-Titanium resonant cavities

We have seen that a Niobium cavity can't be used for the QUAX goals, since it has a small critical magnetic field B_{c2} compared to the magnetic field necessary to polarize a magnetic sample ($B \simeq 0.5$ T to search for a mass $m_a = 58$ μeV). Thus we need a superconductor with higher B_{c2} . Niobium-Titanium meets this constraint (see Tab. 3.1), which makes it a good candidate to be used for QUAX cavities. Furthermore, the resistive losses decrease with B_{c2} , because the surface resistance is proportional to the resistivity, $R_s \propto \rho$, and in the Bardeen-Stephen model (Sec. 2.2.2) the resistivity in the flux flow regime is $\rho_f = \rho_n B / B_{c2}$. Two types of NbTi cavities were studied: a simple Niobium-Titanium cavity and a Niobium-Titanium cavity contaminated with nitrogen, $\text{NbTiN}_{x<1}$ ($x < 1$ indicates a non stoichiometric ratio).

Manufacturing of NbTi cavities. Both the Niobium-Titanium Nitride cavity and the Niobium-Titanium cavity were manufactured in the same way⁴. The superconducting film has been deposited on two copper semi-cells, constituting the two halves of the cavity, with a sputtering technique. The thickness of the film is about $(3 \div 4)$ μm . The semi-cells are shown in the picture of Fig. 3.10, where the NbTi film is recognized by the silvery color region. From the figure the unusual shape of the cavity is also evident. This was not designed as a simple cylinder. The substrate on which the NbTi film is deposited has a cylindrical form, but the edges of the cylinder are ended with conic-shaped regions. From a field point of view, the absence of two lids that close the cylinder doesn't affect the electromagnetic cavity modes. In fact, in the conic region the radius decreases continuously and correspondingly the cutoff frequency of both TE and TM modes becomes higher (from eq. 2.77 f_c depends on the inverse of the radius). Here, then, the modes become evanescent and cannot propagate, and this is equivalent to have metallic lids at the edges of the cylinder-shaped region. The absence of the lids also allows to reduce resistive losses, thus increasing the quality factor with respect to a cavity closed with conducting lids at both edges. The antennas enter the cavity from two bores made in one of the conic regions.

Actually the main volume is not perfectly cylindrical, but has two diametrically opposite convexities with the function of splitting the frequency of degenerate resonant modes, allowing to separately resolve them. In fact the convexities spoil the cylindrical symme-

⁴These cavities were manufactured at LNL.

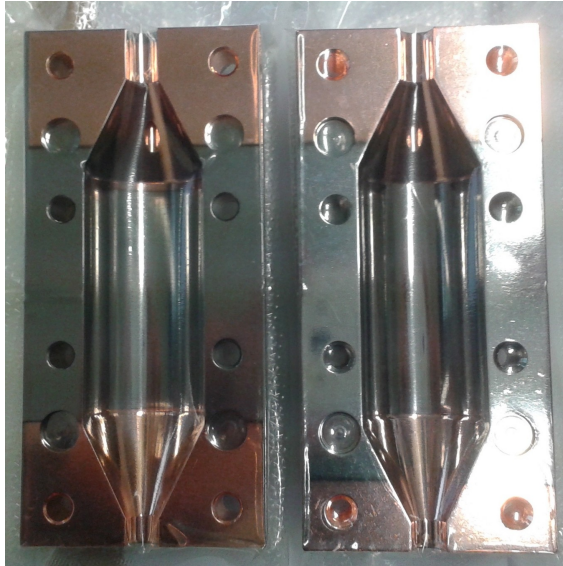


Figure 3.10: The two NbTi semi-cells that constitute the two halves of the cavity. The silvery color indicates the presence of a NbTi film, sputtered only on the cylindrical volume. The substrate on which the NbTi is sputtered is made of copper.

try that makes two modes degenerate. One of the convexities is depicted in the cavity simulations of Fig. 3.14.

Niobium-Titanium cavity

Three resonant modes were taken into account for the NbTi cavity: a TM_{010} mode, that thanks to its field configuration is useful to the detection of axions via the Primakoff effect (see Sec. 2.3), and two TM_{110} useful to the QUAX detection technique exploiting magnetized media. The TM_{110} resonant modes are not degenerate, but indeed they have different resonant frequencies because of the presence of the convexities. In the following the results for these modes are presented.

TM₀₁₀ mode. This mode was found at frequency $\nu_0 = 9.114$ GHz. The same analysis was carried out as for the Niobium cavity. The Q_0 dependence on the applied field B is shown in Fig. 3.11. The highest Q_0 value obtained is about $1.2 \cdot 10^6$ and the smallest value, at $B = 5$ T, is about $2.67 \cdot 10^5$. This curve is quite different from that for Niobium, because we cannot see the Meissner regime and the point where fluxons start to penetrate, but rather the Niobium-Titanium presents immediately a decaying trend. This is because NbTi has a very small critical field B_{c1} , that cannot be determined with our precision grade, and the sample is in a flux flow regime already with small magnetic fields applied to it. Performing the FC measurements, it is found that trapped magnetic field is present below a magnetic field of about $B \lesssim 0.7$ T, and at $B = 0$ T FC and ZFC curves don't

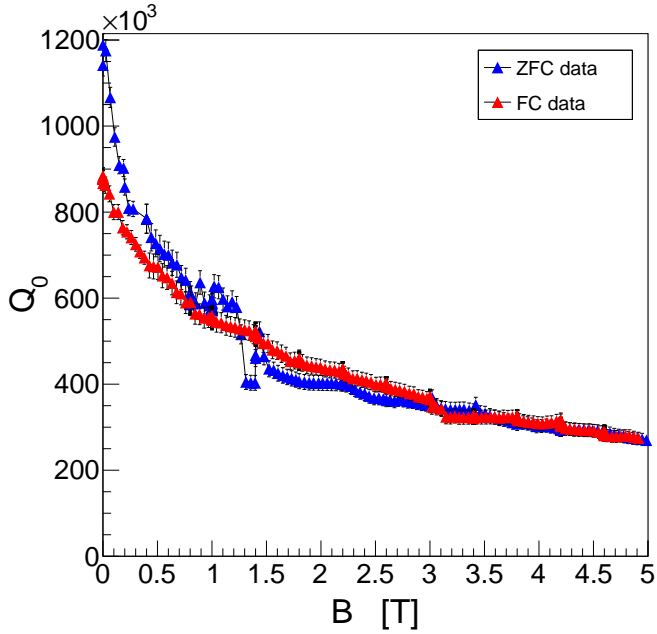


Figure 3.11: Unloaded quality factor of the TM_{010} mode of NbTi with resonant frequency $\nu_0 = 9.114$ GHz, at $T = 4.2$ K. The magnetic field is varied in the range $0 \text{ T} \leq B \leq 5 \text{ T}$. Blue data correspond to ZFC measurements, while the FC points are plotted in red.

show great differences. This could indicate that this material has not a strong pinning, because the magnetic field can be expelled through the cuts that divide the two half-cells of the cavity.

To assign the uncertainties on Q_0 , the (Q_0 vs B) plot was divided in three regions, one between $0 \text{ T} \leq B \leq 0.4 \text{ T}$, where the curve has a high slope, one between $0.4 \text{ T} < B \leq 3 \text{ T}$ and the last one between $3 \text{ T} < B \leq 5 \text{ T}$. The uncertainties are:

- $\sigma_Q = 2\%$ in the range $0 \text{ T} \leq B \leq 0.4 \text{ T}$;
- $\sigma_Q = 4\%$ in the range $0.4 \text{ T} < B \leq 3 \text{ T}$;
- $\sigma_Q = 5\%$ in the range $3 \text{ T} < B \leq 5 \text{ T}$.

The measured values of Q_0 for NbTi are interesting if compared with the quality factor of copper, that is the most common material employed in the manufacturing of resonant cavities. A copper cavity was available at the beginning of the QUAX R&D, but only the TM_{110} mode at $\nu_0 \simeq 14$ GHz was measured. From simulations with ANSIS-HFSS the unloaded quality factor of the copper cavity at $\nu_0 \simeq 9$ GHz is found to be $Q_0 \simeq 80\,000$. It follows that the ratios of the NbTi quality factor on the copper quality factor for the TM_{010} mode are, at $B = 0 \text{ T}$ and $B = 5 \text{ T}$, respectively:

$$\frac{Q_0(\text{NbTi})}{Q_0(\text{Cu})} \Big|_{0 \text{ T}} \simeq 14.7, \quad \frac{Q_0(\text{NbTi})}{Q_0(\text{Cu})} \Big|_{5 \text{ T}} \simeq 3.34. \quad (3.11)$$

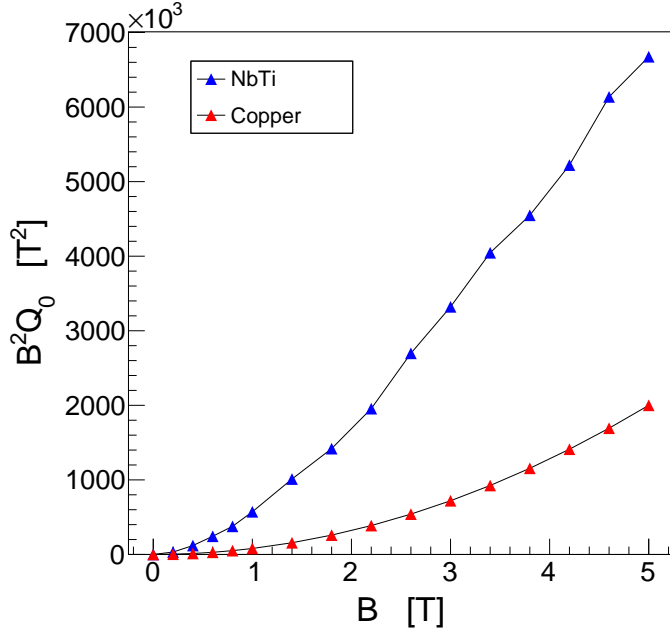


Figure 3.12: The plot shows the $Q_0 B^2$ quantity in dependence on B for the TM_{010} mode of NbTi at $\nu_0 = 9.114$ GHz (blue data) and copper at $\nu_0 \simeq 9$ GHz (red data). This quantity enters the expression of the power emitted in photons after an axion-photon interaction. In the NbTi data the error bars are covered by the markers. They are simply evaluated by the uncertainty propagation, having assigned $\sigma_B = 0.001$ T, that is the magnetic field resolution.

Now, the power emitted in photons after the interaction of axions with the static magnetic field in a conventional haloscope (eq. 2.17) is proportional to:

$$P_{\text{sig}} \propto \alpha(\text{axions}) B^2 Q_0, \quad (3.12)$$

where $\alpha(\text{axions})$ contains all the model-dependent axion parameters. B and Q_0 are parameters of the experiment, so the quantity $B^2 Q_0$ can be governed, and the signal power can be enhanced choosing the right material for a resonant cavity. Fig. 3.12 shows the quantity $Q_0 B^2$ for Niobium-Titanium (blue points) and copper (red points). The ratio of this quantity for NbTi and copper at $B = 5$ T is equal to their quality factor ratios:

$$\left. \frac{B^2 Q_0(\text{NbTi})}{B^2 Q_0(\text{Cu})} \right|_{5 \text{ T}} \simeq 3.34. \quad (3.13)$$

This is an unprecedented result and it follows that the sensitivity of a conventional axion haloscope involving NbTi resonant cavities can be enhanced by a factor of 3.34 with respect to a copper cavity. Moreover, this result is also significant from a technological and economical point of view, because it implies that working with NbTi at $B = 5$ T is equivalent to work with a copper cavity at $B = 9$ T, where the same $Q_0 B^2$ value is

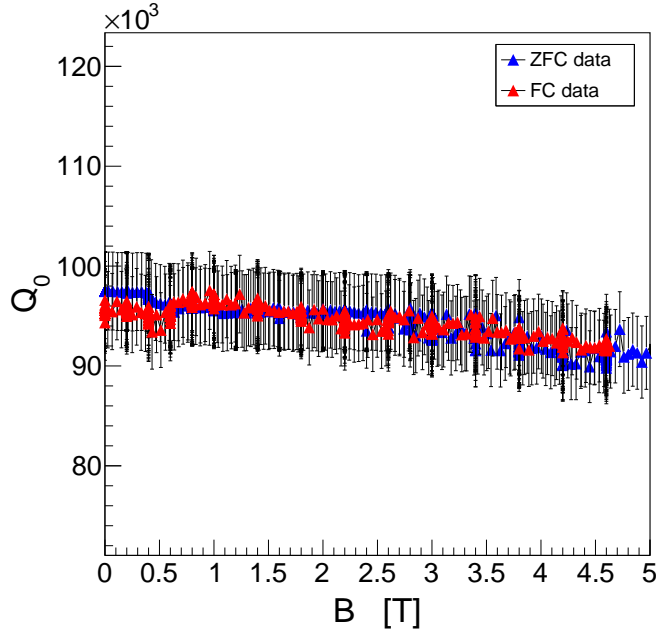


Figure 3.13: Unloaded quality factor of the TM_{110} mode of NbTi with resonant frequency $\nu_0 = 14.266 \text{ GHz}$, at $T = 4.2 \text{ K}$. The magnetic field is varied in the range $0 \text{ T} \leq B \leq 5 \text{ T}$. Blue data correspond to ZFC measurements, while the FC points are plotted in red.

reached. This follows if we equate the two quantities:

$$\begin{aligned} Q_0(\text{NbTi}) B_{\text{NbTi}}^2|_{5 \text{ T}} &= Q_0(\text{Cu}) B_{\text{Cu}}^2|_{x \text{ T}} \\ \Rightarrow B_{\text{Cu}} &= (5 \text{ T}) \sqrt{\frac{Q_0(\text{NbTi})|_{5 \text{ T}}}{Q_0(\text{Cu})}} \simeq 9 \text{ T}, \end{aligned} \quad (3.14)$$

where the constant value of $Q_0(\text{Cu}) = 80000$ was used.

TM₁₁₀ mode. The first TM₁₁₀ resonant mode of the NbTi cavity is found at $\nu_0 = 14.266 \text{ GHz}$, and its field configuration is depicted in Fig. 2.10. The electric field is concentrated in two lobes with opposite directions. It has been found that this mode is subject to a significant reduction of the Q_0 values, with respect to the expected ones of order $\mathcal{O}(10^6)$ for small magnetic fields. From Fig. 3.13 we see that both ZFC and FC Q_0 data vary within the values $9.7 \cdot 10^4$ and $9.0 \cdot 10^4$. The same data analysis was repeated as for the previous TM₀₁₀ mode, and the same uncertainty was assigned to all the data:

- $\sigma_Q = 4\%$ in the range $0 \text{ T} \leq B \leq 5 \text{ T}$;

The simulations of the current density of this mode help to understand the low quality factor measured, or high losses. Fig. 3.14 shows a comparison of the current density in the TM₀₁₀ (Fig. 3.14a) mode and in the TM₁₁₀ mode (Fig. 3.14b). For the TM₀₁₀ mode we

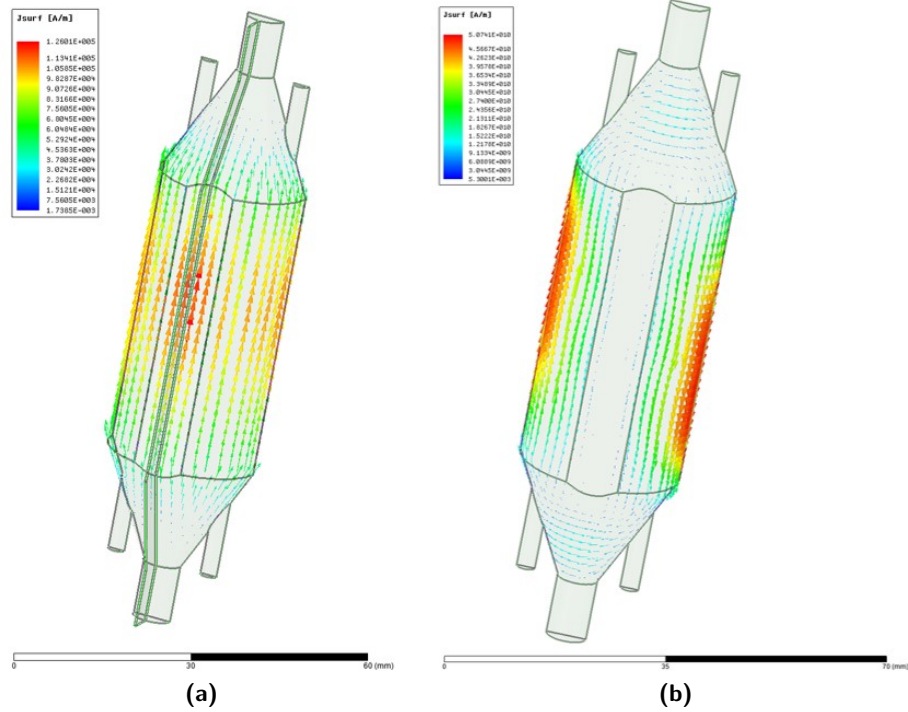


Figure 3.14: (a): The simulation shows the current density flowing on the cavity walls for the TM_{010} mode. For simplicity only half a cavity is shown. The actual side where the cavity is cut (see Fig. 3.10) is indicated here by the plane passing through the convexity. The current indicated by red arrows is more intense. The currents flow parallel to the cavity axis and are not interrupted by the cavity cut. (b): This simulation shows the current density of the TM_{110} mode at $\nu_0 = 14.266$ GHz. Here the currents form two loops (one showed here and one on the other side), and they close in the conic regions, where they flow perpendicular to the cut plane. They are thus interrupted, causing additional RF losses.

see that the currents flow parallel to the cavity axis, and so they cannot be interrupted by the cavity cut (represented by the plane parallel to the cavity axis and passing through the convexity). For the TM_{110} mode the currents form two loops (only one is showed in the picture), and they close in the conic copper regions, where they flow perpendicular to the cut plane. They are therefore interrupted, and this causes a significant reduction of the quality factor.

Reversed TM_{110} mode. This is the second TM_{110} mode appearing in the cavity, at a frequency $\nu_0 = 14.464$ GHz. In a cylindrical resonant cavity there exists a certain number of degenerate TM_{nml} modes for each n index. They are degenerate because they correspond to rotated field configurations with the same resonant frequency. This follows from the solution of the TM modes in the cavity, given in eq. (A.21). The $\cos n\phi$ and $\sin n\phi$ terms, on which the fields depend, are independent solutions, thus can be both excited yielding to degenerate modes. In this case, with $n = 1$, two degenerate modes would exist

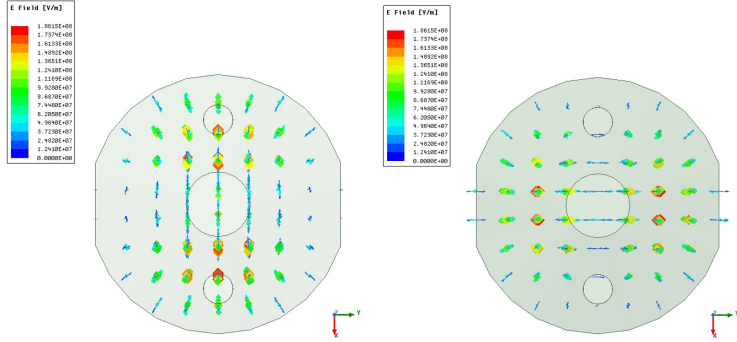


Figure 3.15: Section of the NbTi cavity showing the electric field lines of TM_{110} modes. On the left the electric field of TM_{110} mode at $\nu_0 = 14.266 \text{ GHz}$ is shown, while on the right there is the 90° rotated electric field of TM_{110} at $\nu_0 = 14.464 \text{ GHz}$. The two lobes can be recognized from the color code: red arrows indicate more intense fields.

if the cavity section were perfectly circular. The two convexities break the cylindrical symmetry and shift the frequency of one of the degenerate modes at $\nu_0 = 14.464 \text{ GHz}$. Fig. 3.15 shows a simulation of the two TM_{110} modes for this geometry. It can be seen that the orientations of the electric field lobes are 90° rotated with respect to each other.

The Q_0 variation with an applied magnetic field B is reported in Fig. 3.16a. The maximum value obtained is $Q_0 \simeq 1.5 \cdot 10^6$ and the minimum (at $B = 5 \text{ T}$) is $Q_0 \simeq 2.3 \cdot 10^5$. The trend is very similar to that for the TM_{010} mode (see Fig. 3.11), also regarding the small difference between the ZFC and FC values at small B fields. For comparison, the value of Q_0 for the TM_{110} of the copper cavity (at frequency $\nu_0 \simeq 14 \text{ GHz}$) is about $6 \cdot 10^4$, thus at 5 T we gain in this case a factor of 3.83 with the NbTi cavity. The uncertainties given to the Q_0 data are:

- $\sigma_Q = 10\%$ in the range $0 \text{ T} \leq B \leq 2 \text{ T}$;
- $\sigma_Q = 4\%$ in the range $2 \text{ T} < B \leq 5 \text{ T}$.

Note that in this case higher Q_0 values are less precise.

As shown, the Q_0 values obtained are again high for this mode. This is because the RF currents do not cross the cavity cut and are not interrupted, since the current loops are 90° rotated with respect to the previous TM_{110} mode loops of Fig. 3.14b. Therefore this proves that the previous TM_{110} mode at $\nu_0 = 14.266 \text{ GHz}$ suffers from RF losses due to the presence of a cavity cut (in that case the currents are interrupted by the cut). On the contrary, the reversed TM_{110} mode at $\nu_0 = 14.464 \text{ GHz}$ is reliable for the QUAX detection scheme exploiting axion-electron interactions.

To conclude this paragraph note that the cavity decay time, already defined as $\tau_c = Q_0/\omega_0$, for resonant modes having $Q_0 \sim 10^6$ and for frequencies $\nu_0 \simeq 14 \text{ GHz}$ takes values:

$$\tau_c = \frac{Q_0}{\omega_0} \approx 10 \text{ } \mu\text{s}. \quad (3.15)$$

Performing the same calculation at $B = 2$ T, where the reversed TM₁₁₀ mode has $Q_0 \approx 5 \cdot 10^5$, yields the value $\tau_c \approx 5 \mu\text{s}$. These values are large compared to the spin relaxation time, $\tau_2 \simeq 0.11 \mu\text{s}$ [43], entering the expression of τ_{\min} in the signal power of the axion-electron coupling (eq. (2.80)). This means that the signal power is only limited by the relaxation time of magnetized materials, while τ_c is not limiting in the axion search through axion-electron detection.

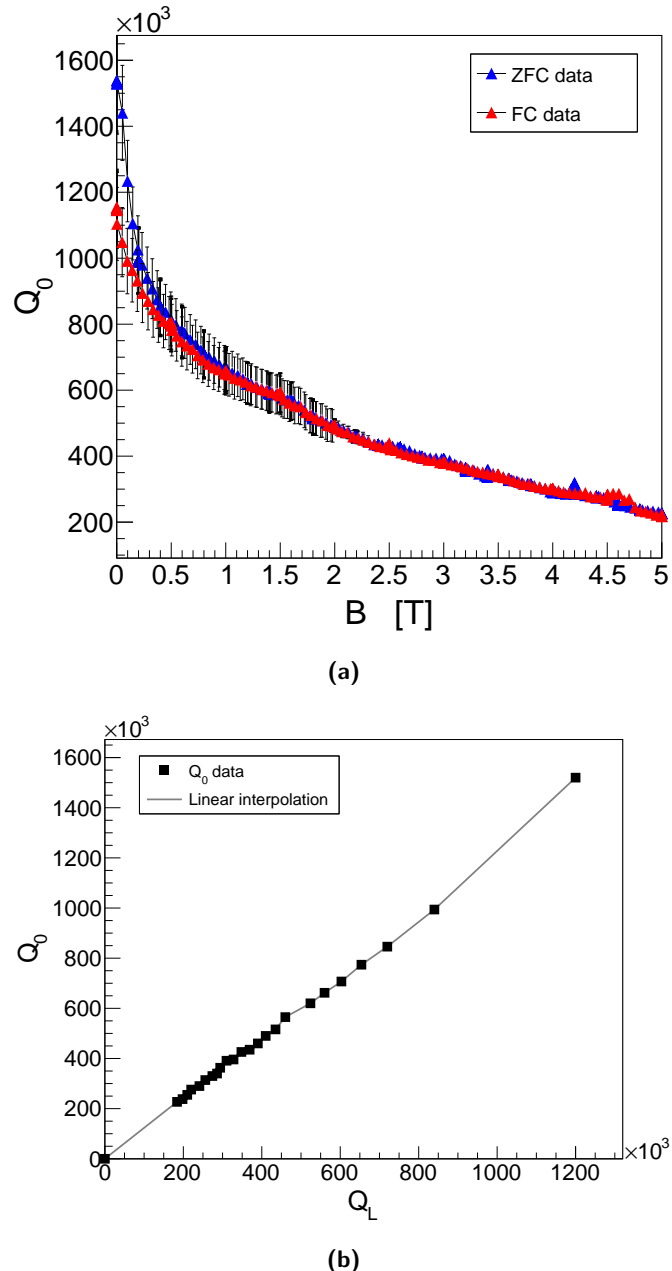


Figure 3.16: (a): Unloaded quality factor of the reversed TM₁₁₀ mode of NbTi with resonant frequency $\nu_0 = 14.464$ GHz, at $T = 4.2$ K. The magnetic field is varied in the range $0 \text{ T} \leq B \leq 5 \text{ T}$. Blue data correspond to ZFC measurements, while the FC points are plotted in red. (b): The correspondence between Q_L values and interpolated Q_0 values. The black squares are the fitted data and the line represents the interpolation function. The Q_L errors are not present, due to experimental difficulties, see the comment to Fig. 3.7 in the text of Sec. 3.2.1. Q_0 uncertainties are only reported in the (Q_0 vs B) plots.

Temperature dependence. In Fig. 3.17 the $Q_L(T)$ dependences at $B = 0$ T for all the three studied modes of NbTi are represented. The transition is seen at about $T_c \approx (7.8 \div 8.0)$ K, and we were able to measure the plateau only for the TM₀₁₀ mode (Fig. 3.17a), having a value of $Q_L \approx 180$. The $Q_L(T)$ curves for TM₀₁₀ and reversed TM₁₁₀ modes (Fig.s 3.17a and 3.17b respectively) seem to have almost a linear dependence on temperature, while the same curve for the first TM₁₁₀ mode (Fig. 3.17c) is saturated for $T \lesssim 6$ K and then sharply decrease. This is probably due to the fact that for Q_L values above $\approx 70\,000$ the dominating losses are due to RF field exiting from the cut of the half-cells.

Fig. 3.18 shows the comparison of the temperature dependences of Q_L for the reversed TM₁₁₀ mode at different values of the applied B field. For values up to $B = 3$ T (red points) data seem to show a good linear dependence from T_c to $T = 4$ K, while at $B = 5$ T (green points) data start to saturate at low temperatures. This is important from the point of view of the design of a possible future set-up. In fact, in the case that lower temperatures are reached (for example ~ 100 mK, the temperature of operation of a Josephson Parametric Amplifier) we could improve the cavity quality factor. This is true for the reversed TM₁₁₀ mode with an applied field $0 \text{ T} < B < 3$ T, values needed to magnetize the media in the QUAX set-up exploiting axion-electron spin interaction.

From Fig. 3.18 it can also be noted that the critical temperature T_c decreases if a magnetic field is applied. For example with $B = 3$ T (red data) it is $T_c \approx 7.2$ K, while at 0 T (black data) it is $T_c \approx (7.8 \div 8.0)$ K, as seen before (Fig. 3.17).

Niobium-Titanium Nitride cavity

The NbTiN has a higher critical temperature with respect to Nb and NbTi ($T_c \simeq 12.6$ K in our case). This could result in an improvement of the quality factor at 4.2 K. On the other hand, the nitriding process introduces contaminating defects in the NbTi that could improve the surface resistance, lowering the Q_0 .

The only resonant mode that has been studied for the NbTiN cavity is the reversed TM₁₁₀ mode at resonant frequency $\nu_0 = 14.461$ GHz, because of the impossibility to find the other modes of interest (TM₀₁₀ and TM₁₁₀ at $\nu_0 = 14.266$ GHz). In Figure 3.19 the (Q_0 vs B) curve is plotted. The highest Q_0 value that has been measured is about $Q_0 \simeq 6.5 \cdot 10^5$, while the smallest is $Q_0 \simeq 6.4 \cdot 10^4$. The trend is quite regular, apart the step found at $B \simeq 0.9$ T in the ZFC data. This is due to the fact that the depth of the antennas was strongly changed because, as the magnetic field was increased, the couplings κ_1 and κ_2 became increasingly smaller. Thus they were inserted more deeply. In correspondence of this operation the extracted Q_0 emerges with lower values, and then this means that the fit procedure failed in solving the bias. The FC data match the ZFC data when turning off the magnetic field until the value $B \simeq 0.9$ T is reached, where the

FC curve deviates from the ZFC curve.

The uncertainties given to the Q_0 values are:

- $\sigma_Q = 4\%$ in the range $0 \text{ T} \leq B \leq 2 \text{ T}$;
- $\sigma_Q = 3\%$ in the range $2 \text{ T} < B \leq 5 \text{ T}$.

To conclude, the contamination with nitrogen has not introduced improvements towards higher quality factors.

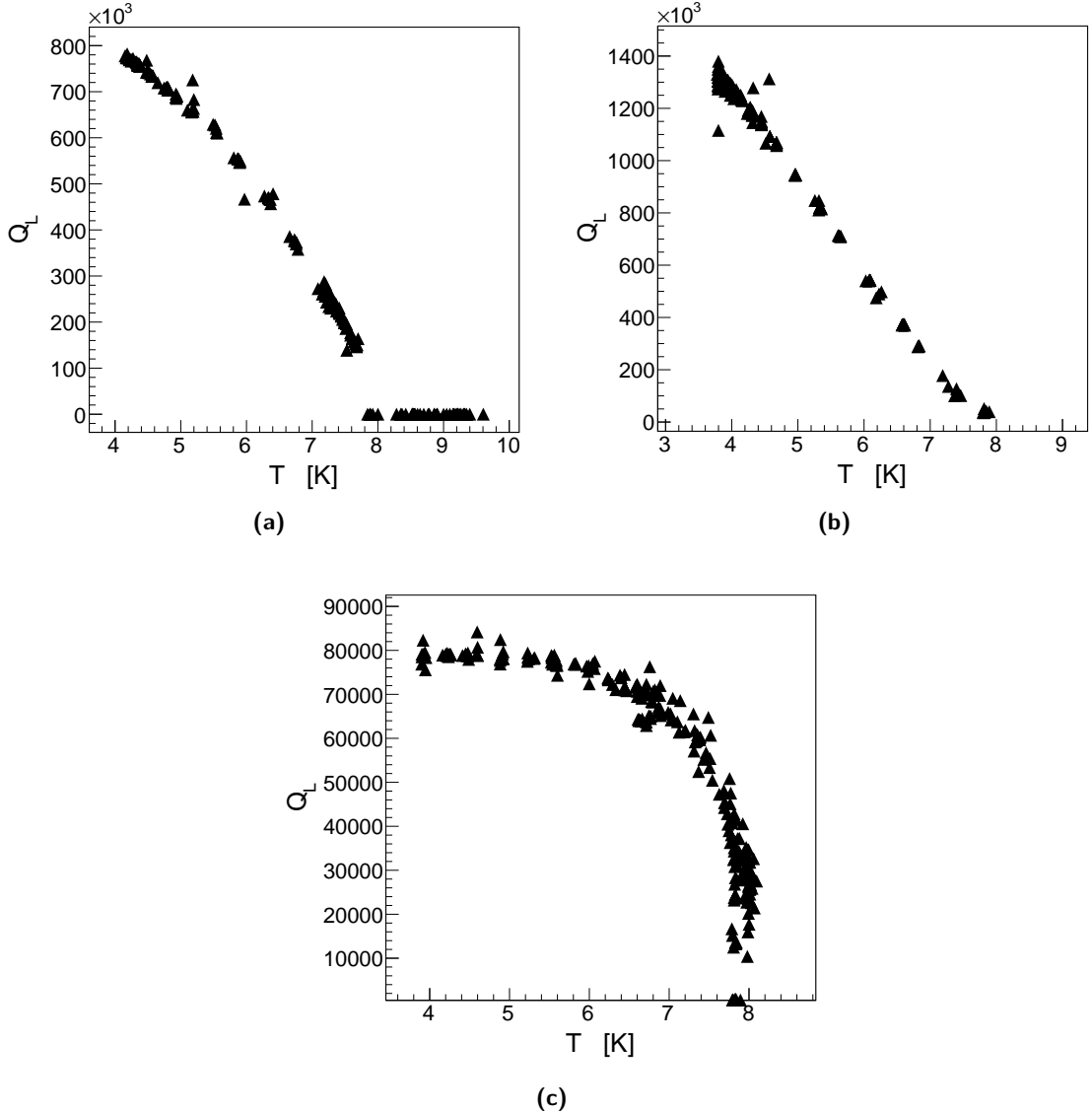


Figure 3.17: (a): Temperature dependence of Q_L for the TM_{010} mode of NbTi at $B = 0$ T. (b): Temperature dependence of Q_L for the reversed TM_{110} mode of NbTi at $B = 0$ T. (c): Temperature dependence of Q_L for the first TM_{110} mode of NbTi at $B = 0$ T. From the curves we see that the transition occurs approximately at $T_c \approx (7.8 \div 8.0)$ K. The errors on the temperature are negligible, while the Q_L errors are not present, see the comment to Fig. 3.7 in the text of Sec. 3.2.1.

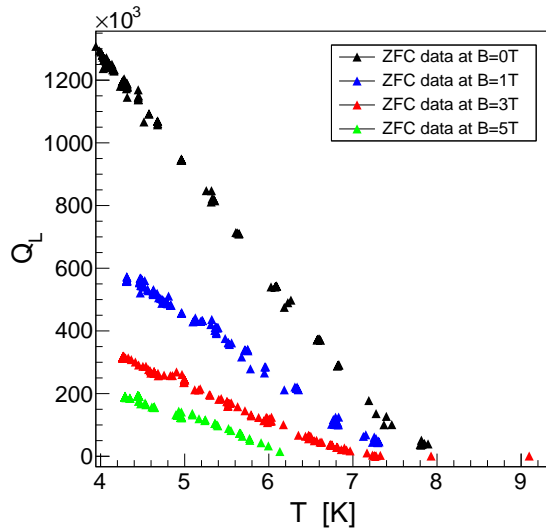


Figure 3.18: Comparison of the temperature dependences of Q_L for the reversed TM_{110} mode at different values of applied B field. In black the data at $B = 0$ T are shown, blue is relative to $B = 1$ T data, red is used for $B = 3$ T and green for $B = 5$ T. The errors on the temperature are negligible, while the Q_L errors are not present, see the comment to Fig. 3.7 in the text of Sec. 3.2.1.

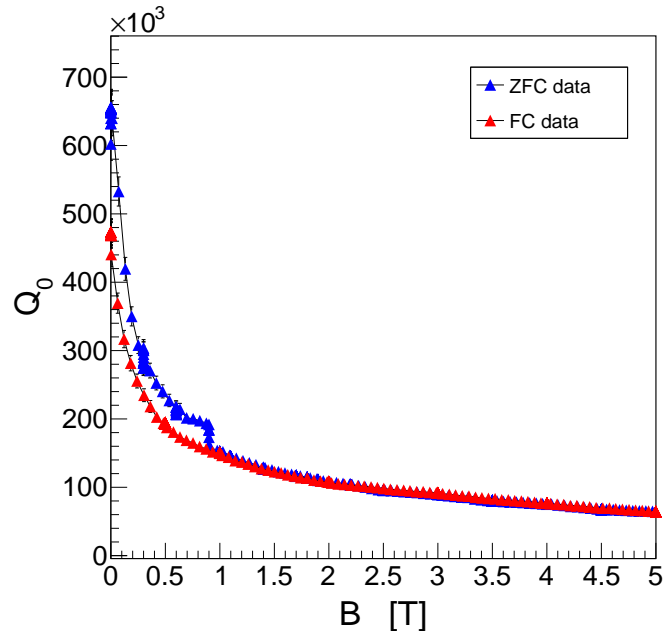


Figure 3.19: Unloaded quality factor of the reversed TM_{110} mode of NbTiN with resonant frequency $\nu_0 = 14.461$ GHz, at $T = 4.2$ K. The magnetic field is varied in the range $0 \text{ T} \leq B \leq 5$ T. Blue data correspond to ZFC measurements, while the FC points are plotted in red.

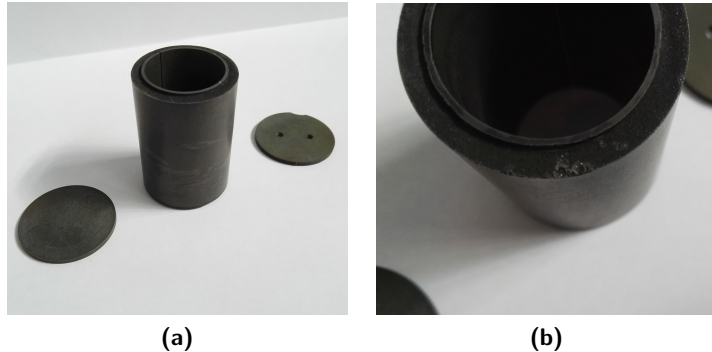


Figure 3.20: (a): The Magnesium Diboride bulk cavity, with the two lids of the same material. One of the lids is provided with two bores for the antennas. (b): A detail of the MgB₂ cavity after the first test. One of the edges is ruined, and this probably causes RF losses.

3.2.3 Magnesium Diboride cavity

MgB₂ is a High-Temperature Superconductor (HTS) (i.e. with high T_c). It was chosen for two main reasons: it has a quite high critical field ($B_{c2} \approx 15$ T [59]), and from the measurements reported in Ref. [60] it is seen that the resistivity has a linear dependence on the magnetic field, $\rho_f \propto B/B_{c2}$.

The MgB₂ cavity (Fig. 3.20a) was manufactured by the authors of Ref. [61] with a technique consisting in a reaction of B₂ powder and pure liquid Magnesium (see [61] and ref.s therein). This cavity has a cylindrical shape, thus the TM₁₁₀ modes are degenerate. Also the lids are made of MgB₂.

A first measurement at temperature $T = 4.3$ K was performed with this MgB₂ cavity. According to Ref. [61], the expected quality factor was $Q_0 \sim \text{few} \cdot 10^5$, but our cavity shows Q_L values not higher than 7500 for both the two modes of interest, that are TM₀₁₀ at $\nu_0 \simeq 8.8$ GHz and TM₁₁₀ at $\nu_0 \simeq 14.02$ GHz. This is probably due to the fact that the cavity edges were ruined when pressing the lids to the cylindrical body, as shown in the detail of Fig. 3.20b. This could cause RF losses and limit the quality factor. As a next step it was suggested to add two copper rings, although it is not superconducting, to ensure a better electric contact between the body and the lids. Then a further test will be executed.

However, it was proved that the superconducting state of MgB₂ is reached and is effective. In fact the measured Q_L values in dependence on temperature of Fig. 3.21 clearly show a transition. The critical temperature is estimated to be $T_c \approx 38$ K, before which the loaded quality factor is higher than the constant value of $Q_L \simeq 2000$ of the normal state (after T_c), and it shows a growing trend as the temperature decreases.

Table 3.2 summarizes the obtained results concerning the quality factors of the four cavi-

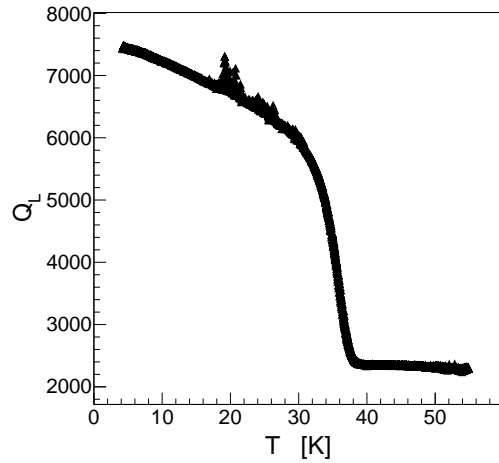


Figure 3.21: Loaded quality factor versus temperature of the MgB_2 cavity, from $T = 4.3$ K to $T = 55$ K, with $B = 0$ T. The transition from superconducting to normal state happens at $T_c \simeq 38$ K, after which the quality factor reaches a constant value. At about 20 K the Q_L values measured by the VNA present some fluctuations. The errors on the temperature are negligible, while the error bars of Q_L are not present, see the discussion in Sec. 3.2.1.

ties.

Table 3.2: Summary of the results obtained concerning quality factors. rTM₁₁₀ refers to the reversed TM₁₁₀ and pertains only to NbTi and NbTiN cavities.

	mode	Nb	NbTi	NbTiN	MgB ₂
$Q_0(0\text{ T})$	TM ₀₁₀		$1.18 \cdot 10^6 (\pm 2\%)$		
	TM ₁₁₀	$1.78 \cdot 10^6 (\pm 1\%)$	$9.75 \cdot 10^4 (\pm 4\%)$		
	rTM ₁₁₀		$1.52 \cdot 10^6 (\pm 10\%)$	$6.55 \cdot 10^5 (\pm 4\%)$	
$Q_0(5\text{ T})$	TM ₀₁₀		$2.67 \cdot 10^5 (\pm 5\%)$		
	TM ₁₁₀		$9.1 \cdot 10^4 (\pm 4\%)$		
	rTM ₁₁₀		$2.27 \cdot 10^5 (\pm 4\%)$	$6.44 \cdot 10^4 (\pm 3\%)$	
$\frac{Q_0 B^2}{Q_0 B^2(\text{Cu})} _{5\text{ T}}$	TM ₀₁₀			3.34	
$Q_L(0\text{ T})$	TM ₀₁₀				≈ 7500
$\tau_c(2\text{ T}) [\mu\text{s}]$	rTM ₁₁₀			≈ 5	

Conclusion

I have conducted my thesis work in the characterization of superconducting microwave resonant cavities for their employment in the galactic axion detection with the QUAX experiment. Axions are well-motivated candidates of Dark Matter and have small couplings to Standard Model particles. The QUAX experiment aims at detecting axions exploiting their coupling with photons and interaction with the electron spin. The main challenge in the design of the QUAX experiment concerns finding a superconducting RF cavity with a high quality factor in the presence of magnetic fields, and finding a magnetized medium with large relaxation time. In particular, my thesis work has focused on the former.

Several materials, each with benefits and issues connected, were tested. The Niobium cavity showed very high unloaded quality factors (up to about $1.78 \cdot 10^6 \pm 1\%$), but for small applied magnetic fields ($B \lesssim 0.22$ T). However, the Nb cavity undergoes the transition from superconducting to normal state with relatively small fields, $B \sim (0.5 \div 0.6)$ T. Therefore it is not suitable to be used in the QUAX experiment.

With the Niobium-Titanium cavity, one of the goals of the QUAX R&D can be considered achieved: we found that this cavity maintains high enough quality factors without spoiling superconductivity in the presence of magnetic fields. In particular at $B = 5$ T the reversed TM_{110} mode has $Q_0 \simeq (2.3 \cdot 10^5 \pm 4\%)$, a factor of almost 4 with respect to a copper cavity. For the TM_{010} mode, instead, $Q_0 \simeq (2.67 \cdot 10^5 \pm 5\%)$ is reached at 5 T and this allows to gain a factor of 3.34 with respect to copper on the signal power of an experiment testing the axion-photon coupling. Moreover, the cavity decay time τ_c of this cavity is quite large, and is not limiting in the search for axions through the axion-electron coupling.

The Magnesium Diboride cavity was tested for the first time, and didn't present quality factors as high as expected, probably due to RF losses caused by a not perfect closure of

the cavity. In any case, we ensured that the superconducting state is reached.

Outlook. Regarding the immediate future of the QUAX R&D, further tests of the MgB₂ cavity will be performed. Next, the manufacturing of a new NbTi cavity has been ordered. The dimensions and the coating are the same as for the already measured cavities, but the cut that divides the two halves is designed to be 90° rotated with respect to the present configuration (see Fig. 3.14 for clarity). This will allow to properly characterize the TM₁₁₀ mode at $\nu_0 = 14.266$ GHz, because the currents won't be interrupted by the cut. Subsequently, QUAX R&D could continue to test other superconducting materials, as for example the YBCO (Yttrium Barium Copper Oxide) that is a High-Temperature Superconductor with $T_c \approx 90$ K and $B_{c2} \approx 150$ T.

An activity that has been approved at LNF is the development of a single photon counter, suitable for a proper detection of the tiny signal power coming from axion-electron or axion-photon interactions (see eq.s (2.13) and (2.19)). The INFN-project SIMP proposes two solutions for single microwave photon detection: a Current-Biased Josephson-Junction (JJ) and a Transition Edge Sensor (TES). JJ are the basic building blocks of superconducting qubits for quantum processors. Qubit-state readout is intimately connected with single photon detection. High efficiency is obtained by coupling the JJ with a planar microwave-resonator where the field confinement enhances the coupling to the junction. TES are already used as bolometers for the measurement of the Cosmic Microwave Background (CMB) and they proved single-photon sensitivity in the IR regime. Nanofabrication of the superconducting films and lowering of the critical temperature will allow the single photon detection in the microwave regime.

APPENDIX A

Resonant modes of a cylindrical cavity

In what follows I describe the field solutions in waveguides and then in cylindrical resonant cavities, following Refs. [44, 14]. It has been said that resonant cavities are volumes enclosed by conducting surfaces. Therefore the solution to their field modes can be found by solving Maxwell's equations in a waveguide and subsequently applying additional boundary conditions to account for the conducting plates short-circuiting both ends.

A waveguide is a conducting structure made of one or more conductors, in which electromagnetic waves can propagate. It can have any shape, as long as it has cylindrical symmetry, as in Fig. A.1. The axis is chosen to be that of the propagation direction \hat{z} . All TE, TM and TEM modes can propagate in a waveguide, but since we treat resonant cavities only TE and TM modes are considered here.

To begin one can write the electric and magnetic fields as a sum of transverse and

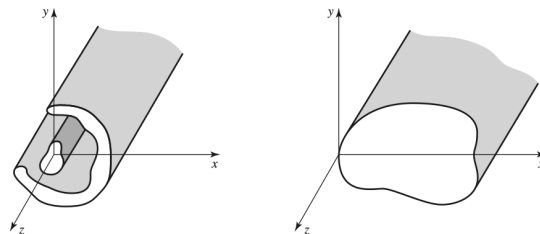


Figure A.1: Left: section of a waveguide made of two conductors; Right: section of a waveguide made of only one conductor. Taken from [44].

longitudinal components:

$$\begin{aligned}\mathbf{E}(x, y, z) &= [\mathbf{e}(x, y) + \hat{\mathbf{z}} e_z(x, y)] e^{-j\beta z}, \\ \mathbf{H}(x, y, z) &= [\mathbf{h}(x, y) + \hat{\mathbf{z}} h_z(x, y)] e^{-j\beta z},\end{aligned}\quad (\text{A.1})$$

where the phasor notation is used and an implicit $e^{j\omega t}$ time dependence is assumed. Here only the forward propagating wave is taken into account; a backward propagation is obtained summing the same components with $\beta \rightarrow -\beta$. The guide is supposed to be lossless. From the curl Maxwell's equations in the frequency domain, $\nabla \wedge \mathbf{E} = -j\omega\mu\mathbf{H}$ and $\nabla \wedge \mathbf{H} = j\omega\epsilon\mathbf{E}$, the transverse components of the fields can be written in terms of the z components:

$$E_x = \frac{-j}{k_c^2} \left(\beta \frac{\partial E_z}{\partial x} + \omega\mu \frac{\partial H_z}{\partial y} \right), \quad (\text{A.2a})$$

$$E_y = \frac{j}{k_c^2} \left(-\beta \frac{\partial E_z}{\partial y} + \omega\mu \frac{\partial H_z}{\partial x} \right), \quad (\text{A.2b})$$

$$H_x = \frac{j}{k_c^2} \left(\omega\epsilon \frac{\partial E_z}{\partial y} - \beta \frac{\partial H_z}{\partial x} \right), \quad (\text{A.2c})$$

$$H_y = \frac{-j}{k_c^2} \left(\omega\epsilon \frac{\partial E_z}{\partial x} + \beta \frac{\partial H_z}{\partial y} \right), \quad (\text{A.2d})$$

where ϵ and μ are the electric permittivity and magnetic permeability, respectively, of the medium that eventually fill the guide, β is the *propagation constant* appearing in the propagation factor $e^{-j\beta z}$, and k_c is the **cutoff wave number**, defined as:

$$k_c^2 = k^2 - \beta^2, \quad (\text{A.3})$$

and k is the wave number of the medium filling the guide: $k = \omega\sqrt{\mu\epsilon}$. The name *cutoff* will become clear later. Equations (A.2) can be solved when the components E_z and H_z are known. They can be found solving the Helmholtz wave equations (that derive from the two curl Maxwell's equations):

$$(\nabla^2 + k^2) E_z = \left(\frac{\partial^2}{\partial x^2} + \frac{\partial^2}{\partial y^2} + k_c^2 \right) e_z = 0, \quad (\text{A.4a})$$

$$(\nabla^2 + k^2) H_z = \left(\frac{\partial^2}{\partial x^2} + \frac{\partial^2}{\partial y^2} + k_c^2 \right) h_z = 0. \quad (\text{A.4b})$$

The first equality holds because $\frac{\partial^2 E_z}{\partial z^2} = -\beta^2 E_z$ and $k^2 - \beta^2 = k_c^2$, and the same for H_z . Now the solutions to the transverse fields are obtained imposing the field configurations of the various modes and the boundary conditions.

TE modes for circular waveguides

Here a cylindrical waveguide is taken into account, with cross-sectional radius a . Eq.s (A.2) are rewritten in cylindrical components:

$$E_\rho = \frac{-j}{k_c^2} \left(\beta \frac{\partial E_z}{\partial \rho} + \frac{\omega \mu}{\rho} \frac{\partial H_z}{\partial \phi} \right), \quad (\text{A.5a})$$

$$E_\phi = \frac{-j}{k_c^2} \left(\frac{\beta}{\rho} \frac{\partial E_z}{\partial \phi} - \omega \mu \frac{\partial H_z}{\partial \rho} \right), \quad (\text{A.5b})$$

$$H_\rho = \frac{j}{k_c^2} \left(\frac{\omega \epsilon}{\rho} \frac{\partial E_z}{\partial \phi} - \beta \frac{\partial H_z}{\partial \rho} \right), \quad (\text{A.5c})$$

$$H_\phi = \frac{-j}{k_c^2} \left(\omega \epsilon \frac{\partial E_z}{\partial \rho} + \frac{\beta}{\rho} \frac{\partial H_z}{\partial \phi} \right), \quad (\text{A.5d})$$

where the fields are now of the form $\mathbf{E}(\rho, \phi, z) = [\mathbf{e}(\rho, \phi) + \hat{z}e_z(\rho, \phi)] e^{-j\beta z}$. In the case of TE modes the component $E_z = 0$, so equations (A.5) are solved founding H_z from the Helmholtz equation in cylindrical coordinates:

$$\left(\frac{\partial^2}{\partial \rho^2} + \frac{1}{\rho} \frac{\partial}{\partial \rho} + \frac{1}{\rho^2} \frac{\partial^2}{\partial \phi^2} + k_c^2 \right) h_z(\rho, \phi) = 0. \quad (\text{A.6})$$

The solution is derived with the method of separation of variables, so that it can be factorized as $h_z(\rho, \phi) = R(\rho)P(\phi)$. The solution for $P(\phi)$ is:

$$P(\phi) = A \sin(n\phi) + B \cos(n\phi),$$

where n is an integer number, because we require that the function is periodic in ϕ , due to the cylindrical symmetry. A and B are arbitrary constants. The solution for $R(\rho)$ is:

$$R(\rho) = C J_n(k_c \rho) + D Y_n(k_c \rho).$$

J_n and Y_n are Bessel functions of the first and second kind respectively, and satisfy the Bessel's differential equation. Y_n is physically unacceptable because has an infinite at $\rho = 0$, so the ultimate solution for the field h_z is:

$$h_z(\rho, \phi) = (A \sin(n\phi) + B \cos(n\phi)) J_n(k_c \rho). \quad (\text{A.7})$$

Now the boundary conditions has to be applied. The requirement is that the electric field tangential to the conducting walls must vanish. In this case the two tangential components are E_z , that is identically null, and E_ϕ . Looking at eq. (A.5) E_ϕ depends on $\partial H_z / \partial \rho$, then imposing that $E_\phi(\rho = a, \phi) = 0$ yields the condition:

$$J'_n(k_c a) = 0,$$

because the dependence on ρ only resides in the Bessel function. J'_n is the first derivative of J_n . This is equivalent to the request that the argument of J'_n be a root of this function. Defining the roots p'_{nm} such that $J'_n(p'_{nm}) = 0$, then we have for the cutoff wave number:

$$k_{c_{nm}} = \frac{p'_{nm}}{a}. \quad (\text{A.8})$$

The m index stands for the m -th root of the n -th function J'_n (Bessel functions have damped oscillations around the zero). The values of p'_{nm} are tabulated. From a field point of view the n index indicates the number of variations of the electric field in the ϕ direction, i.e. the number of its maximum values, while m indicates the number of variations along the ρ direction.

Once found the cutoff wave number (A.8), the propagation constant is:

$$\beta_{nm}^{\text{TE}} = \sqrt{k^2 - k_{c_{nm}}^2} = \sqrt{k^2 - \left(\frac{p'_{nm}}{a}\right)^2}. \quad (\text{A.9})$$

Now it is clear why the name *cutoff* was used for the wave number: β_{nm} is real when $k > k_{c_{nm}}$ and the waves can propagate, but when $k < k_{c_{nm}}$ the corresponding mode becomes *evanescent*, since β becomes pure imaginary and the propagation factor $e^{-j\beta z}$ takes the form of a decaying exponential. Also, a cutoff frequency can be defined:

$$f_{c_{nm}}^{\text{TE}} = \frac{k_{c_{nm}}}{2\pi\sqrt{\mu\epsilon}} = \frac{p'_{nm}}{2\pi a\sqrt{\mu\epsilon}}. \quad (\text{A.10})$$

Finally, having found the solution $h_z(\rho, \phi)$ (A.7), all the transverse field components for the TE_{nm} modes are:

$$E_\rho = \frac{-j\omega\mu n}{k_{c_{nm}}^2\rho}(A \cos n\phi - B \sin n\phi)J_n(k_{c_{nm}}\rho)e^{-j\beta z}, \quad (\text{A.11a})$$

$$E_\phi = \frac{j\omega\mu}{k_{c_{nm}}} (A \sin n\phi + B \cos n\phi)J'_n(k_{c_{nm}}\rho)e^{-j\beta z}, \quad (\text{A.11b})$$

$$H_\rho = \frac{-j\beta}{k_{c_{nm}}} (A \sin n\phi + B \cos n\phi)J'_n(k_{c_{nm}}\rho)e^{-j\beta z}, \quad (\text{A.11c})$$

$$H_\phi = \frac{-j\beta n}{k_{c_{nm}}^2\rho} (A \cos n\phi - B \sin n\phi)J_n(k_{c_{nm}}\rho)e^{-j\beta z}, \quad (\text{A.11d})$$

TM modes for circular waveguides

The derivation of the fields of TM modes follows the same procedure as for TE modes, with little differences. The starting point is again equations (A.5), where now $H_z = 0$ is imposed. To find the transverse fields, the Helmholtz equation (A.6) for e_z must be

solved, giving the same type of solution as for H_z , that is:

$$e_z(\rho, \phi) = (A \sin n\phi + B \cos n\phi) J_n(k_c \rho). \quad (\text{A.12})$$

In this case the boundary condition $E_z(\rho = a, \phi) = 0$ can be directly applied to e_z , thus giving the condition:

$$J_n(k_c a) = 0 \Rightarrow k_{c_{nm}} = \frac{p_{nm}}{a}, \quad (\text{A.13})$$

where p_{nm} are the m -th roots of the functions J_n , i.e. $J_n(p_{nm}) = 0$. As for TE modes, the propagation constant and the cutoff frequency can be determined in terms of $k_{c_{nm}}$ given in eq. (A.13). For TM_{nm} modes they are:

$$\beta_{nm}^{\text{TM}} = \sqrt{k^2 - \left(\frac{p_{nm}}{a}\right)^2}, \quad (\text{A.14})$$

$$f_{c_{nm}}^{\text{TM}} = \frac{p_{nm}}{2\pi a \sqrt{\mu\epsilon}}. \quad (\text{A.15})$$

As before, inserting the solution $E_z(\rho, \phi, z) = e_z(\rho, \phi) e^{-j\beta_{nm}z}$, with e_z given by (A.12), in equations (A.5), all the transverse field components for the TM_{nm} modes are:

$$E_\rho = \frac{-j\beta}{k_{c_{nm}}} (A \sin n\phi + B \cos n\phi) J'_n(k_{c_{nm}} \rho) e^{-j\beta z}, \quad (\text{A.16a})$$

$$E_\phi = \frac{-j\beta n}{k_{c_{nm}}^2 \rho} (A \cos n\phi - B \sin n\phi) J_n(k_{c_{nm}} \rho) e^{-j\beta z}, \quad (\text{A.16b})$$

$$H_\rho = \frac{j\omega\epsilon n}{k_{c_{nm}}^2 \rho} (A \cos n\phi - B \sin n\phi) J_n(k_{c_{nm}} \rho) e^{-j\beta z}, \quad (\text{A.16c})$$

$$H_\phi = \frac{-j\omega\epsilon}{k_{c_{nm}}} (A \sin n\phi + B \cos n\phi) J'_n(k_{c_{nm}} \rho) e^{-j\beta z}. \quad (\text{A.16d})$$

TE modes in a cylindrical cavity

Now that the electric and magnetic fields have been determined for cylindrical waveguides, the field configurations for a cylindrical cavity can be easily derived. Since the cavity is obtained by short-circuiting two sides of the waveguide, it suffices to impose additional boundary conditions at both ends. The cavity, with longitudinal size d and radius a , is shown in Fig. A.2. The electric fields of equations (A.11) for TE modes can be written in the more compact form $\mathbf{E}_t(\rho, \phi, z) = \mathbf{e}(\rho, \phi)(A^+ e^{-j\beta_{nm}z} + A^- e^{j\beta_{nm}z})$, where now also the backward travelling waves have been considered, and A^+ and A^- are arbitrary amplitude constants for the forward and backward waves, respectively. Now the conditions that the transverse electric fields must vanish at the end plates can be put. Assuming that the end plates are at $z = 0$ and $z = d$, the conditions are $\mathbf{E}_t(\rho, \phi, 0) = 0$ and $\mathbf{E}_t(\rho, \phi, d) = 0$. The

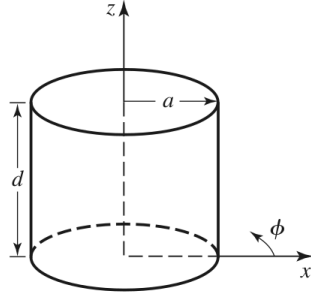


Figure A.2: A resonant cavity of length d and radius a . Taken from [44].

first gives $A^+ = -A^-$, and then the second becomes $-2jA^+e(\rho, \phi) \sin \beta_{nm}d = 0$, yielding:

$$\beta_{nml}d = l\pi. \quad (\text{A.17})$$

Thus the modes acquire another index l , that accounts for the number of field variations along the z axis. Note that with the condition $A^+ = -A^-$ the z dependence of the fields is of the type $-2jA^+ \sin(\beta_{nml}z)$, that is a standing wave, not a propagating wave, because forward and backward travelling waves sum up with the same amplitude.

A resonant wave number k is now defined as $k = \sqrt{k_{c_{nm}}^2 + \beta_{nml}^2}$ and then the *resonant frequency* for the TE_{nml} modes is:

$$f_{nml}^{\text{TE}} = \frac{k^{\text{TE}}}{2\pi\sqrt{\mu\epsilon}} = \frac{1}{2\pi\sqrt{\mu\epsilon}} \sqrt{\left(\frac{p'_{nm}}{a}\right)^2 + \left(\frac{l\pi}{d}\right)^2}, \quad (\text{A.18})$$

The expression of all the fields of TE_{nml} modes of a cylindrical cavity are easily derived taking their expressions for the cylindrical waveguide (eq. (A.11)), adding the backward travelling wave and imposing that $A^+ = -A^-$. Then the TE_{nml} field components are:

$$E_z = 0, \quad (\text{A.19a})$$

$$E_\rho = \frac{-j\omega\mu a^2 n H_0}{(p'_{nm})^2 \rho} J_n\left(\frac{p'_{nm}\rho}{a}\right) (A \cos n\phi - B \sin n\phi) \sin \frac{l\pi z}{d}, \quad (\text{A.19b})$$

$$E_\phi = \frac{j\omega\mu a H_0}{p'_{nm}} J'_n\left(\frac{p'_{nm}\rho}{a}\right) (A \sin n\phi + B \cos n\phi) \sin \frac{l\pi z}{d}, \quad (\text{A.19c})$$

$$H_z = H_0 J_n\left(\frac{p'_{nm}\rho}{a}\right) (A \sin n\phi + B \cos n\phi) \sin \frac{l\pi z}{d}, \quad (\text{A.19d})$$

$$H_\rho = \frac{\beta_{nml} a H_0}{p'_{nm}} J'_n\left(\frac{p'_{nm}\rho}{a}\right) (A \sin n\phi + B \cos n\phi) \cos \frac{l\pi z}{d}, \quad (\text{A.19e})$$

$$H_\phi = \frac{\beta_{nml} a^2 n H_0}{(p'_{nm})^2 \rho} J_n\left(\frac{p'_{nm}\rho}{a}\right) (A \cos n\phi - B \sin n\phi) \cos \frac{l\pi z}{d}, \quad (\text{A.19f})$$

with the definition $H_0 = -2jA^+$. The arbitrary constants A and B remain in the solutions,

and control the amplitudes of the sine and cosine terms. The latter are both valid solutions, because they are independent. The magnitude of A and B depends on how the cavity is excited.

TM modes in a cylindrical cavity

The solution to TM_{nml} modes is found in a similar manner as for TE modes. Also in this case, the boundary conditions yield to the same value of the propagation constant: $\beta_{nml} = l\pi/d$. Thus the resonant wave number is $k^{\text{TM}} = \sqrt{k_{c_{nm}}^2 + \beta_{nml}^2} = \sqrt{(p_{nm}/a)^2 + \beta_{nml}^2}$, where $k_{c_{nm}} = p_{nm}/a$ is the cutoff wave number found in eq. (A.13). The resonant frequency of the TM_{nml} modes is then:

$$f_{nml}^{\text{TM}} = \frac{k^{\text{TM}}}{2\pi\sqrt{\mu\epsilon}} = \frac{1}{2\pi\sqrt{\mu\epsilon}} \sqrt{\left(\frac{p_{nm}}{a}\right)^2 + \left(\frac{l\pi}{d}\right)^2}. \quad (\text{A.20})$$

For brevity, here I report only the (ρ, ϕ, z) dependence of all the electric and magnetic field components of TM_{nml} resonant modes:

$$H_z = 0, \quad (\text{A.21a})$$

$$H_\rho \sim \frac{1}{\rho} J_n \left(\frac{p_{nm}\rho}{a} \right) (A \cos n\phi - B \sin n\phi) \cos \frac{l\pi z}{d}, \quad (\text{A.21b})$$

$$H_\phi \sim J'_n \left(\frac{p_{nm}\rho}{a} \right) (A \sin n\phi + B \cos n\phi) \cos \frac{l\pi z}{d}, \quad (\text{A.21c})$$

$$E_z \sim J_n \left(\frac{p_{nm}\rho}{a} \right) (A \sin n\phi + B \cos n\phi) \cos \frac{l\pi z}{d}, \quad (\text{A.21d})$$

$$E_\rho \sim J'_n \left(\frac{p_{nm}\rho}{a} \right) (A \sin n\phi + B \cos n\phi) \sin \frac{l\pi z}{d}, \quad (\text{A.21e})$$

$$E_\phi \sim \frac{1}{\rho} J_n \left(\frac{p_{nm}\rho}{a} \right) (A \cos n\phi - B \sin n\phi) \sin \frac{l\pi z}{d}. \quad (\text{A.21f})$$

APPENDIX B

3-dB method

The 3-dB method relies on the measurement of the bandwidth of the resonance curve $S_{21}(\omega)$ at a particular value. The frequency ω of a resonance curve doesn't differ very much from the resonant frequency ω_0 , so that it can be written as $\omega = \omega_0 + \Delta\omega$, with $\Delta\omega$ small since $\omega_0 \approx \omega$. The expression of the input impedance (2.20) can be expanded near resonance and becomes [44]:

$$Z_{\text{in}} \simeq \frac{R}{1 + 2jQ_0\Delta\omega/\omega_0}. \quad (\text{B.1})$$

There exist a value of the input impedance, $|Z_{\text{in}}| = R/\sqrt{2}$, for which the real part of the power delivered to the resonator is half the power at the resonant frequency, and is drawn in Fig. 2.2b as the mark $0.707R$. Calling $\bar{\omega}_1$ and $\bar{\omega}_2$ the frequencies at which this occurs, the previous statement can be written as [44]:

$$\text{Re}\{P_{\text{in}}(\bar{\omega})\} = \frac{1}{2}P_{\text{loss}} = \frac{1}{4} \frac{|V|^2}{R}. \quad (\text{B.2})$$

The *half-power fractional bandwidth* BW is defined as:

$$BW = \frac{2\Delta\omega}{\omega_0} = \frac{\bar{\omega}_2 - \bar{\omega}_1}{\omega_0}, \quad (\text{B.3})$$

where in this case $\Delta\omega = \bar{\omega}_2 - \omega_0 = \omega_0 - \bar{\omega}_1$ assuming a symmetric resonance curve. With this definition, eq. (B.1) becomes:

$$Z_{\text{in}} \simeq \frac{R}{1 + jQ_0 BW}, \quad (\text{B.4})$$

hence the expression $|Z_{\text{in}}| = R/\sqrt{2}$ is satisfied only if:

$$Q_0 = \frac{1}{BW}. \quad (\text{B.5})$$

This is true for an ideal isolated resonator. When it is coupled to external circuitry, Q_0 and Q_L are related through the coupling coefficients as in eq. (2.49). The latter can be exploited to rewrite the expression of $S_{21}(\omega)$ (2.57) as:

$$S_{21}(\omega) = \frac{|S_{21}(\omega_0)|}{1 + jQ_L\delta}, \quad \text{with } |S_{21}(\omega_0)| = \frac{2\sqrt{\kappa_1\kappa_2}}{1 + \kappa_1 + \kappa_2}. \quad (\text{B.6})$$

Now, in the approximation that the frequency is near the resonant frequency, $\omega \approx \omega_0$, δ is just the fractional bandwidth: $\delta|_{\omega \approx \omega_0} \approx BW$. Thus, comparing the expression of Z_{in} for the parallel RLC circuit (B.4) and that for the transmission coefficient S_{21} (B.6), we see that they have the same form:

$$f(\omega) = \frac{f(\omega_0)}{1 + jQBW},$$

with the difference that S_{21} presents the loaded quality factor Q_L instead of Q_0 . In this case, that indeed is the real case, the bandwidth allows the determination of Q_L :

$$Q_L = \frac{1}{BW}. \quad (\text{B.7})$$

Having in mind the definition of BW (B.3), one can perform its measurement by determining the frequencies $\bar{\omega}_1$ and $\bar{\omega}_2$ for which $|S_{21}(\bar{\omega})| = |S_{21}(\omega_0)|/\sqrt{2}$, and ω_0 is easily obtained as the frequency at which $|S_{21}|$ reaches its maximum, $|S_{21}(\omega_0)|$. The procedure is named the 3-dB method because if the transmission coefficient is expressed in decibels, with $|S_{21}(\omega_0)|^2$ as the reference value, one has:

$$10 \log_{10} \left(\frac{|S_{21}(\bar{\omega})|^2}{|S_{21}(\omega_0)|^2} \right) = 10 \log_{10} \left(\frac{1}{2} \right) \simeq -3 \text{ dB}. \quad (\text{B.8})$$

So, if data are expressed in decibels, the half-power fractional bandwidth corresponds to a value of $S_{21}(\omega)$ 3 decibels below the maximum value $|S_{21}(\omega_0)|$. These calculations are automatically made by network analyzers and give the loaded quality factor Q_L .

Bibliography

- [1] I. Irastorza and J. Redondo. In: *Progress in Particle and Nuclear Physics* **102** (2018). [arXiv:1801.08127v2](https://arxiv.org/abs/1801.08127v2), p. 89 (cit. on pp. 1, 19, 24, 27, 28, 30, 32–35).
- [2] J. M. Pendlebury et al. In: *Phys. Rev. D* **92** (2015). [arXiv:1509.04411v3](https://arxiv.org/abs/1509.04411v3), p. 092003 (cit. on pp. 2, 4, 14).
- [3] R. Peccei and H. Quinn. In: *Phys. Rev. Lett.* **38** (1977), p. 1440 (cit. on pp. 2, 15).
- [4] R. Peccei and H. Quinn. In: *Phys. Rev. D* **16** (1977), p. 1791 (cit. on pp. 2, 15, 16).
- [5] F. Wilczek. *Asymptotic freedom: from paradox to paradigm*. Nobel Lecture. 2004. URL: https://www.nobelprize.org/nobel_prizes/physics/laureates/2004/wilczek-lecture.pdf (cit. on p. 2).
- [6] P. Sikivie. In: *Phys. Rev. Lett.* **51** (1983), p. 1415 (cit. on pp. 2, 31, 34, 64).
- [7] B. M. Brubaker. *First results from the HAYSTAC axion search*. PhD dissertation. [arXiv:1801.00835v1](https://arxiv.org/abs/1801.00835v1). Yale University, 2018 (cit. on pp. 4, 8, 20, 22, 26, 28, 30, 41).
- [8] P. Collins, A. Martin, and E. Squires. *Particle Physics and Cosmology*. Wiley, 1989 (cit. on pp. 5, 6, 8–10).
- [9] M. Tanabashi et al. In: *Phys. Rev. D* **98** (2018), p. 030001 (cit. on pp. 5, 22–25, 27).
- [10] M. Srednicki. *Quantum Field Theory*. Cambridge University Press, 2007 (cit. on pp. 6, 9–11).
- [11] F. Mandl and G. Shaw. *Quantum Field Theory*. Wiley, 2010 (cit. on p. 6).
- [12] S. Weinberg. In: *Phys. Rev. D* **11** (1975), p. 3583 (cit. on p. 7).
- [13] R. Peccei. In: *J. Korean Phys. Soc.* **29** (1996). [arXiv:hep-ph/9606475v1](https://arxiv.org/abs/hep-ph/9606475v1) (cit. on pp. 8, 12, 13, 16–18).

Bibliography

- [14] R. E. Collin. *Foundations for Microwave Engineering*. Wiley-Interscience, 2001 (cit. on pp. 9, 107).
- [15] R. Peccei. *The Strong CP Problem and Axions*. arXiv:hep-ph/0607268v1. 2006 (cit. on pp. 10, 15).
- [16] M. Pospelov and A. Ritz. In: *Nuclear Physics B* **573**.1 (2000). arXiv:hep-ph/9908508v4 (cit. on p. 14).
- [17] V. Baluni. In: *Phys. Rev. D* **19** (1979), p. 2227 (cit. on p. 14).
- [18] S. Weinberg. In: *Phys. Rev. Lett.* **40** (1978), p. 223 (cit. on p. 15).
- [19] F. Wilczek. In: *Phys. Rev. Lett.* **40** (1978), p. 279 (cit. on p. 15).
- [20] D. Budker et al. In: *Phys. Rev. X* **4** (2014), p. 021030 (cit. on p. 17).
- [21] W. Bardeen, R. Peccei, and T. Yanagida. In: *Nucl. Phys. B* **279** (1987), p. 401 (cit. on p. 18).
- [22] J. Kim. In: *Phys. Rev. Lett.* **43** (1979), p. 103 (cit. on p. 18).
- [23] M. Shifman, A. Vainshtein, and V. Zakharov. In: *Nucl. Phys. B* **166** (1980), p. 493 (cit. on p. 18).
- [24] A. Zhitnitsky. In: *Sov. J. Nucl. Phys.* **31** (1980), p. 260 (cit. on p. 18).
- [25] M. Dine, W. Fischler, and M. Srednicki. In: *Phys. Lett. B* **104** (1981), p. 199 (cit. on p. 18).
- [26] J. Jaeckel and A. Ringwald. In: *Annu. Rev. Nucl. Part. Sci.* **60** (2010), p. 405 (cit. on pp. 19, 24, 31).
- [27] H. Primakoff. In: *Phys. Rev.* **81** (1951), p. 899 (cit. on p. 20).
- [28] G. G. Raffelt. “Astrophysical Axion Bounds”. In: *Lecture Notes in Physics*. Vol. 741. Springer, 2008, pp. 51–71. URL: <https://arxiv.org/abs/hep-ph/0611350> (cit. on p. 22).
- [29] L. Di Luzio, F. Mescia, and E. Nardi. In: *Phys. Rev. Lett.* **118** (2017), p. 031801 (cit. on p. 23).
- [30] M. Srednicki. In: *Nucl. Phys. B* **260** (1985), p. 689 (cit. on p. 24).
- [31] P. Arias et al. In: *JCAP* 06 (2012), p. 013 (cit. on p. 26).
- [32] P. A. R. Ade and others (Planck collaboration). In: *Astron. Astrophys.* **594**.A13 (2016). arXiv:1502.01589v3 (cit. on p. 27).
- [33] J. I. Read. In: *J. Phys. G* **41**.6 (2014). arXiv:1404.1938v2, p. 063101 (cit. on p. 28).
- [34] E. Lentz et al. In: *ApJ* **845** (2017). arXiv:1703.06937v1, p. 121 (cit. on p. 28).
- [35] M. S. Turner. In: *Phys. Rev. D* **42** (1990), p. 3572 (cit. on pp. 28, 29).

- [36] P. Sikivie. In: *Phys. Rev. D* **32** (1985), p. 2988 (cit. on pp. 31, 32, 34, 41).
- [37] L. Krauss et al. In: *Phys. Rev. Lett.* **55** (1985), p. 1797 (cit. on pp. 31, 36, 41, 65).
- [38] S. Asztalos et al. In: *Phys. Rev. D* **64** (2001), p. 092003 (cit. on pp. 32, 33, 42).
- [39] N. Du et al. In: *Phys. Rev. Lett.* **120** (2018). arXiv:1804.05750v2, p. 151301 (cit. on p. 33).
- [40] D. Alesini et al. *The KLASH Proposal*. 2017. URL: <https://arxiv.org/abs/1707.06010> (cit. on p. 33).
- [41] K. Zioutas et al. In: *Nucl. Instrum. Meth. A* **425** (1999). arXiv:astro-ph/9801176v2, p. 480 (cit. on p. 35).
- [42] R. Barbieri et al. In: *Phys. Dark Univ.* **15** (2017), p. 135 (cit. on pp. 36–40).
- [43] N. Crescini et al. *Operation of a ferromagnetic Axion haloscope at $m_a = 58 \mu\text{eV}$* . 2018. URL: <https://arxiv.org/abs/1806.00310> (cit. on pp. 36, 66, 97).
- [44] D. M. Pozar. *Microwave Engineering*. Wiley, 2012 (cit. on pp. 43, 44, 46–48, 62, 107, 112, 114).
- [45] C. M. Rey and A. P. Malozemoff. “Fundamentals of superconductivity”. In: *Superconductors in the Power Grid*. Woodhead Publishing, 2015, pp. 29–73 (cit. on pp. 55, 58).
- [46] M. Tinkham. *Introduction to Superconductivity*. McGraw-Hill, Inc., 1996 (cit. on pp. 55–58, 60).
- [47] J. I. Gittleman and B. Rosenblum. In: *Phys. Rev. Lett.* **16** (1966), p. 734 (cit. on p. 60).
- [48] J. I. Gittleman and B. Rosenblum. In: *Journal of Applied Physics* **39** (1968), p. 2617 (cit. on pp. 60, 61).
- [49] R. Marcon et al. In: *Phys. Rev. B* **43** (1991), p. 2940 (cit. on p. 61).
- [50] S. Calatroni and R. Vaglio. In: *IEEE Transactions on Applied Superconductivity* **27.5** (2017) (cit. on p. 61).
- [51] G. Ventura and L. Risegari. *The Art of Cryogenics*. Elsevier, 2008 (cit. on pp. 69, 71).
- [52] P. J. Petersan and S. M. Anlage. In: *Journal of Applied Physics* **84** (1998) (cit. on pp. 74, 76).
- [53] D. Kajfez. *Q factor measurements, analog and digital*. 1999. URL: <https://engineering.olemiss.edu/~eedarko/experience/rfqmeas2b.pdf> (cit. on pp. 74, 75).
- [54] K. Coakley et al. In: *IEEE Transactions on Microwave Theory and Techniques* **51.3** (2003) (cit. on p. 74).

Bibliography

- [55] D. Kajfez et al. In: *IEEE Transactions on Microwave Theory and Techniques* **47**.3 (1999) (cit. on p. [75](#)).
- [56] N. Pompeo et al. In: *2017 IEEE International Instrumentation and Measurement Technology Conference (I2MTC)* (2017), pp. 1–6 (cit. on pp. [76](#), [77](#)).
- [57] C. P. Poole, H. A. Farach, and R. J. Creswick. *Superconductivity*. Academic Press, 1995 (cit. on p. [81](#)).
- [58] C. Buzea and T. Yamashita. In: *Supercond. Sci. Technol.* **14** (2001), R115 (cit. on p. [81](#)).
- [59] I. N. Askerzade et al. In: *Supercond. Sci. Technol.* **15** (2002), p. L13 (cit. on pp. [81](#), [103](#)).
- [60] S Sarti et al. In: *Phys. Rev. B* **72** (2005), p. 024542 (cit. on p. [103](#)).
- [61] G. Giunchi et al. In: *Supercond. Sci. Technol.* **20** (2007), p. L16 (cit. on p. [103](#)).